MULTIOBJECTIVE AND LEVEL SET METHODS FOR RESERVOIR CHARACTERIZATION AND OPTIMIZATION

A Dissertation

by

JICHAO HAN

Submitted to the Office of Graduate and Professional Studies of
Texas A&M University
in partial fulfillment of the requirements for the degree of

DOCTOR OF PHILOSOPHY

Chair of Committee,	Akhil Datta-Gupta
Committee Members,	Michael J. King
	Eduardo Gildin
	Yalchin Efendiev
Head of Department,	A. Daniel Hill

May 2016

Major Subject: Petroleum Engineering

ABSTRACT

Proper management of oil and gas reservoirs as dynamic systems reduces operational expenditures, alleviates uncertainty, and increases hydrocarbon recovery. In this dissertation, we focus on two issues in reservoir management: multiobjective integration and channelized reservoir calibration. Multiple objectives, including bottom-hole pressure (BHP), water cut, and 4-D seismic data, are utilized in model ranking, history matching, and production optimization. These objectives may conflict, as they represent characteristics coming from different measurements and sources, and, significantly, of varying scales. A traditional weighted-sum method may reduce the solution space, often leading to loss of key information for each objective. Thus, how to integrate multiple objectives effectively becomes critical in reservoir management. This dissertation presents a Pareto-based approach to characterize multiobjective and potentially conflicting features and to capture geologic uncertainty, preserving the original objective space and avoiding weights determination as in the weight-sum method. For channelized reservoirs, identification of the channel geometry and facies boundaries, as well as characterization of channel petrophysical properties are critical for performance predictions. Traditional history matching methods, however, are unable to preserve the channel geometry. We propose a level set based method, integrated with seismic constraint and coupled with the Grid Connectivity Transform (GCT) for channelized reservoirs calibration.

We first develop the Pareto-based model ranking (PBMR) to rank multiple realizations, taking into consideration seismic and production data. We demonstrate that

this approach can be applied to select multiple competitive realizations compared with the weighted-sum method, and uncertainty range of each objective can be effectively addressed.

Next, we extend the Pareto-based framework to full-field history matching and production optimization of the Norne Field in the North Sea. A hierarchical history matching workflow including global and local updates helps to capture the large- and fine-scale heterogeneity. A two-step polymer flood optimization consisting of the streamline-based rate optimization and the Pareto-based polymer optimization is shown to be beneficial for reducing the impact of heterogeneity and increasing production improvement as well as NPV.

Finally, we propose a two-step history matching workflow for facies and property calibration of the channelized reservoirs, where the channel geometry is modeled using the level set method, and smaller scale heterogeneity is modeled using the GCT. Moreover, the seismic constraints incorporated into the level set improves facies model calibration.

DEDICATION

I dedicate this dissertation to my parents, my relatives and my friends for their support and care.

ACKNOWLEDGEMENTS

I would like to express my sincere gratitude to my advisor, Dr. Datta-Gupta for his academic guidance and financial support for my PhD studies. His immense knowledge, insightful view, and continuous encouragement helped me smooth away the difficulties and obstacles on the way to success. Also, his generous support for industry internship opportunities was helpful to expand my horizons before joining the industry.

I would like to extend my deepest gratitude to my committee members, Dr. King, Dr. Gildin, and Dr. Efendiev for their valuable comments and suggestions that helped me improve the quality and level of my dissertation.

I would like to thank Anadarko, Schlumberger and Shell companies in Houston for providing me the internship opportunities. I would like to show my sincere gratitude to P.K. Pande, Sathish Sankaran, Doug Shotts, Kyrre Bratvedt, Shingo Watanabe, Detlef Hohl and Eduardo Jimenez and Tzu-hao Yeh for their patience and trust during my summer internships.

Thanks for all the MCERI members and friends in Texas A&M. All of you composed a perfect colorful painting for my wonderful life in College Station.

Finally, thanks for my beloved parents in China. They provided me a strong spiritual motivation to overcome the difficulties both in my study and life in America.

TABLE OF CONTENTS

Page

LIST OF FIGURES

Page

LIST OF TABLES

Page

CHAPTER I

INTRODUCTION AND STUDY OBJECTIVES

Proper management of oil and gas reservoirs as dynamic systems reduces operational expenditures, alleviates uncertainty, and increases hydrocarbon recovery. This dissertation focuses on two issues of reservoir management: multiobjective integration and channelized reservoir calibration. First, the research aims to establish a systematic multiobjective workflow consisting of model ranking, history matching, and production optimization, especially in field application. Second, a channelized reservoir history matching workflow will be proposed in terms of seismic integration.

1.1 Overview of Multiobjective Integration in Reservoir Management

Model ranking, history matching, and production optimization play the important roles in the reservoir management. The Model ranking acts as a bridge between geological modeling and reservoir engineering, and provides several good candidates for history matching and optimization in the next stage. History matching is used to calibrate selected geological models under the guidance of seismic and production data for more accurate prediction of future production. Production optimization provides optimal operation schedules and development plans to maximize reservoir recovery while reducing operational expenditures. These three processes either use a single measurement or include multiple objectives, such as bottom-hole pressure (BHP), water cut and 4-D seismic data,

which are potentially conflicting due to incorrect assumptions on variables, measurement errors, and uncertainty on the inverted data.

1.1.1 Model Ranking

In model ranking, research studies focus on a single reservoir performance parameter to evaluate models. Alabert and Modot (1992) proposed a ranking method based on connected pore volumes around the wells. Hirsch and Schuette (1999) proposed a ranking approach looking at the permeability connectivity from the graph theory perspective, using a shortest-path algorithm. Similarly in the graph theory framework, Kim and Dobin (2008) considered a Fast Marching Method (FMM), taking the absolute permeability-porosity ratio as the speed function in the estimation of connected pore volumes as a measure of reservoir performance. These approaches pay more attention to static properties, which cannot account for dynamic flow behavior. In that line, Idrobo et al. (2000) and Mishra et al. (2000) applied thresholds to the convective time-of-flight contour to estimate the volumetric sweep efficiency, E_V, which was used as a surrogate parameter for ranking multiple geologic models. Hird and Dubrule (1998) proposed the drainable Hydrocarbon Pore Volume (HCPV) concept based on a Resistivity Index (RI) method, which was well correlated with ultimate recovery. However, all these applications are based on a single measurement, no matter whether they are static or dynamic properties.

Getting around this problem has resulted in the evaluation of geologic models using multiple criteria for equiprobable realizations. Odai and Ogbe (2011) used the static and dynamic measures — stock tank oil originally in place, geometric average permeability,

connected HCPV, average breakthrough time, and cumulative recovery — to select models for history matching of field water, but this method deals with each measurement separately rather than considering them together. The Pareto-based concept, which can handle multiple objectives simultaneously, has been incorporated in the multiobjective optimization evolutionary algorithm (MOEA) to find multiple representative Pareto-optimal solutions instead of solutions biased toward some preferred objective (Deb et al. 2002; Li and Zhang 2009; Srinivas and Deb 1994). In recent years, a fully explored solution space and consideration of conflicting characteristics made the Pareto-based algorithm popular in multiobjective history matching (Mohamed et al. 2011; Park et al. 2013). However, the Pareto-based concept has not been used in the model ranking area for handling multiple criteria.

1.1.2 History Matching and Production Optimization

Instead of manual history matching method, which is impractical for large and complex fields, the assisted history matching (AHM) method has drawn a lot of attention over the past decades. AHM mainly includes the gradient-based methods, sensitivity-based methods and derivative-free methods in terms of minimizing the difference between simulation and observed data. The gradient-based methods, such as the Levenberg–Marquardt, BFGS, and limited-memory BFGS are efficient when the objective function is sufficiently smooth, but are inappropriate for discrete properties (Gao and Reynolds 2006; McCormick and Tapia 1972). Also, the convergence of Gradient-based methods is typically very slow. Instead, the sensitivity-based methods can converge faster. In

particular, the streamline-based generalized travel time inversion (GTTI) (Wu and Datta-Gupta 2002) approach has been widely adopted in many field applications (Cheng et al. 2005; Kam and Datta-Gupta 2014; Tanaka et al. 2015). These deterministic techniques, such as the gradient-based and sensitivity-based methods, are easily trapped in the local optimum and are not robust for the uncertainty analysis. In contrast, the derivative-free methods, such as the genetic algorithm (Holland 1992) and the Markov Chain Monte Carlo (MCMC) (Hastings 1970) are powerful to search global optimum for the complex reservoir models and more effectively quantify the uncertainty by providing more alternative simulation models without requiring any gradient calculation. The disadvantage of derivative-free methods is that the computation is highly prohibitive because of plenty of simulation running requirement, especially for relatively large number of parameters to be updated.

In practice, history matching always involves multiple objectives. The traditional technique typically aggregates all the objectives into the single objective space, called the weighted-sum method, regardless of whether these objectives conflict. It will be problematic for the weighted-sum method when the objectives are conflicting. The more conflicting the objectives are, the worse results weighted-sum method produces. Weighted-sum method squeezes the objectives solution space, and each objective is tied with each other, resulting that the original solution space cannot be preserved. Moreover, the weighting factor assignment for each objective is very subjective, mainly relying on the prior knowledge and degree of confidence. Cheng et al. (2008) used weighted sum of squares difference between the observed values and calculated model values for joint

integration of static gradient surveys (SGS) and modular dynamic tests (MDT) pressure data. Rey et al. (2012) applied a penalized misfit function in which the weighting factors control the balance between production and seismic data misfit. Similarly, Denney (2012) assigned different weighting factors for production misfit and seismic misfit respectively.

Similar issues can be found in the polymer optimization. Polymer injection during water flooding can effectively reduce viscous fingering and increase sweep efficiency by decreasing the mobility of the injected water, which results from the increase of water viscosity and reduction of rock permeability to water. The objective of polymer optimization is to maximize the net present value (NPV) (Van Doren et al. 2011). To evaluate polymer performance, generally, oil production improvement after injecting polymer can be used as a measurement. Polymer utility factor (UF), which the ratio between the total injected polymer and incremental oil production, is also proven to be an effective measurement for polymer usage efficiency (Clemens et al. 2011). Unfortunately, large oil production improvement always comes with poor polymer usage efficiency. It is a challenge to find an optimal solution considering oil production improvement and UF.

To solve the above issues, the Pareto-based concept, which is used for the model ranking, is incorporated into the MOEA, contributing to finding multiple representative Pareto-optimal solutions instead of solutions biased toward some preferred objective (Deb et al. 2002; Li and Zhang 2009; Srinivas and Deb 1994). Mohamed et al. (2011) developed the Multi-Objective Particle Swarm Optimisation approach (MOPSO) which coupled the Pareto-based algorithm with particle swarm method to keep the solution diversity. Park et al. (2013) replaced the classical genetic algorithm with the Pareto-based MOEA to

update the GCT coefficients in the hierarchical workflow framework for history matching with potentially conflicting objectives.Olalotiti-Lawal and Datta-Gupta (2015) proposed a multiobjective MCMC approach to sample multiple trade-off solutions along the Pareto front for history matching and uncertainty quantification.

1.2 Overview of Model Calibration of Channelized Reservoirs

Identification of the channel geometry, facies boundaries and characterization of channel petrophysical properties are critical for performance prediction of channelized reservoirs. On account of the sharp contrast between facies, the orientation and geometry of channels with high permeability contribute most to the fluid flow, followed by the heterogeneity within the channel. Thus, it is important to efficiently update channel geometry as well as channel petrophysics during history matching.

There are many difficulties for traditional geostatistical techniques, such as the two-point geostatistical method, the object-based modeling approach, and the multi-point geostatistical method, to calibrate channelized reservoirs. The two-point geostatistical method is inappropriate for the channel geometry reproduction because a variogram cannot represent spatial continuity at more than two locations simultaneously (Koltermann and Gorelick 1996). Although the object-based method (Deutsch and Wang 1996) has been widely used in generating channelized facies distributions, it is difficult and time-consuming to incorporate into history matching to honor dynamic data. The multi-point geostatistical (Strebelle and Journel 2001) method, overcoming the downsides of the two-

point and object-based methods, heavily relies on the quality of the training image, which possesses too many uncertainties.

Parameterization methods have been successfully applied in the image reconstruction (Bhark et al. 2011; Jafarpour 2011; Jafarpour et al. 2009b) and the inverse problem (Awotunde and Horne 2010; Jafarpour et al. 2009a; Kang et al. 2014) by reducing parameter dimensionality. Especially in the history matching of channelized reservoirs, parameterization may mitigate the issues brought by geostatistical approach in terms of keeping the large-scale channel continuity while honoring dynamic data. The Discrete Cosine Transform (DCT) uses a small number of coefficients to capture dominant features of reservoir permeability distributions and helps capture spatial continuity of geological facies in channelized environments during history matching (Jafarpour and McLaughlin 2009). Currently, the main limitation of the DCT is that it can only be used in spatial domains with regular spatial structure. In contrast, the GCT can be extended from structure grids to unstructured grids (Bhark et al. 2011b; Bhark et al. 2012). The Discrete Wavelet Transform (DWT) is another attractive approach for the history matching of channelized reservoirs on account of its ability of capturing both frequency and location information. Jafarpour (2011) calculated the sensitivity of flow response with respect to important wavelet coefficients and used the Ensemble Kalman Filter (EnKF) to update this subset of wavelet coefficients to approximate the spatial distribution of permeability. The DWT is also powerful in the integration of different sources of data. For the integration, production and variogram information can be integrated sequentially into the reservoir model by calculating a sensitivity matrix of production response to wavelet coefficients (Kind and

Quinteros 2007; Sahni and Horne 2005, 2006a, 2006b). However, the difficulties in location and estimation of significant DWT coefficients become the bottleneck to improve the DWT performance in the inverse problem.

The level set method, as a numerical algorithm for surface and shape tracking (Osher and Fedkiw 2002; Osher and Sethian 1988; Osher and Santosa 2001), has shown great promise to effectively parameterize facies boundaries and allows for changing channel geometry and connectivity during history matching. Xie et al. (2011) applied the two-stage MCMC to perturb the coefficients of velocity eigenvectors, followed by the channel boundaries evolution through solving the level set equation. Ping and Zhang (2014) parameterized channelized reservoirs into a group of parameters: level set function, real radius and virtual radius, which are updated by the EnKF. These approaches simply assumed constant properties within each facies, ignoring the heterogeneity of the reservoir field. In that line, Agbalaka and Oliver (2011) and Lorentzen et al. (2012) used the EnKF, combined with the level set method, to jointly update facies boundaries and estimate petrophysical properties within each facies. The approaches listed above mainly focus on conditioning models to well data but seismic constraint in the level set has not been mentioned in the current literature. The successful integration of seismic constraint can help to not only significantly improve channelized reservoir history matching performance, but also extend the level set from simple channelized models to more complicated ones.

1.3 Objectives and Dissertation Outline

This dissertation mainly focuses on the Pareto-based multiobjective optimization application and channelized reservoir calibration in the reservoir management. The specific objectives and main chapters are outlined as follows:

In Chapter II, we will design the Pareto-based model ranking workflow to select favorable realizations for history matching and optimization based on multiple conflicting objectives. This approach, coupled with cluster analysis, can capture more plausible solutions, which keep potentially conflicting information.

In Chapter III, we will apply a hierarchical history matching workflow and a two-step polymer flood optimization on the Norne Field. Both history matching and polymer optimization employ the Pareto-based framework to consider multiple objectives. We aim to provide well calibrated models and optimized production parameters for production and NPV improvement.

In Chapter IV, we implement a two-step history matching workflow, where the channel geometry is modeled using the level set with/without seismic constraint, and internal scale heterogeneity is modeled using the GCT. Our objective is to improve channelized geometry calibration with seismic constraints and efficiently update channel petrophysics.

CHAPTER II

RANKING GEOLOGIC MODELS USING PARETO OPTIMALITY CRITERION

In this chapter, we present Pareto-based model ranking (PBMR) approach for model ranking, taking into account multiple and potentially conflicting objectives. In the model ranking, when multiple objectives, such as seismic and production data, are encountered, the traditional weighted-sum method presents difficulty in determine weighting factors, and does not fully explore the solution space. The proposed Pareto-based approach can effectively overcome these difficulties by avoiding interference between multiple objectives. Thus, the original objective space is preserved by avoiding weights determination, and more plausible solutions can be captured, while keeping conflicting information. The coupled cluster analysis serves choosing final models from selected optimal model set in the absence of prior knowledge.

2.1 Introduction

Significant uncertainties in petroleum exploration investment decisions can be primarily tied to uncertainties in subsurface model parameters. Uncertainties abound in the spatial distribution of static and dynamic properties, such as porosity, permeability, phase saturations, phase contacts, fault structures, and facies distribution. These uncertainties may be reduced as more data, such as well log, well test, production, and seismic data, are integrated into existing geologic models (Hu et al. 1999).

Geostatistical methods have widely been adopted as an important tool in geologic modeling and uncertainty quantification (Hu et al. 1999; Journel 1990). This generally involves generating multiple equiprobable realizations of models that satisfy the available information. If all the models are used in the history matching and production optimization, it can be computationally prohibitive for high resolution geologic models at the field scale. Thus, model ranking/evaluation is needed to reduce the number of realizations before reservoir simulation based on some specific reservoir performance parameters.

Model ranking technologies have evolved over time, starting from the Dykstra-Parsons method of characterizing and ranking model permeability heterogeneities (Johnson Jr 1956). Alabert and Modot (1992) proposed a ranking method based on connected pore volumes around the wells, but this method was later shown in a waterflood system to give poor correlations with oil recovery factor, which was the measure of reservoir performance (Saad et al. 1996). Hirsch and Schuette (1999) proposed a ranking approach looking at the permeability connectivity from the graph theory perspective, using a shortest-path algorithm. Similarly in the graph theory framework, Kim and Dobin (2008) considered a Fast Marching Method (FMM), taking the absolute permeability-porosity ratio as the speed function in the estimation of connected pore volumes as a measure reservoir performance. However, these approaches pay more attention to static properties, which cannot account for dynamic flow behavior.

Recent advances in streamline simulation (Datta-Gupta and King 2007) has helped in the incorporation of more realism to ranking geologic models. Idrobo et al. (2000) and

Mishra et al. (2000) applied thresholds to the convective time-of-flight contour to estimate the volumetric sweep efficiency, E_V, which was used as a surrogate parameter for ranking multiple geologic models. Similarly, Shook and Mitchell (2009) proposed a model ranking approach that uses the E_V as the surrogate parameter but was however calculated using only the dynamic flow capacity. Although these approaches account for a fair amount of system dynamics into the ranking procedure, streamlines and the concept of swept volumes were designed for convective flows, rather than diffusive transport. In that line, the concept of ranking geologic models based on efficient drainage volume calculations becomes more attractive. Hird and Dubrule (1998) proposed the drainable Hydrocarbon Pore Volume (HCPV) concept based on a Resistivity Index (RI) method which was well correlated with ultimate recovery. This method has been acclaimed useful for ranking geologic models under primary recovery (Shook and Mitchell 2009). However all these applications are based on a single measurement, no matter whether they are static or dynamic properties.

Getting around this problem has resulted in the evaluation of geologic models using multiple criteria for the equiprobable realizations. Odai and Ogbe (2011) used the static and dynamic measures — stock tank oil originally in place, geometric average permeability, connected HCPV, average breakthrough time, and cumulative recovery — to select models for history matching of field water, but this method deals with each measurement separately rather than considering them together. The Pareto-based concept, which can handle multiple objectives simultaneously, has been incorporated in the multi-objective evolutionary algorithm (MOEA) to find multiple representative Pareto-optimal

solutions instead of solutions biased toward some preferred objective (Deb et al. 2002; Li and Zhang 2009; Srinivas and Deb 1994). In recent years, a fully explored solution space and consideration of potentially conflicting characteristics of multiple data sets made the Pareto-based algorithm popular in multi-objective history matching. Mohamed et al. (2011) developed the Multi-Objective Particle Swarm Optimization approach (MOPSO), which coupled the Pareto-based algorithm with particle swarm method to keep the solution diversity. Park et al. (2013) replaced the classical genetic algorithm with the Pareto-based MOEA to update the Grid Connectivity Transform (GCT) coefficients in the hierarchical workflow framework for history matching with potentially conflicting objectives. However, the Pareto-based concept has not been used in the model ranking area for handling multiple criteria.

The Pareto-based model ranking is proposed to reduce geologic models set by ranking using dynamic data. The outline of this chapter is as follows. We first review the idea and formulation for Pareto concept as it applies to ranking multiple solutions. Then, we briefly introduce the PBMR workflow for ranking multiple geologic realizations based on field data misfits. The PBMR workflow will first be illustrated with a synthetic case of 102 geologic realizations and then applied to the Brugge field (Peters et al. 2009) having 104 realizations. In both cases, production and seismic objectives are considered, which explains why the Pareto-based approach is a promising way to integrate different types of data. The K-means clustering algorithm (Elphick and Moore 1999; L.N.Y.Wong and G.Liu 2010; Tokhmechi et al. 2008) is included to assist PBMR workflow to reduce the model set while preserving the model spread. The combination of the Pareto-based method

and K-means clustering approach takes into account the conflicting nature of different objectives in selecting the desired number of models for reservoir engineering and subsurface uncertainty analysis.

2.2 Pareto Concept

Dominance relationship among conflicting solutions forms the basis for Pareto concept. For a minimization problem involving *n* conflicting objectives defined by objective function *f*, solution *a* dominates *b* if all objectives represented by *a* are not greater than those of *b*, and at least one objective of *a* is strictly smaller than the corresponding objective(s) of *b*. This is mathematically described by the following expression:

$$\forall i \in \{1,2,\dots,n\}: f_i(a) \leq f_i(b) \wedge \exists j \in \{1,2,\dots n\}: f_i(a) < f_i(b) \qquad (2.1)$$

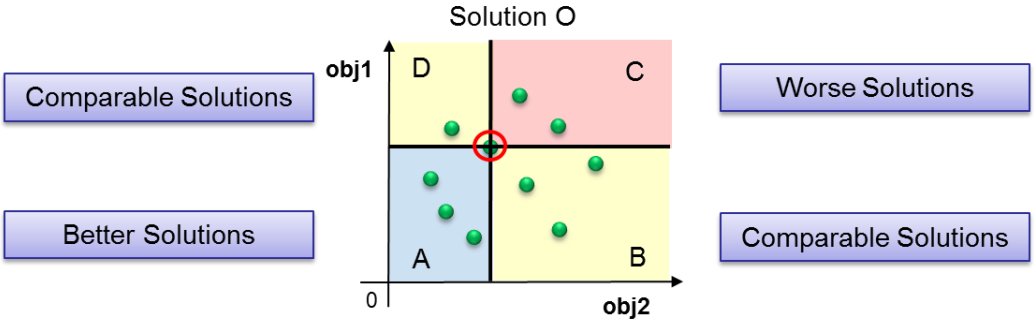

Figure 2-1 Domination concept.

The Pareto concept is also graphically explained in Figure 2-1. To explain the idea, we start by projecting the solutions to the objective space defined by objectives *obj1* and *obj2* under consideration. To describe the dominance relationship with solution *O* selected at random, we draw vertical and horizontal lines at this solution point to partition the entire

objective space into four parts as shown in the diagram. In partition A, both *obj1* and *obj2* of all three solutions are smaller than those of solution *O*. In other words, for a minimization problem, solutions in partition A are better solutions and dominate solution *O*. In partition C, both *obj1* and *obj2* of the two solutions are larger than those of solution *O*. Hence, these solutions represent worse solutions, and they are dominated by solution *O*. In partitions B and D, solutions have one of *obj1* and *obj2* smaller than either of those of solution *O*. As such, these solutions are comparable, and there are no domination relationships between partition B and D solutions and solution *O*.

Similar analysis can be performed on every solution point to obtain the rank level of each, as shown in Figure 2-2. First, a set of models, which are not dominated by the rest models, can be classified as rank 1 level models. Then, the rank 1 models are excluded from the solutions set, and similar analysis performed to obtain the rank 2 level. Rank 2 (and rank 1) models are then excluded to obtain the next rank level of non-dominated solutions. This is continued until all models in the domain have been assigned a rank level. Solutions on each rank level exhibit certain features. First, solutions on the same Pareto front are equally optimal. It is mathematically difficult to decide which model is better than the other on the same rank level without prior information. Second, the lower rank solutions are more competitive than higher rank ones for a minimization problem. Since our objectives here are misfit between observed and calculated data, the solutions on the lower rank levels, regarded as highly ranked models, are closer to the observed data and therefore, more competitive than models on the higher rank levels. Finally, trade-offs of

the front reveal potential conflict between objectives. If the objectives are highly conflicting, we will expect a large trade-off.

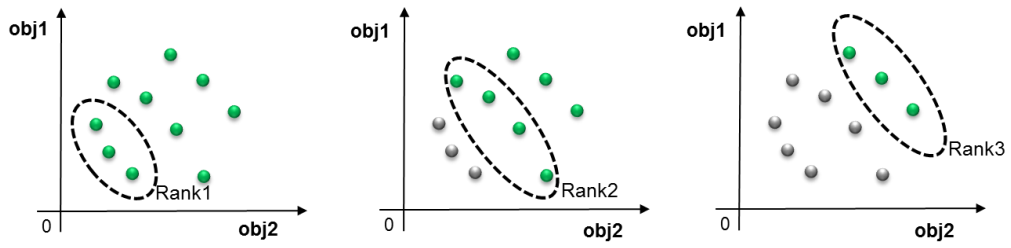

Figure 2-2 Rank level concept.

2.3 Pareto-based Modeling Ranking Workflow

Before illustration, the Pareto-based model ranking workflow (Figure 2-3) is proposed to show the whole picture. To start PBMR, we get initial model set using the geostatistical method and determine the types of objectives involved in model ranking. Forward simulations based on the model set are then carried out to obtain objective values. Next, all the models should be projected into the objective space, and Pareto algorithm is implemented to get multiple rank levels. Highly ranked models will be focused, since they are best selections considering multiple objectives at the same time. Finally, cluster analysis is made to select several models from highly ranked models to compose our final model set.

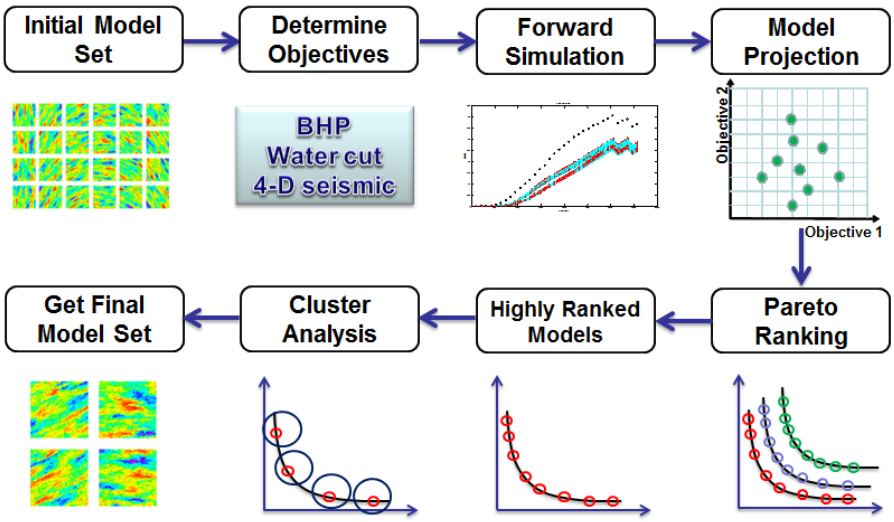

Figure 2-3 Proposed Pareto-based model ranking workflow.

2.4 Illustration of Procedure

To illustrate PBMR, a simple 5 spot synthetic case (one injector in the middle and four producers in the corner) with multiple objectives was developed. The model contains 2500 cells with single layer ($50 \times 50 \times 1$), and six years production history was simulated.

2.4.1 Initial Model Set

Figure 2-4 shows the model generation procedure: first, sequential indicator simulation (SIS) was used to generate facies models, which are composed by floodplain and channel sand; second, porosity model was generated using facies control method to ensure that the property model follows the facies pattern; at last, permeability model was constructed by co-kriging method on porosity model. As such, our initial models are classified into 6 groups based on different azimuth values, and each group includes 17 realizations. Figure 2-5 shows the first 4 realizations for each group. The azimuth value changes every 30

degree, and the differences are very clear between six groups. Our true permeability model is shown in Figure 2-6 (a) and the arrow in the roulette chart in Figure 2-6 (b) is azimuth direction in each group, which corresponds to channel sand trend in Figure 2-5. The red arrow means that our true model comes from group 3.

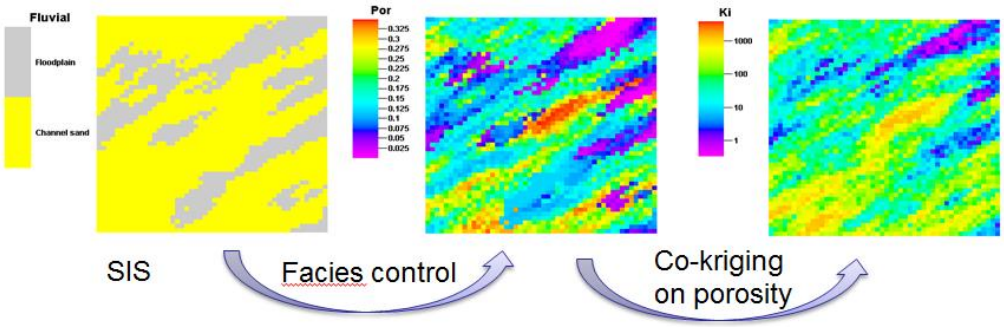

Figure 2-4 Model generation procedure.

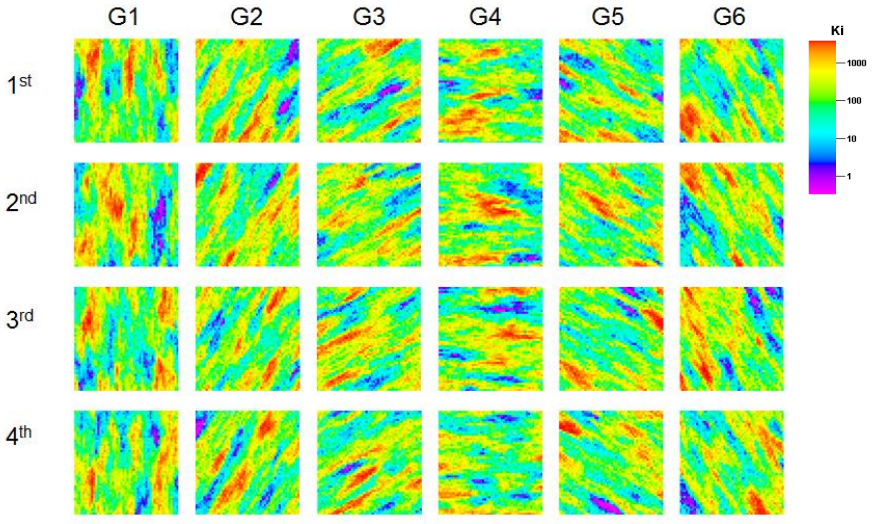

Figure 2-5 First four realizations for six groups.

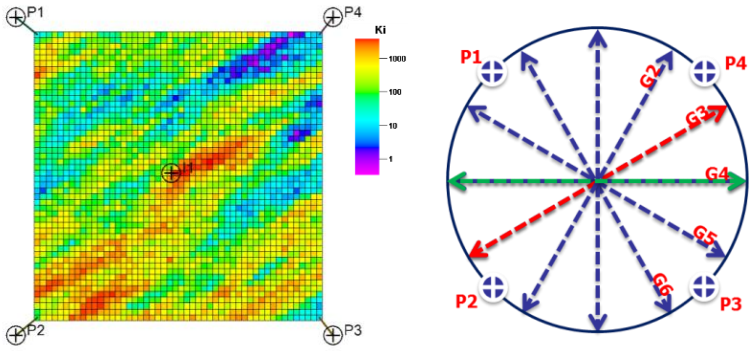

Figure 2-6 (a) Reference permeability field (left) and (b) roulette chart of initial models (right).

2.4.2 Potentially Conflicting Objectives and Forward Simulation

In practice, our objectives may appear conflicting because of the underlying assumptions on variables, measurement errors and uncertainties on the inverted data. To simulate practical situation, seismic objective was intentionally made to conflict with production objectives. The observed production responses: field water cut (Figure 2-7 (a)) and bottomhole pressure (Figure 2-7 (c)) came from group 3 as shown in Figure 2-6 (b) while seismic saturation changes (Figure 2-7 (b)) came from group 4 shown by green arrow (Figure 2-6 (b)). Since the production responses and seismic observed data come from different groups, the corresponding objectives are conflicting, which means if models come from group 3, it should have low water cut misfit and high seismic saturation difference, and models coming from group 4 have a high chance to get high water cut misfit and low seismic saturation difference. Models of the other groups may have relatively small misfit values compared with those of groups 3 and 4. We cannot abandon the models, which have relatively high production misfit or seismic saturation difference,

because they still have high probability to be or close to true model, particularly with limited data.

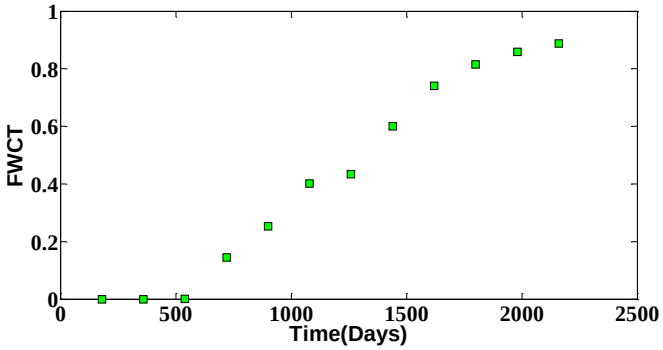

(a) Field water cut observed data.

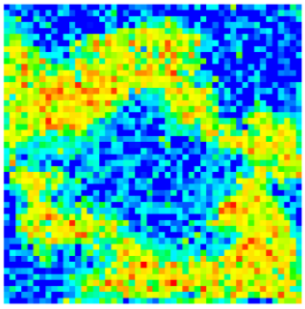

(b) Seismic saturation changes.

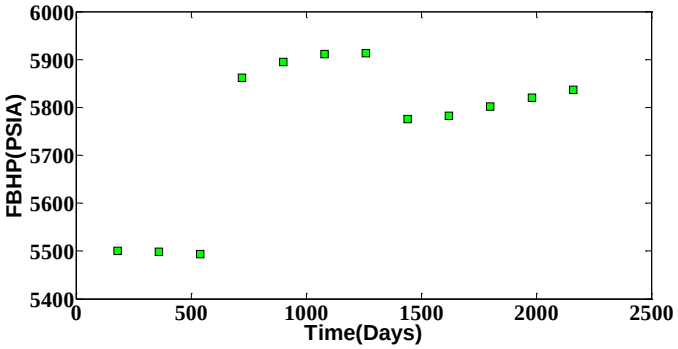

(c) Bottomhole pressure observed data.

Figure 2-7 Production and seismic observed data in synthetic case.

Next step, forward simulation is carried out (Schlumberger 2012) based on our initial model set, and production and seismic responses are generated. Differences are taken between the observed data and responses to get water cut (Figure 2-8 (a)) and BHP misfit (Figure 2-8 (b)). The third objective is seismic saturation differences (Figure 2-8 (c)).

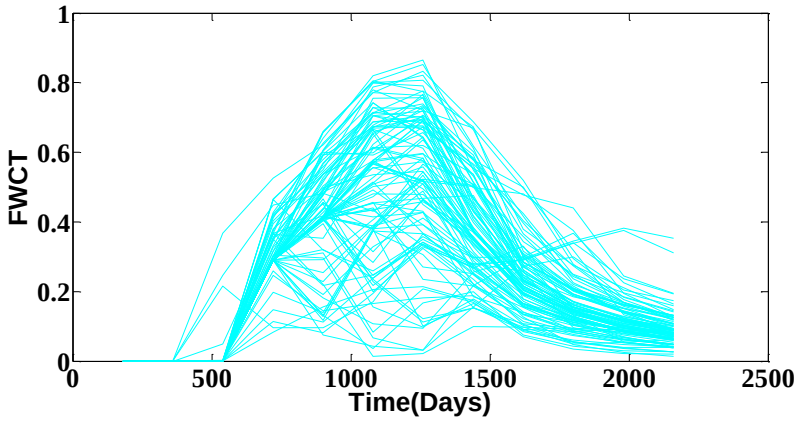

(a) Field water cut misfit versus production time.

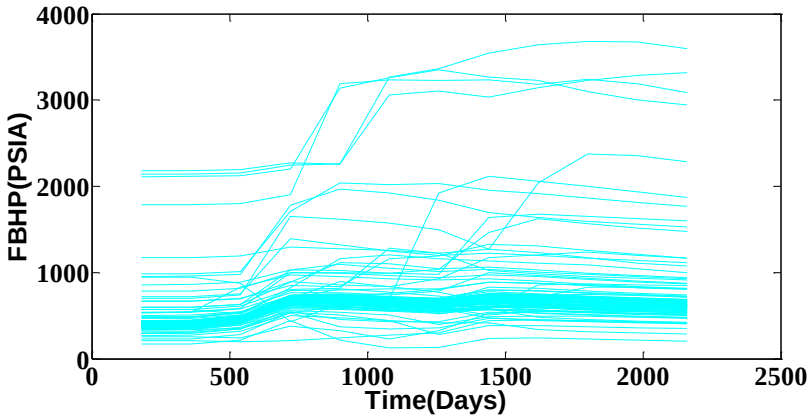

(b) Field bottomhole pressure misfit versus production time.

Figure 2-8 Production misfits and seismic saturation difference in synthetic case.

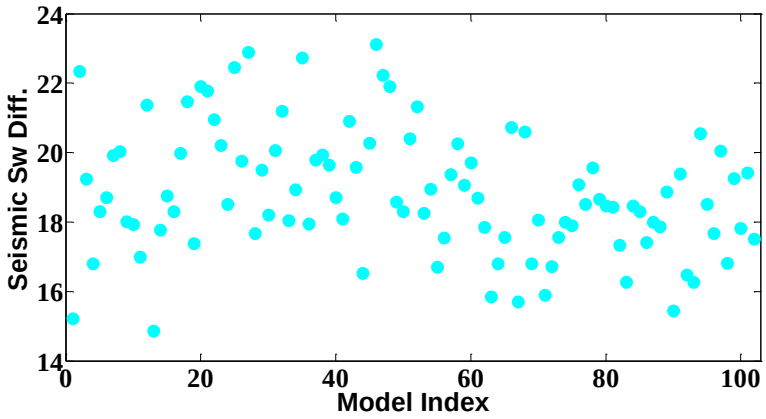

(c) Seismic saturation difference versus model index.

Figure 2.8 continued.

2.4.3 Model Projection and Pareto Ranking

After the three objectives of each model were obtained, we projected our models into BHP, seismic saturation differences, and water cut coordinates, and ranked the models. Six ranking levels are shown in Figure 2-9, where color bar represents different ranking levels, and model index is labeled above the point.

Rank 1 level (dark blue) has included 14 models, which are competitive compared to the other rank level models and spread largely among each objective considering the conflicting characteristic of these three objectives. Thus, we exclude other level models and just focus on rank 1 level. Figure 2-10 (b), (c) and (d) show three 2-D figures, which are projection of 3-D figure of Rank 1 level (Figure 2-10 (a)). The red lines are imaginary Pareto fronts of rank 1 level, which are projection of Pareto surface. As mentioned above, trade-offs of the front reveal conflict between objectives. The large trade-off, such as seismic saturation differences and water cut misfit, indicates that they are conflicting.

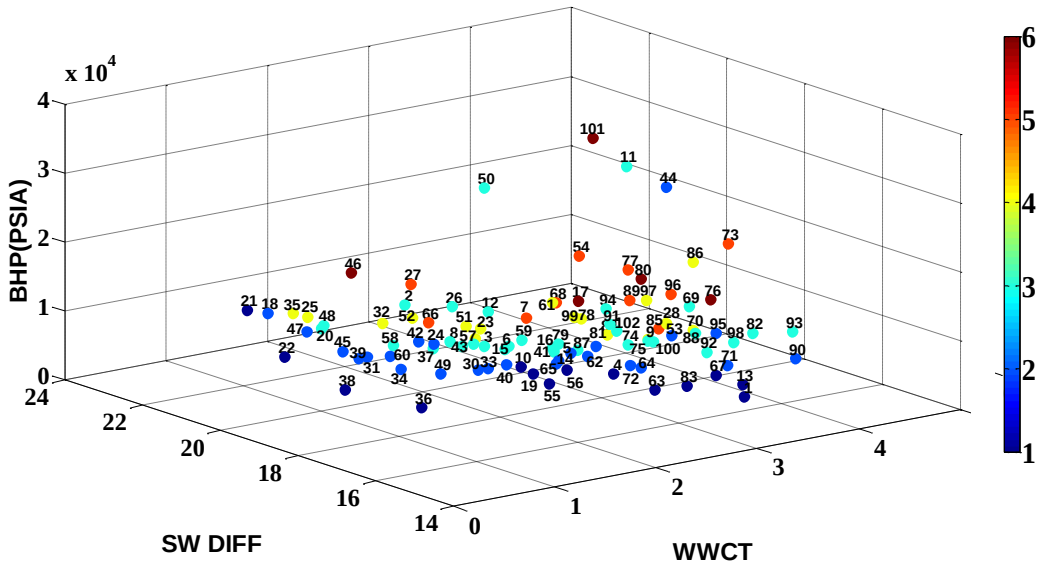

Figure 2-9 Pareto ranking result in synthetic case.

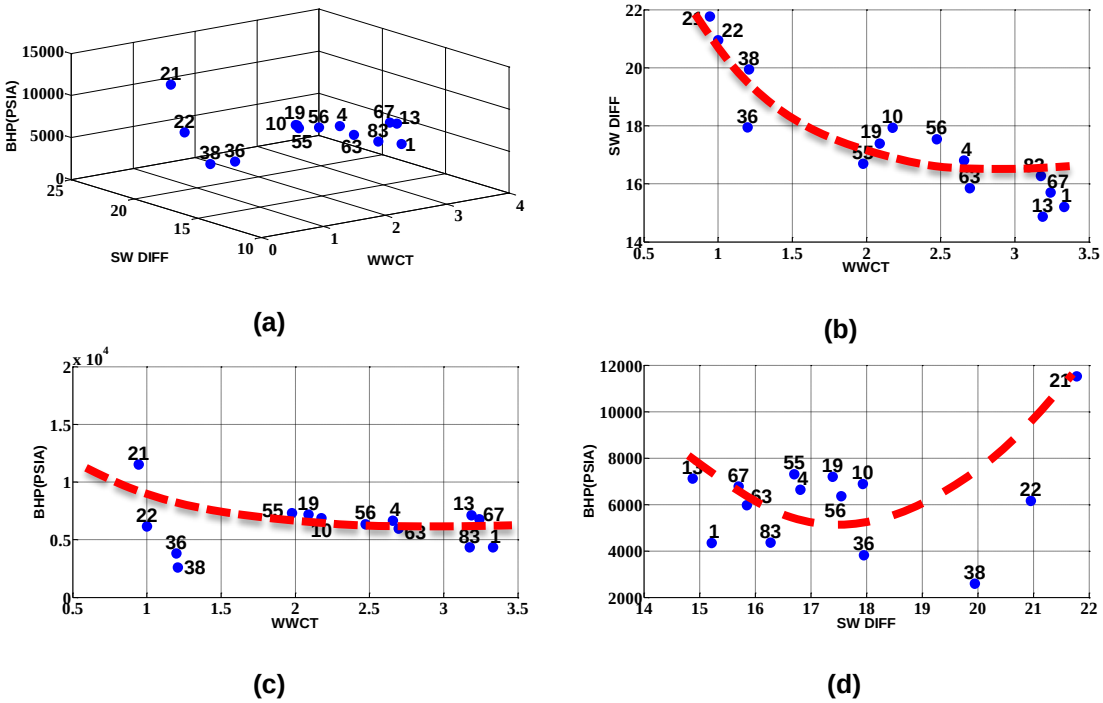

Figure 2-10 Rank 1 models visualization in synthetic case.

2.4.4 Cluster Analysis for Highly Ranked Models

Our model set has been reduced from 102 models to 14 models, which are still too many for decision making. To reduce model set further while preserving model diversity, the K-means clustering is adopted for grouping highly ranked models. In this case, the rank 1 models were grouped into four clusters, and the models which are close to the centroids were selected (Figure 2-11) to keep maximum differences between models.

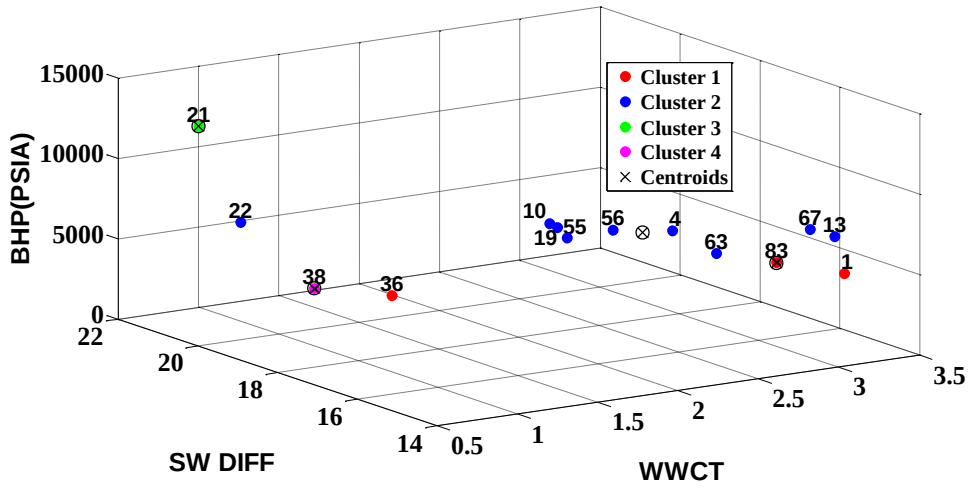

Figure 2-11 Cluster analysis for rank 1 models in synthetic case.

Table 2.1 Selected models in synthetic case

Cluster	Model Index	Group
1	21	2
2	38	3
3	56	4
4	83	5

Table 2.1 shows the models we chose. Model 38 comes from group 3, which is our true model group. The orientation of Group 2 and Group 3 models are symmetric with

respect to well P4 and P2 (or well P1 and P3), and they may have the same production response. Hence, Model 21 coming from group 2 is also a satisfied result. Model 56 comes from group 4, which possess small seismic saturation differences. However, we also include model 83 from group 5. Although it is inevitable to include models from other uncompetitive group, which are not from group 3 and 4, we can capture plausible solutions by PBMR. All the models together we chose here reflect the complementary as well as conflicting characteristic of the three objectives.

Our goal is that we expect to select the models (like model 38) from true model group before history matching. However, in general if the initial model set does not incorporate true models, the models that are close to the true models (like model 21) are our best choices. The advantage of small seismic saturation difference pushes model 56 into our final choices. In this case, we know that group 4 is not the true model group, but in practice, it is difficult to distinguish which group (group 3 or group 4) is true model group in the absence of prior knowledge. We generate Pareto fronts to capture these plausible solutions together, which serve our uncertainty analysis.

Figure 2-12 shows selected models dynamic responses. The red line and red dot are model 21 responses that show the low field water cut misfit, high bottomhole pressure misfit and high seismic saturation differences. Model 83 responses, the black line and dot, show the opposite result for each objective. This phenomenon shows that the models we selected spread largely along the front, and at the same time, the misfit for each objective has been reduced correspondingly. This is the balanced state we want to achieve.

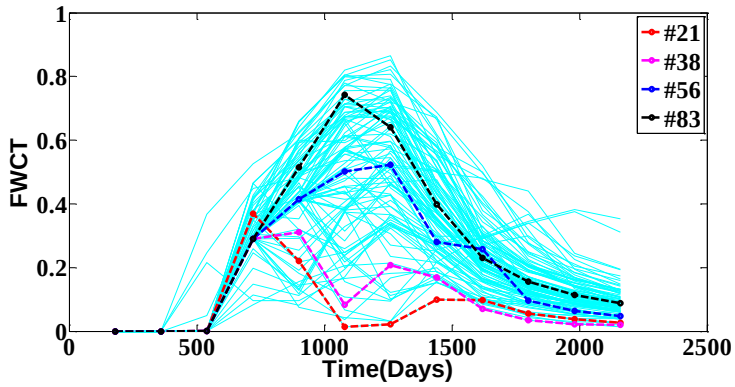

(a) Field water cut misfit versus production time.

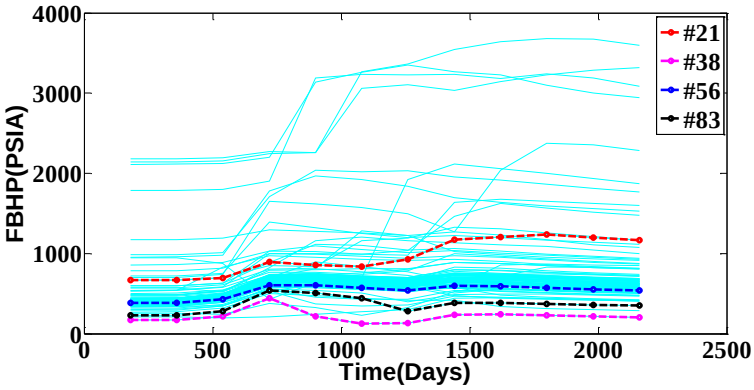

(b) Bottomhole pressure misfit versus production time.

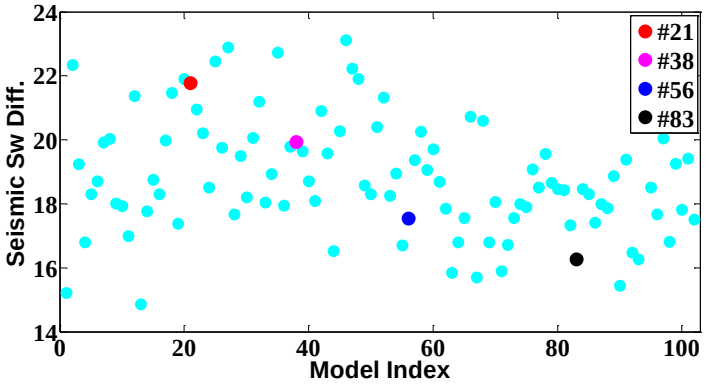

(c) Seismic saturation differences versus model index.

Figure 2-12 Selected models dynamic responses in synthetic case.

2.4.5 Comparison with Weighted Sum Method

To compare with the PBMR method, the weighted sum method (Eq. 2.2) is applied for model ranking with the same initial model set. We assign different weights and pick models which have smallest overall objective (Table 2.2). However, different weight assignments produce various results, and also these solutions are pushed into different limited areas by the weights, causing the result that it may lose some plausible solutions (no models come from group 2 or group 3) while it includes more uncompetitive solutions for the same selected model size (model 76 comes from rank 6).

$$obj = w_1 \times WWCT + w_2 \times BHP + w_3 \times SW\_DIFF \tag{2.2}$$

Table 2.2 Model ranking result with weighted sum method.

Weights	Models	Group	Rank
w_1=1; w_2=1; w_3=1	#56 #76 #85 #91	G4 G5 G5 G6	R1 R6 R5 R3
w_1=1; w_2=1; w_3=0.1	#54 #85 #87 #91	G4 G5 G6 G6	R5 R5 R3 R3
w_1=1; w_2=1; w_3=0.01	#10 #54 #85 #56	G1 G4 G5 G4	R1 R5 R5 R1

2.5 Field Application

Brugge field has one fault at the north edge, going through nine layers with 60048 grids. There are twenty producers, which are surrounding by eight water injectors, each providing the observation data for ten years. 104 realizations are classified into eight groups based on different geostatistical methods (Table 2.3).

In the Brugge case, the groups which are close to the true model group are unknown. To select competitive models (closer to the original point relatively), which can preserve the conflicting information given chosen objectives, the PBMR workflow is employed to

the Brugge field model ranking. Objectives are the same as those of synthetic case: water cut misfit, bottomhole pressure misfit, and seismic saturation difference. Through forward simulation, corresponding responses are shown in Figure 2-13.

Then we project models and implement Pareto ranking. Six ranking levels are obtained shown in Figure 2-14.

Table 2.3 Brugge model set with different geostatistical methods.

Geostatistical methods			
1. FY-SF-KM	2. FY-SF-KS	3. FY-SF-KP	4. FY-SS-KM
5. FY-SS-KS	6. FY-SS-KP	7. FN-SS-KS	8. FN-SS-KP

Terms explanation		
1st term: Facies	2nd term: Fluvial	3rd term: Perm. Poro.
- FY: Classify facies	- SF: Single shale	- KM: Regression per facies
- FN: Ignore facies	- SS: Sequential indicator simulation	- KS: Single regression - KP: Co-kriging on porosity

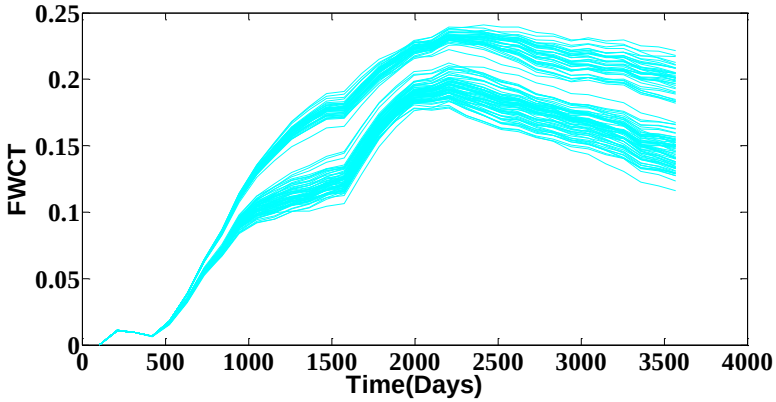

(a) Field water cut misfit versus production time.

Figure 2-13 Production misfit and seismic saturation difference in Brugge case.

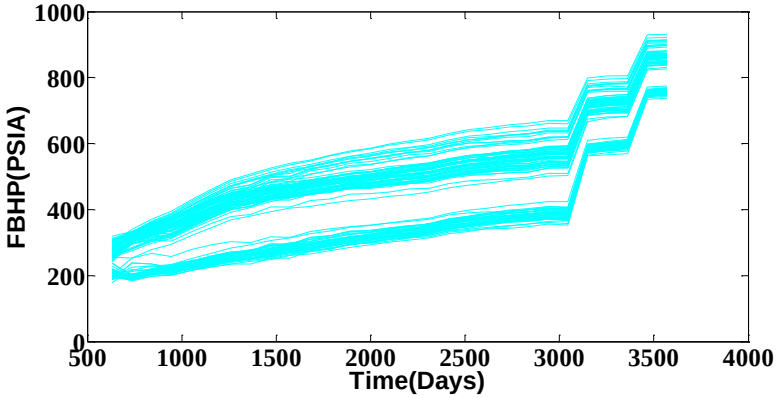

(b) Field bottomhole pressure misfit versus production time.

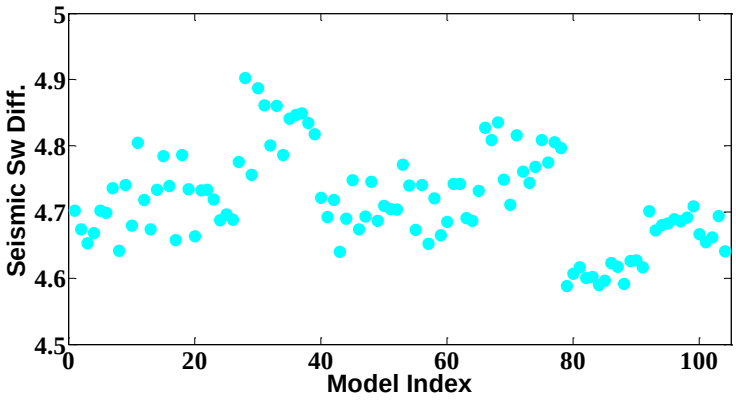

(c) Seismic saturation difference versus model index

Figure 2.13 continued.

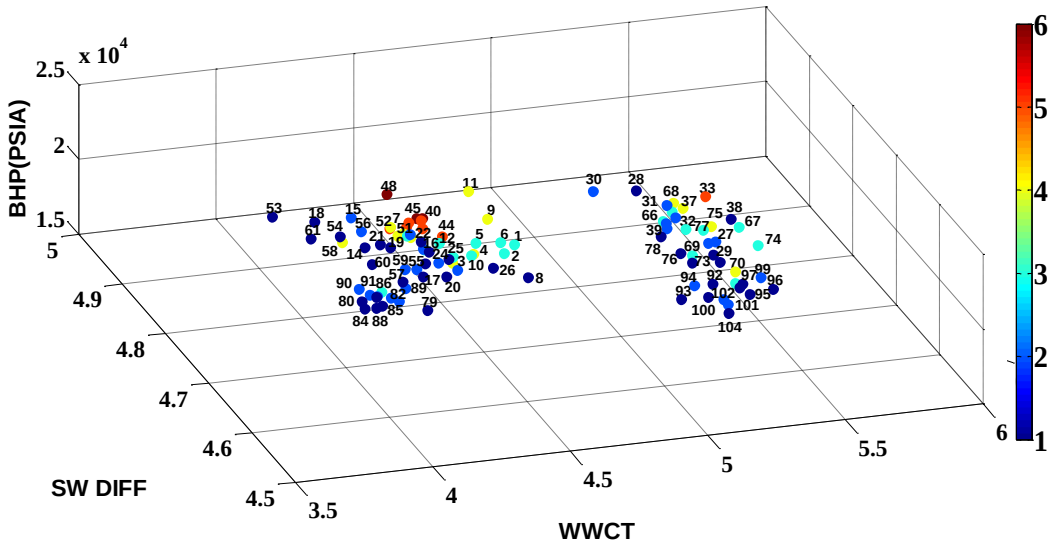

Figure 2-14 Pareto ranking result in Brugge case.

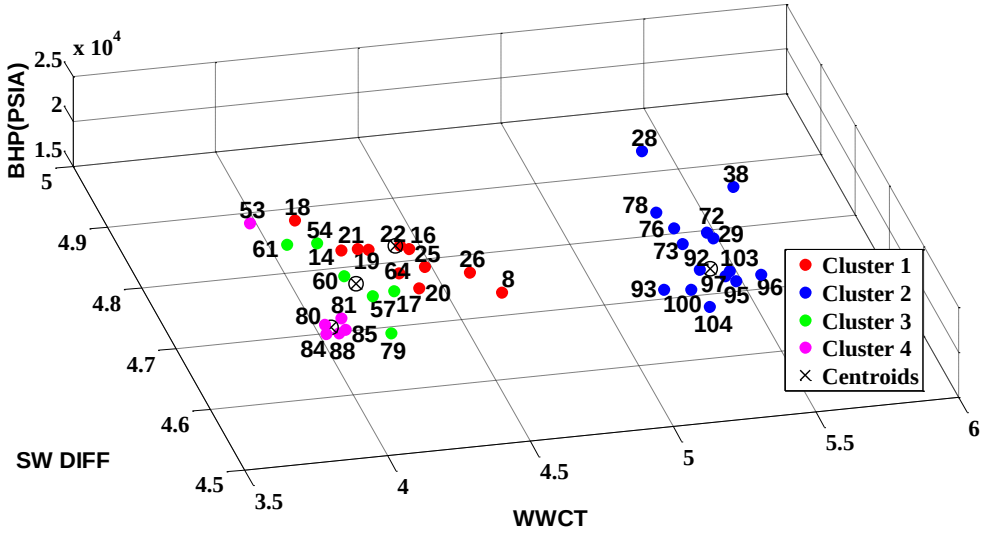

Figure 2-15 Cluster analysis for rank 1 models in Brugge case.

Since rank 1 level includes 38 models, regarded as highly ranked models, we ignore models from the other rank level. The K-means clustering algorithm is used to reduce models number from 38 to 4 (Figure 2-15). The selected models come from group 2, 5, 7,

and 8 (Table 2.4). Their permeability and dynamic responses are shown in Figure 2-16 and Figure 2-17 respectively. In Figure 2-17, the four colored lines are dynamic responses of selected models. Uncertainty range is reduced for each objective, and it reflects the complementary as well as conflicting characteristic between objectives.

Table 2.4 Selected models in Brugge case

Cluster	Model Index	Group
1	22	2
2	60	5
3	80	7
4	92	8

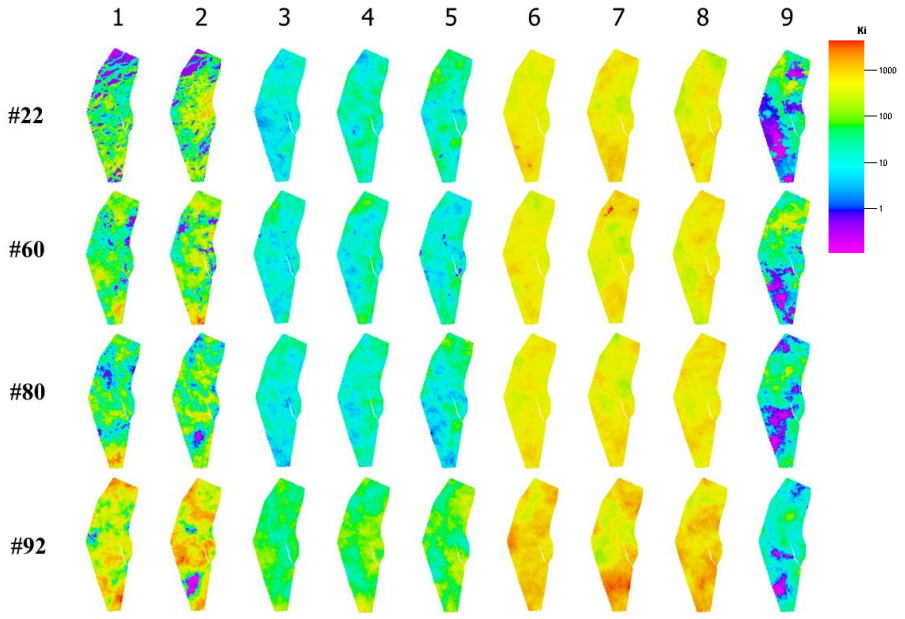

Figure 2-16 Selected models permeability field in Brugge case.

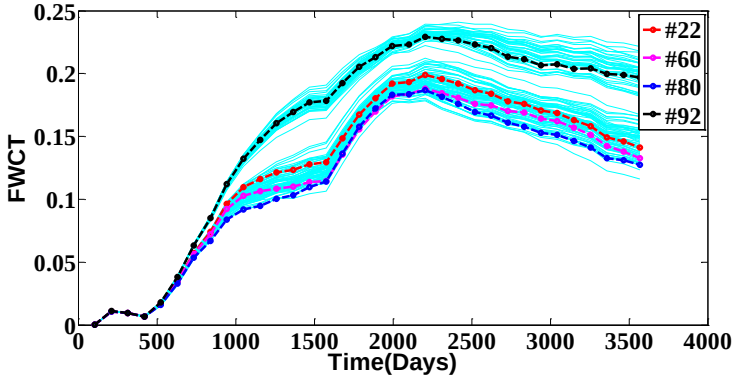

(a) Field water cut misfit versus production time.

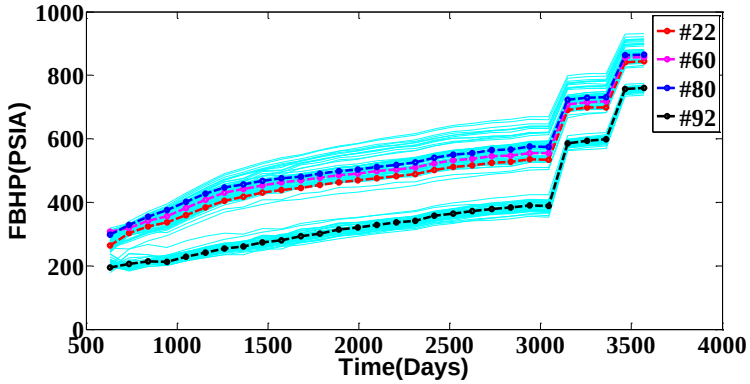

(b) Bottomhole pressure misfit versus production time.

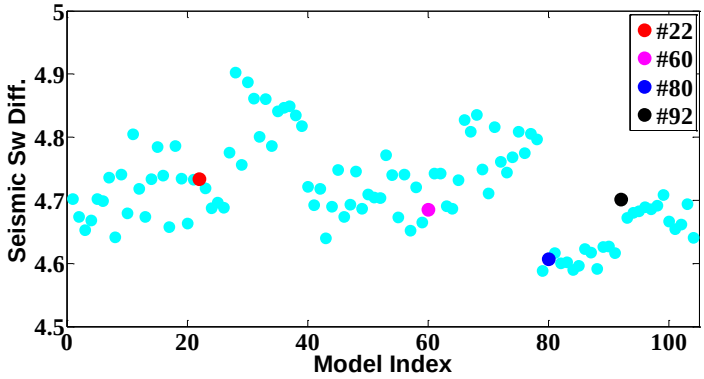

(c) Seismic saturation differences versus model index.

Figure 2-17 Selected models dynamic responses in Brugge case.

2.6 Summary

In this chapter, we proposed a Pareto-based modeling ranking approach to rank geological models considering multiple sources of data: production and seismic. We tested the PBMR approach on a 2-D synthetic example and then applied it to the SPE benchmark Brugge field with three types of dynamic data: bottom-hole pressure, field water cut and 4-D seismic derived saturation differences. For all cases, we demonstrated the benefits of the proposed PBMR approach for model ranking. The main findings are summarized as follows:

1. The Pareto-based approach can effectively handle multiple objectives to avoid interference between them. In this way, we get more accurate and comprehensive model set solution: complementary as well as conflicting characteristic of multiple objectives can be preserved, selected models are competitive, and uncertainty range can be effectively analyzed for each objective.
2. The weighted-sum method may lose some plausible solutions and include more uncompetitive solution simultaneously, because different weight assignments will push these solutions into different limited areas. Moreover, the weighting factor determination is avoided by PBMR.
3. Cluster analysis is useful to reduce the plausible model set while keeping the model spread in the absence of prior knowledge. We can also pick several favorable models from highly ranked models based on the prior knowledge of the field.

CHAPTER III

PARETO-BASED MULTIOBJECTIVE HISTORY MATCHING AND POLYMER OPTIMIZATION: APPLICATION TO NORNE FIELD*

In this chapter, we apply a hierarchical history matching workflow consisting of global and local updates, followed by polymer optimization on the Norne Field, North Sea. Both history matching and production optimization are performed under the multiobjective framework, considering the potential conflicting objectives features. In the history matching part, 4-D repeat seismic surveys are efficiently integrated with well production data: globally, both seismic (acoustic impedance change misfit) and production objectives (cumulative field water & gas production misfit) are minimized using the Pareto-based multiobjective evolutionary algorithm (MOEA) (Park et al. 2013), coupled with the Grid Connectivity Transform (GCT) (Bhark et al. 2011b) parameterization; locally, pressure and saturation effects on acoustic impedance changes are considered sequentially based on streamline-based sensitivity approach, and water cut data is finally integrated by the streamline-based generalized travel time inversion (GTTI) (He et al. 2002). In the polymer optimization part, production and injection rates are allocated using the streamline-based rate optimization for maximizing sweep efficiency, and then the MOEA is applied to

*Part of the data reported in this chapter is reprinted with permission from "Streamline-Based Time Lapse Seismic Data Integration Incorporating Pressure and Saturation Effect" by Watanabe, S., Han, J., Datta-Gupta, A. et al. 2013: Paper SPE-166395-MS Presented at the SPE Annual Technical Conference and Exhibition, 30 September – 2 October New Orleans, Louisiana, USA. Copyright 2014 Society of Petroleum Engineers.

optimize polymer concentration and slug size for maximizing oil production while preserving high polymer usage efficiency.

3.1 Introduction

History matching is used to calibrate geologic models under the guidance of seismic and production data for more accurate prediction of future production. The more accurate the geologic models are through history matching, the more reliable the prediction of reservoir performance is. Instead of manual history matching method, which is impractical for large and complex fields, the assisted history matching (AHM) method has drawn a lot of attention over the past decades. The AHM mainly includes the gradient-based methods, sensitivity-based methods, and derivative-free methods in terms of minimizing the difference between simulation and observed data. The gradient-based methods, such as the Levenberg–Marquardt, BFGS, and limited-memory BFGS, are efficient when the objective function is sufficiently smooth, but are inappropriate for discrete properties (Gao and Reynolds 2006; McCormick and Tapia 1972). Also, the convergence of gradient-based methods is typically very slow. Instead, the sensitivity-based methods can converge faster. In particular, the streamline-based GTTI (Wu and Datta-Gupta 2002) approach has been widely adopted in many field applications (Cheng et al. 2005; Kam and Datta-Gupta 2014; Tanaka et al. 2015). These deterministic techniques, such as the gradient-based and sensitivity-based methods, are easily trapped in the local optimum, and are not robust for the uncertainty analysis. In contrast, the derivative-free methods, such as the genetic algorithm (Holland 1992) and Markov Chain Monte Carlo (MCMC) (Hastings 1970), are

powerful to search global optimum for the complex reservoir models, and more effectively quantify the uncertainty by providing more alternative simulation models without requiring any gradient calculation. The disadvantage of derivative-free methods is that the computation is highly prohibitive because of plenty of simulation running requirement, especially for relatively large number of parameters to be updated.

In practice, history matching always involves multiple objectives. The traditional technique typically aggregates all the objectives into the single objective space, called the weighted-sum method, regardless of whether these objectives conflict. It will be problematic for the weighted-sum method when the objectives are conflicting. The more conflicting the objectives are, the worse results weighted-sum method produces. Weighted-sum method reduces the objectives solution space, and each objective is tied with each other, resulting that the original solution space cannot be preserved. Moreover, the weighting factor assignment for each objective is very subjective, mainly relying on the prior knowledge and degree of confidence. Cheng et al. (2008) used weighted sum of squares difference between the observed values and calculated model values for joint integration of static gradient surveys (SGS) and modular dynamic tests (MDT) pressure data. Rey et al. (2012) applied a penalized misfit function in which the weighting factors control the balance between production and seismic data misfit. Similarly, Denney (2012) assigned different weighting factors for production misfit and seismic misfit respectively.

Similar issues can be found in the polymer optimization. Polymer injection during water flooding can effectively reduce viscous fingering and increase sweep efficiency by decreasing the mobility of the injected water, which results from the increase of water

viscosity and reduction of rock permeability to water. The objective of polymer optimization is to maximize the net present value (NPV) (Van Doren et al. 2011). To evaluate polymer performance, generally, oil production improvement after injecting polymer can be used as a measurement. Polymer utility factor (UF), which the ratio between the total injected polymer and incremental oil production, is also proven to be an effective measurement for polymer usage efficiency (Clemens et al. 2011). Unfortunately, large oil production improvement always comes with poor polymer usage efficiency. It is a challenge to find an optimal solution considering oil production improvement and UF.

To solve the above issues, the Pareto-based concept, which is used for the model ranking, is incorporated into the MOEA, contributing to finding multiple representative Pareto-optimal solutions instead of solutions biased toward some preferred objective (Deb et al. 2002; Li and Zhang 2009; Srinivas and Deb 1994). Mohamed et al. (2011) developed the Multi-Objective Particle Swarm Optimisation approach (MOPSO) which coupled the Pareto-based algorithm with particle swarm method to keep the solution diversity. Park et al. (2013) replaced the classical genetic algorithm with the Pareto-based MOEA to update the GCT coefficients in the hierarchical workflow framework for history matching with potentially conflicting objectives.Olalotiti-Lawal and Datta-Gupta (2015) proposed a multiobjective MCMC approach to sample multiple trade-off solutions along the Pareto front for history matching and uncertainty quantification.

Here, we will apply the Pareto-based framework to the history matching and production optimization of the Norne Field. The outline of this chapter is as follows. We start with the reservoir description of the Norne Field. Then we show the global update

application of history matching in the Norne Field, coupled with the Pareto-based genetic algorithm and GCT. Seismic objective involved in the workflow includes the petro-elastic modeling level seismic data integration and time-lapse acoustic impedance change derived from the post-stack seismic amplitude date. Next, we apply the local update workflow into fine-scale tuning of the Norne Field using the streamline-based analytic sensitivities for fluid saturation and pressure data integration. Finally, based on the history-matched models obtained above, production is optimized on the Norne Field through the streamline rate optimization, followed by the multiobjective polymer optimization.

3.2 Norne Field Description

The Norne Field, located in North Sea, was discovered in December 1991, and started oil production in November 1997. High quality 4-D seismic data and production data are available in the field. Horizontally, there are Norne C, D, E, G segments, and vertically five reservoir zones are Garn, Not, Ile, Tofte and Tilje. The sandstones are buried at the depth of 2500-2700 m. Porosity and permeability are 25-30% and 20-2500 md respectively (Osdal et al. 2006; Rwechungura et al. 2012; Steffensen and Karstadt 1996).

We demonstrate the practical feasibility of our approach by carrying out full field history matching of the Norne Field. The reservoir model includes 44431 active cells, and it contains 36 wells (9 injectors and 27 producers) as shown in Figure 3-1. We consider the time frame from 1997 to 2006 as the history matching period and from 2006 to 2016 as the production optimization period. The actual simulation model containing all information and properties was provided by the operator. In addition, production and

injection data from 1997 to the end of 2006 and multiple sets of 4-D seismic data for the same period (2003-2001, 2004-2003, 2006-2004) were provided. The production data includes water, oil, and gas rates and bottom-hole pressures at the producers. The seismic data were externally processed and provided for the model calibration as near, mid, far, and full offset stacked 3-D volumes of the reflection amplitude together with the corresponding horizons for the top and base of the reservoir. Also, the time-lapse differences of the reflection amplitude were provided with interpreted horizons used for identification of movement of the water-oil contacts. More details of the data set can be found in Rwechungura et al. (2012).

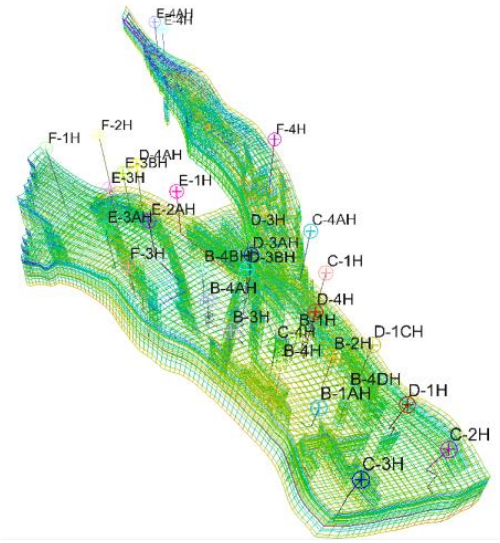

Figure 3-1 Norne Field skeleton model.

3.3 Global Update Step: Pareto-based Multiobjective Evolutionary Algorithm Workflow

In the global step, we couple the Pareto-based genetic algorithm and the GCT parameterization to calibrate permeability field by minimizing the seismic and production

objective misfits in the Norne Field. First, we introduce the petro-elastic model (PEM) and seismic data processing procedure for the acoustic impedance change misfit calculation, and then present the GCT parameterization and the MOEA methodology. Global update results on the Norne Field using the mentioned approaches are shown in the end.

3.3.1 Petro-Elastic Model

A petro-elastic model is a set of equations, such as the Gassmann equation (Gassmann 1951) and Hertz-Mindlin contact theory (Mindlin 1949), which relates reservoir properties (pore volume, pore fluid saturations, reservoir pressures and rock composition) to seismic rock elastic parameters (P-wave and S-wave velocities, V_p and V_s, respectively) (Mohsen et al. 2009).

The Hertz-Mindlin model is used to compute seismic rock elastic parameter changes from pressure changes (Mavko et al. 1998). The effective bulk modulus of a dry random identical sphere pack can be computed as

$$K_{HM} = K_{ma} \sqrt[n]{P_{eff}/(P_{ext} - P_i)} \tag{3.1}$$

where K_{HM} is the bulk modulus at critical porosity (Dadashpour et al. 2009). Here, P_{eff} is the effective pressure, K_{ma} is the bulk modulus of the matrix, and n is the coordination number. In the Norne Field application, P_{eff} is the difference between the lithostatic pressure P_{ext} and the hydrostatic pressure P (Christensen and Wang 1985), K_{ma} is given in Table 3.2, n is set to five based on the literature (Dadashpour et al. 2009), the initial

pressure is taken as 270 bar, and the lithostatic pressure is written as a function of the true vertical depth (TVD) shown by Eq. 3.2 (Mohsen et al. 2010).

$$P_{\text{ext}} = 0.0981.(9 \times 10^{-5} \times \text{TVD} + 1.7252) \times \text{TVD} \tag{3.2}$$

The Gassmann equation expresses the bulk modulus of a fluid saturated rock from three terms: (1) the bulk modulus of the mineral matrix K_{HM}, (2) the bulk modulus of the porous rock frame K_{fr}, (3) the bulk modulus of the pore-filling fluids K_{f} as given by the following formula (Dadashpour et al. 2009),

$$K_{\text{sat}} = K_{\text{fr}} + \frac{(K_{\text{HM}} - K_{\text{fr}})^2}{K_{\text{HM}}\left(1 - \phi + \phi\frac{K_{\text{HM}}}{K_{\text{f}}} - \frac{K_{\text{fr}}}{K_{\text{HM}}}\right)} \tag{3.3}$$

ϕ is the effective porosity, and K_{f} is calculated shown below (Reuss 1929)

$$\frac{1}{K_{\text{f}}} = \frac{S_{\text{o}}}{K_{\text{o}}} + \frac{S_{\text{w}}}{K_{\text{w}}} + \frac{S_{\text{g}}}{K_{\text{g}}} \tag{3.4}$$

Here K_{o}, K_{w}, and K_{g} are oil, water, and gas bulk moduli respectively, and S_{o}, S_{w}, and S_{g} are oil, water, and gas saturations, respectively. The density of the saturated rock is given by the weighted average of the densities of the components (Vasco et al. 2003):

$$\rho_{\text{sat}} = (1 - \phi)\rho_{\text{ma}} + \phi\left(S_{\text{o}}\rho_{\text{o}} + S_{\text{w}}\rho_{\text{w}} + S_{\text{g}}\rho_{\text{g}}\right) \tag{3.5}$$

Here ρ_{o}, ρ_{w}, ρ_{g}, and ρ_{ma} are the densities of oil, water, gas, and the rock matrix, respectively. With the saturated rock bulk modulus, shear modulus, and density, we can compute the compressional (p-wave) velocity for an isotropic, layered, elastic medium (Kennet 1983) as

$$V_{\text{p}} = \sqrt{\frac{K_{\text{sat}} + \frac{4}{3}G_{\text{fr}}}{\rho_{\text{sat}}}} \tag{3.6}$$

Here the shear modulus, G_{fr}, is the frame shear modulus, which is not affected by fluid saturations. The acoustic (p-wave) impedance can be computed as

$$Z_{\mathrm{p}} = \rho_{\mathrm{sat}} V_{\mathrm{p}} = \sqrt{\rho_{\mathrm{sat}} \left(K_{\mathrm{sat}} + \frac{4}{3} G_{\mathrm{fr}} \right)} \tag{3.7}$$

For the Norne Field application, all the parameters for petro-elastic model are provided in Table 3.1, Table 3.2 and Table 3.3. With the above PEM model for the Norne Field application, we examined the sensitivity of the acoustic impedance with pressure and saturation changes. In a simple two phase (oil, water) system, Figure 3-2 (a) shows the increase of acoustic impedance with increasing water saturation for a fixed pressure. Figure 3-2 (b) shows the decrease of acoustic impedance with increasing pressure with fixed saturation values.

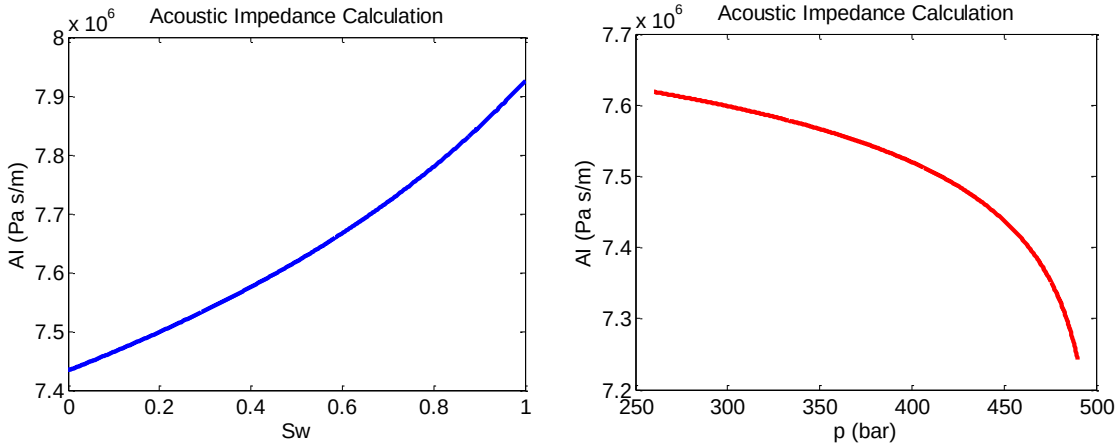

Figure 3-2 Acoustic impedance calculation sensitivity by PEM model in oil and water two phase system, (a) with respect to water saturation changes under a fixed pressure (P=270 bar) and (b) with respect to pressure changes under a fixed saturation value (Sw=0.5).

Table 3.1 Shale properties for the petro-elastic model in Norne Field.			
Parameters	Shale type 1	Shale type 2	Shale type 3
P-wave velocity, V_p , [m/s]	3200	3350	3350
S-wave velocity, V_s , [m/s]	1600	1800	1900
Shale density, ρ , [kg/m^3]	2300	2450	2450

Table 3.2 Sand properties for the petro-elastic model in Norne Field.		
Parameters	Garn formation (lay 1-3)	Garn formation (lay 5-22)
Frame bulk modulus, K_{fr} , [Gpa]	18.8-36.8 ϕ	18.5-27.4 ϕ
Frame shear modulus, G_{fr}, [Gpa]	11.8-21.4 ϕ	10.9-13.0 ϕ
Matrix bulk modulus, k_{ma}, [Gpa]	37	37
Matrix density, ρ , [kg/m^3]	2650	2650

Table 3.3 Fluid properties for the petro-elastic model in Norne Field.	
Parameters	Fluid bulk modulus when temperature = 98.3^o (Batzle and Wang 1992) and Fluid density
Oil bulk modulus, K_o , [Gpa]	1.35
Water bulk modulus, K_w, [Gpa]	2.79
Gas bulk modulus, K_g, [Gpa]	6.49×10^{-2}
Oil density, ρ_o , [kg/m^3]	860
Water density, ρ_w , [kg/m^3]	1000
Gas density, ρ_g , [kg/m^3]	190

3.3.2 Seismic Data Processing

In our data calibration procedure, the seismic volumes of reflection amplitude needs to be inverted to changes in acoustic (p-wave) impedance. Using commercial software, we

conduct seismic data processing, which consists of (1) time to depth data conversion, (2) well log quality check and acoustic impedance log calculation, and (3) genetic inversion for generating an acoustic impedance map from the seismic amplitude data. As for the post-stack seismic sections, we decided to use near-offset stacking data set, because the acoustic (p-wave) impedance changes are more evident in the small angle reflection waves in AVO analysis (Aki and Richards 1980).

Time to depth data conversion is achieved by using a velocity model that the operator used for the reservoir model construction. The layering of the reservoir model is consistent with the depth converted seismic amplitude data as shown in Figure 3-3. Well log data quality is reviewed especially for the density logs and the sonic logs with the aim of computing acoustic impedance at the well locations shown in Figure 3-4. We adapt a genetic inversion of the seismic amplitude, as proposed by Veeken et al. (2009). The method only requires the post-stack seismic cube as input. The acoustic impedance logs at the wells are used as training data for a neural network to construct the non-linear operator that transforms the seismic traces into the equivalent acoustic impedance response. The weights of the operator are updated by a genetic algorithm to minimize the difference between the predicted acoustic impedance response and the training acoustic impedance logs at wells. The seismic cube can be transformed to acoustic impedance map estimates using the neural network derived operator (Figure 3-5). The acoustic impedance changes correspond to the interpreted motion of the water oil contact between surveys. They are consistent with the PEM model responses: the positive change reflects the aquifer encroachment and the negative change below the water oil contact corresponds to the

simulated pressure increases in Figure 3-5. The cross validation of the predicted acoustic impedance values from the genetic inversion and the training acoustic impedance logs show overall agreement (Figure 3-4).

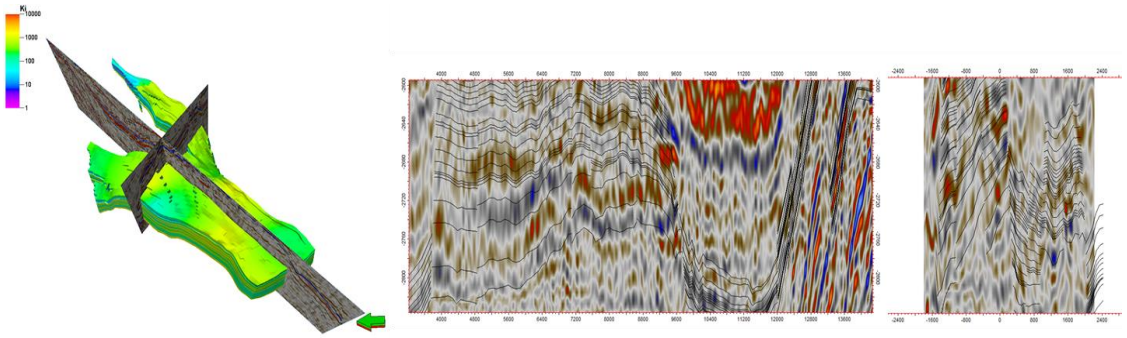

(a) (b) (c)

Figure 3-3 Time to depth data conversion. (a) Reservoir model intersected by the depth domain seismic amplitude inline and crossline slices, (b) the inline slice with reservoir model layer horizons, and (c) the crossline slice with reservoir model layer horizons.

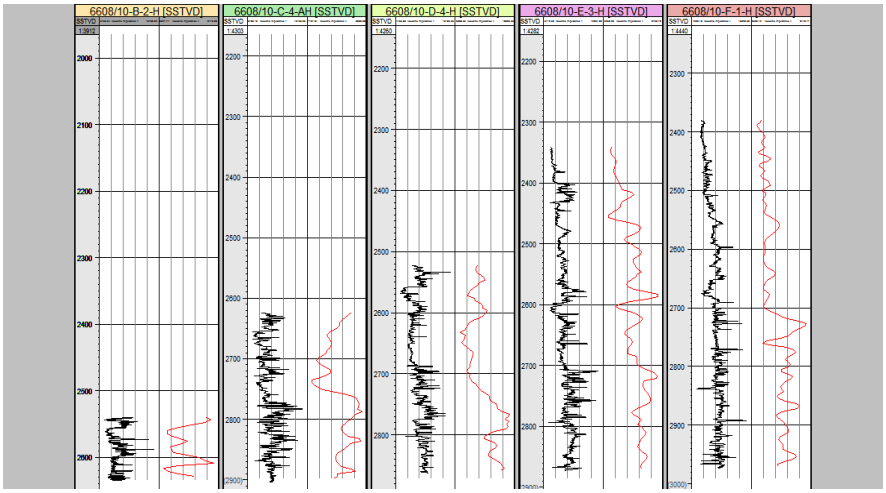

Figure 3-4 The acoustic impedance log comparisons. The black line is the calculated acoustic impedance log, and the red line is the response taken from the acoustic-impedance cube through genetic inversion.

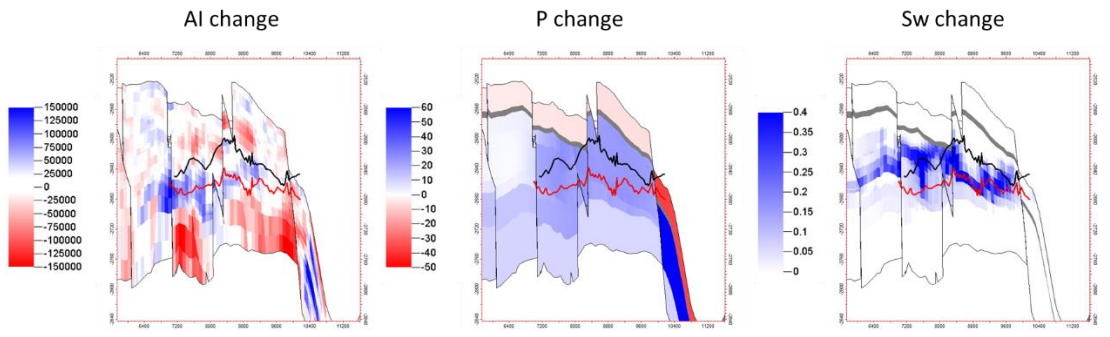

Figure 3-5 Acoustic impedance change data in an inline slice between 2003 and 2001 surveys from genetic inversion. Water oil contact interpretations are superimposed (red line is at 2001 survey and black line is at 2003 survey). The water saturation and pressure changes from the initial model are compared.

3.3.3 Grid Connectivity Transform Method

The Grid Connectivity Transform is a linear transformation from spatial domain to spectral domain, where the heterogeneity is updated based on eigen-decomposition Laplacian/connectivity matrix (Bhark et al. 2011b; Bhark et al. 2012). The property field can be parameterized into the linear combination of the GCT coefficients, which are constructed from the eigenvalues of a grid Laplacian, and the GCT bases, which are eigenvectors of the Laplacian matrix. A property field can be mapped into the spectral domain through orthogonal basis,

$$\mathbf{v} = \mathbf{\Phi}^{\mathbf{T}}\mathbf{u} \Leftrightarrow \mathbf{u} = \mathbf{\Phi}\mathbf{v} \tag{3.8}$$

where $\mathbf{u}$ is $N\times1$ dimension property in the spatial domain, such as permeability or porosity. The column vector $\mathbf{v}$ is the M-length GCT coefficient in the spectral domain, and $\mathbf{\Phi}$ is a ($N\times M$) matrix, containing M-column that defines the discrete basis functions with length N. Take single layer permeability of the Norne Field for example (Figure 3-6), permeability field is parameterized into linear combination of the first 15 GCT coefficients

v and the GCT bases **Φ**. The first GCT basis is a constant vector, corresponding to the reservoir average energy. The latter GCT basis contains high frequency information, helping depict the heterogeneity of the reservoir.

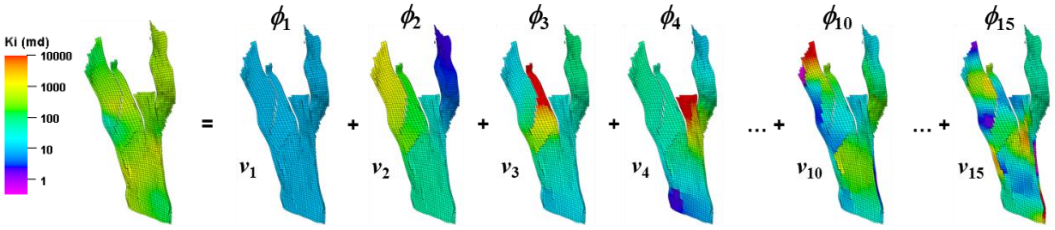

Figure 3-6 GCT parameterization illustration of single layer in the Norne Field.

In history matching calibration, this parameterization method can efficiently reduce parameter dimensionality and enhance spatial continuity/smoothness of the property. **Φv** acts as the spatial multiplier field in Eq. 3.9,

$$\mathbf{u} = \mathbf{u_0} \circ \mathbf{\Phi v} \tag{3.9}$$

where $\mathbf{u_0}$ is the initial or prior property field, and (∘) is the Schur product operator, which means element-wise product between $\mathbf{u_0}$ and **Φv**. It can honor the prior permeability heterogeneity in the model updates.

3.3.4 Pareto-based Genetic Algorithm with GCT

For the global updates, the geological model is first parameterized using the GCT. A few bases are selected to represent the main spatial information of the reservoir in order to reduce dimension of parameters. Then, the corresponding GCT coefficients are updated by a Pareto-based multi-objective history matching workflow (Park et al. 2013), leading to the global changes in the geologic model.

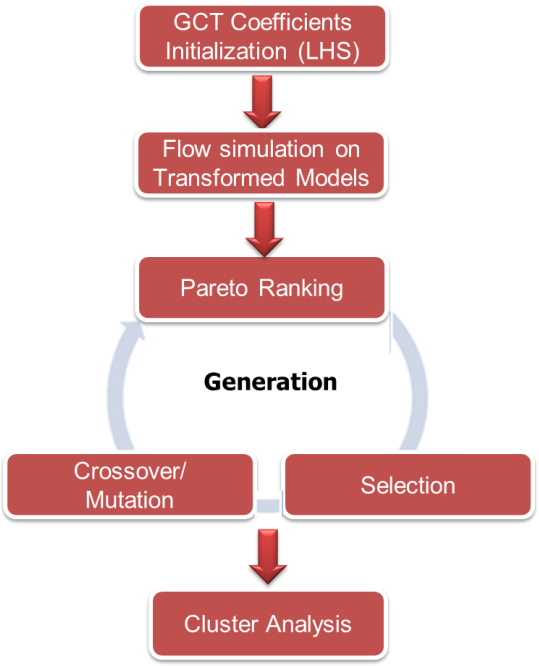

Figure 3-7 Global history matching workflow.

As shown in Figure 3-7, initial populations (GCT coefficients **v**) are generated using the Latin hypercube sampling (LHS) to maximally stratifying each variable's marginal distribution (Yin et al. 2010). Next, all the transformed models from spectral space are fed into forward reservoir simulation running, generating well production responses and pressure and saturation distributions for the history matching objectives calculation. Further, all the models are sorted based on Pareto algorithm to get multiple rank levels in the objective space. Only GCT coefficients from highly ranked models are selected to be utilized by genetic operations: crossover and mutation. It is then followed by the transformation of the new generated the GCT coefficients from spectral domain to spatial domain for the next generation evaluation. The iterations continue until reaching stopping criteria. Finally, the cluster analysis is implemented to select several models for further

local updates. This approach is particularly well suited for minimizing the multiple and potentially conflicting objectives involved in matching both seismic data and production data.

3.3.5 Global Update on the Norne Field

The reservoir model provided by the operator was already calibrated to match the reservoir energy (regional pressure and pore volume). Our objective was to minimally update the permeability at locations and scales required to improve the history matching performance further.

Based on the global update workflow (Figure 3-7), we first parameterize the permeability field by each layer individually to preserve the vertical stratification. The GCT parameterization of a multiplier field is shown in Figure 3-8. In this case, we used a total of 420 coefficients (20 basis vectors per layer × 21 active layers) to represent the geologic model consisting of 44431 active cells. As for the Pareto-based multi-objective minimization, we define three objective functions: (1) grid block acoustic impedance change misfit $(AI = Z_p)$, (2) cumulative field water production ($FWPT$) misfit, and (3) cumulative field gas production ($FGPT$) misfit expressed as

$$obj1 = \sum_{time=1}^{3} \sqrt{\sum_{i=1}^{Ncell} \left(\delta AI_{i,time}^{obs} - \delta AI_{i,time}^{cal}\right)^2} \tag{3.10}$$

$$obj2 = \sum_{j=1}^{Nwell} \sqrt{\sum_{i=1}^{Ntime} \left(FWPT_{i,j}^{obs} - FWPT_{i,j}^{cal}\right)^2} \tag{3.11}$$

$$obj3 = \sum_{j=1}^{Nwell} \sqrt{\sum_{i=1}^{Ntime} \left(FGPT_{i,j}^{obs} - FGPT_{i,j}^{cal}\right)^2} \tag{3.12}$$

Here $time$ is the time-lapse period, $Ncell$ is the total number of grid blocks, $Nwell$ is the total number of history matching wells, and $Ntime$ is the total number of timesteps. Figure 3-9 shows the results of the multi-objective function minimization in the global step of the model calibration. The Pareto-based evolutionary algorithm produces a suite of optimal solutions from the diverse initial population around the prior model in a multi-dimensional objective space. In the two-dimensional projection spaces in Figure 3-9, the Pareto-fronts are clearly shown to depict the trade-off between objectives.

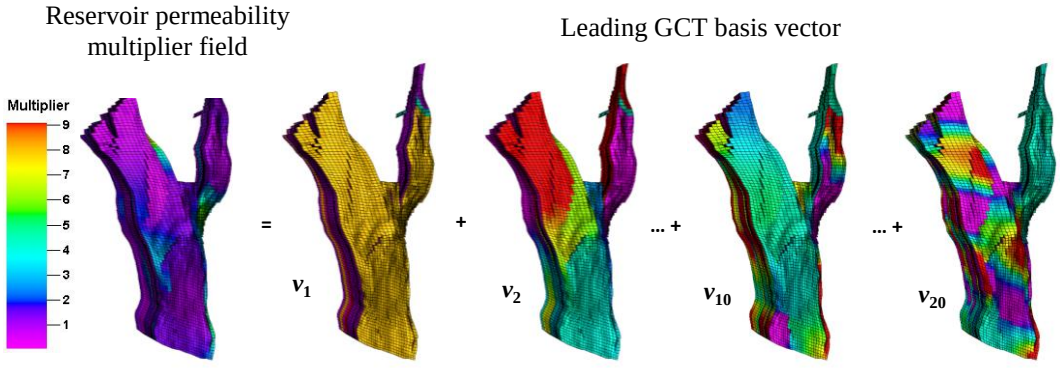

Figure 3-8 Parameterization of the permeability multiplier field as the weighted linear combination of leading GCT basis vectors.

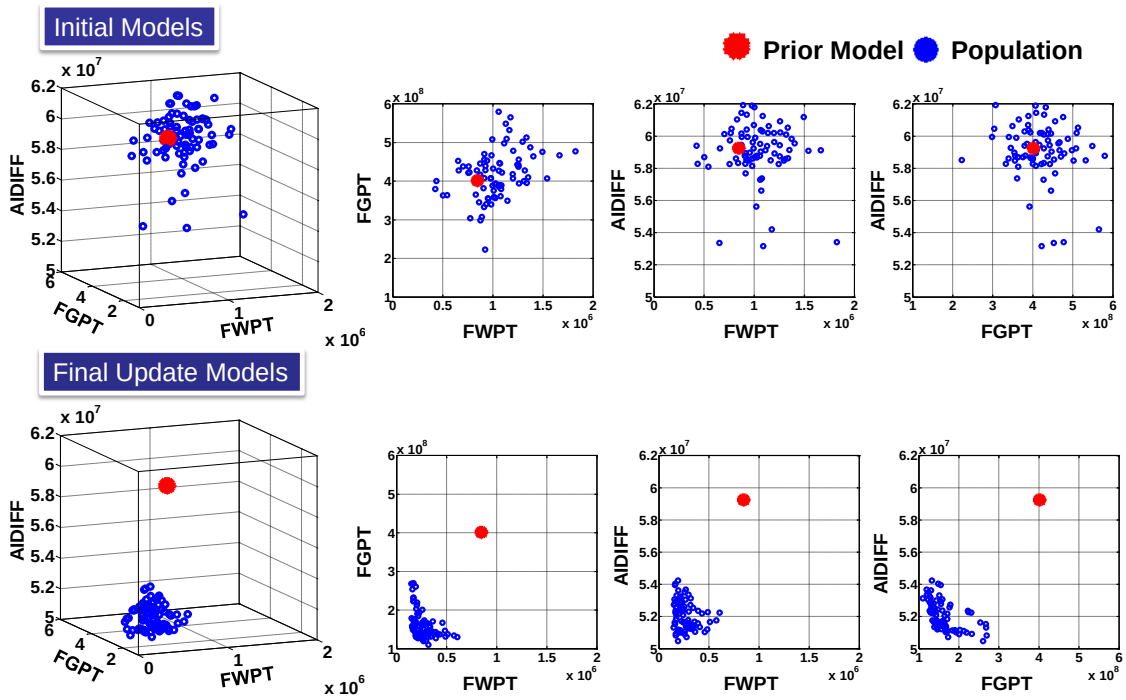

Figure 3-9 Multiobjective function comparisons between initial models and the final models in the global step model calibration.

3.4 Local Update Step: Streamline-based Inversion Workflow

In the local step, the grid block permeability changes are introduced via the streamline-based inversion algorithm. The time-lapse acoustic impedance changes and well by well water cut production data are further integrated, and the fine scale permeability variations between well locations are refined. The sensitivity of the acoustic impedance with respect to grid block permeability considering pressure and saturation effects are derived, and local update results on Norne Field using streamline-based inversion algorithm are shown in the end.

3.4.1 Time of Flight Sensitivity Calculation

We start with the definition of the streamline time of flight, which is the travel time of a neutral tracer along a streamline (Datta-Gupta and King 2007),

$$\tau(\psi) = \int_{\psi} s(\boldsymbol{x}) dr \tag{3.13}$$

Here, ψ is the streamline trajectory, r is distance along the streamline, and s is the slowness, which is the reciprocal of the interstitial velocity:

$$s(\boldsymbol{x}) = \frac{1}{|\vec{v}(\boldsymbol{x})|} \tag{3.14}$$

According to Darcy's law, the slowness is expressed as

$$s(\boldsymbol{x}) = \frac{\phi(\boldsymbol{x})}{\lambda_{rt} * (\boldsymbol{x}) k(\boldsymbol{x}) |\nabla P|} \tag{3.15}$$

Here, λ_{rt} is the total relative mobility, $\lambda_{rt}(\boldsymbol{x}) = \lambda_{ro}(\boldsymbol{x}) + \lambda_{rw}(\boldsymbol{x}) + \lambda_{rg}(\boldsymbol{x})$, and $|\nabla P(\boldsymbol{x})|$ is the pressure gradient along the streamline. The first order variation of the slowness, assuming a fixed pressure gradient, will be given by

$$\delta s(\boldsymbol{x}) = \frac{\partial s(\boldsymbol{x})}{\partial k(\boldsymbol{x})} \delta k(\boldsymbol{x}) + \frac{\partial s(\boldsymbol{x})}{\partial \phi(\boldsymbol{x})} \delta \phi(\boldsymbol{x}) \tag{3.16}$$

From Eq. 3.15, the partial derivatives are

$$\frac{\partial s(\boldsymbol{x})}{\partial k(\boldsymbol{x})} \approx \frac{-\phi(\boldsymbol{x})}{\lambda_{rt}(\boldsymbol{x}) k^2(\boldsymbol{x}) |\nabla P|} = -\frac{s(\boldsymbol{x})}{k(\boldsymbol{x})} \tag{3.17}$$

$$\frac{\partial s(\boldsymbol{x})}{\partial \phi(\boldsymbol{x})} \approx \frac{1}{\lambda_{rt}(\boldsymbol{x}) k(\boldsymbol{x}) |\nabla P|} = \frac{s(\boldsymbol{x})}{\phi(\boldsymbol{x})} \tag{3.18}$$

The approximation in Eq. 3.17 and Eq. 3.18 is that the pressure changes can be negligible for the local perturbations in permeability or porosity. This approximation implies that these small perturbations do not cause streamlines to shift. Then the change in time of flight $\delta\tau$ can be related to the change in slowness by integrating along each streamline trajectory as

$$\delta\tau(\psi) = \int_{\psi} \delta s(\boldsymbol{x}) dr = \int_{\psi} \left[\frac{\partial s(x)}{\partial k(x)} \delta k(\boldsymbol{x}) + \frac{\partial s(x)}{\partial \phi(x)} \delta\phi(\boldsymbol{x})\right] dr \tag{3.19}$$

Thus, by computing the integral from the inlet to the outlet of the streamline within the grid block, the sensitivity of streamline time of flight with respect to permeability and porosity at location $\boldsymbol{x}$ can be expressed as

$$\frac{\delta\tau(\psi)}{\delta k(\boldsymbol{x})} = \int_{\text{inlet}}^{\text{outlet}} \left[-\frac{s(\boldsymbol{x})}{k(\boldsymbol{x})}\right] dr = -\frac{\Delta\tau(\boldsymbol{x})}{k(\boldsymbol{x})} \tag{3.20}$$

$$\frac{\delta\tau(\psi)}{\delta\phi(\boldsymbol{x})} = \int_{\text{inlet}}^{\text{outlet}} \left[\frac{s(\boldsymbol{x})}{\phi(\boldsymbol{x})}\right] dr = \frac{\Delta\tau(\boldsymbol{x})}{\phi(\boldsymbol{x})} \tag{3.21}$$

Here $\Delta\tau(\boldsymbol{x})$ is the time-of-flight across the grid block at location $\boldsymbol{x}$.

3.4.2 Saturation Front Arrival Time Sensitivity

The sensitivities of streamline time of flight with respect to porosity and permeability have been developed. We now relate the time of flight sensitivity to the travel time sensitivity of the water saturation. For two phase flow, this sensitivity is used after water breakthrough at a producing well to calibrate the reservoir properties to water cut response, and can be generalized to three phase flow. According to the Buckley-Leverett equation,

we take the streamline time of flight as the spatial coordinate in the two phase (oil and water) incompressible flow (Datta-Gupta and King 2007),

$$\frac{\partial S_w}{\partial t} + \frac{\partial F_w}{\partial \tau} = 0 \tag{3.22}$$

The solution of Eq. 3.22 is given by

$$\left(\frac{\partial \tau}{\partial t}\right)_{S_w} = \frac{dF_w}{dS_w} \tag{3.23}$$

Eq. 3.23 relates the travel time of a saturation, $t(S_w, \tau; \psi)$ to the time of flight τ, $\frac{\tau}{t} = \frac{dF_w}{dS_w}$. The sensitivity of the saturation arrival time can be computed using that of the streamline time of flight as follows

$$\frac{\delta t(S_w, \tau; \psi)}{\delta k(\boldsymbol{x})} = \frac{\delta \tau(\psi)}{\delta k(\boldsymbol{x})} \Big/ \frac{dF_w}{dS_w} \tag{3.24}$$

$$\frac{\delta t(S_w, \tau; \psi)}{\delta \phi(\boldsymbol{x})} = \frac{\delta \tau(\psi)}{\delta \phi(\boldsymbol{x})} \Big/ \frac{dF_w}{dS_w} \tag{3.25}$$

After water breakthrough on a streamline, these arrival times are evaluated at the total time of flight, $\tau(\psi)$, for the streamline.

3.4.3 Water Saturation Sensitivity Calculation

We now derive expressions for the sensitivity of water saturation with respect to variations in permeability. For two phase flow, water saturation is a function of the streamline time of flight, τ and time, t. First consider self-similar solutions to Eq. 3.22, as have just been derived. Along a streamline the saturation is a function of the dimensionless ratio τ/t. This

allows us to relate the derivative of saturation with respect to time to the derivative with respect to τ as follows:

$$\frac{\partial S_w}{\partial t} = -\frac{\tau}{t^2}\frac{dS_w(\tau/t)}{d(\tau/t)} \tag{3.26}$$

$$\frac{\partial S_w}{\partial \tau} = \frac{1}{t}\frac{dS_w(\tau/t)}{d(\tau/t)} \tag{3.27}$$

Hence:

$$\frac{\partial S_w}{\partial \tau} = -\frac{t}{\tau}\frac{\partial S_w}{\partial t} \tag{3.28}$$

From this we have the water saturation sensitivity:

$$\frac{\delta S_w(\tau,t)}{\delta k(x)} = \frac{\partial S_w}{\partial \tau}\frac{\delta \tau}{\delta k(x)} = -\frac{t}{\tau}\frac{\partial S_w}{\partial t}\frac{\delta \tau}{\delta k(x)} \tag{3.29}$$

The partial derivative of water saturation with respect to time in Eq. 3.28 can be calculated numerically by a backward time difference as

$$\frac{\partial S_w(\tau,t)}{\partial t} \approx \frac{S_w(\tau,t) - S_w(\tau,t-\Delta t)}{\Delta t} \tag{3.30}$$

Here, Δt is the timestep size. This requires saving the saturation information for the time step immediately prior to the time lapse survey time. Therefore, the saturation sensitivity at location τ at a given time t can be calculated by:

$$\frac{\delta S_w(\tau,t)}{\delta k(x)} = -\frac{t}{\tau}\frac{S_w(\tau,t) - S_w(\tau,t-\Delta t)}{\Delta t}\frac{\delta \tau}{\delta k(x)} \tag{3.31}$$

where the last partial derivative of travel time with respect to permeability can be obtained from Eq. 3.20.

3.4.4 Pressure Data Integration

Pressure data integration is performed by converting the spatial distribution of pressure to a spatial distribution of the viscous pressure drop along a streamline from each location, to the producing well where that streamline terminates. Specifically, for a particular location *i,* and pressure P_i then the pressure drop, $\Delta P|_w^i$ along the streamline passing through the location *i* and leading to well *w* with bottom-hole pressure P_w (Figure 3-10) is:

$$P_i = P_w + \Delta P|_w^i \tag{3.32}$$

This utilizes the (known) bottom-hole flowing pressure at the time at which the spatial distribution of pressure data was obtained. If distributed time lapse pressure data and well bottom hole pressure are available, we can compute the pressure drop from Eq. 3.32 and use it as our observation data,

$$\Delta P|_{w,obs}^i = P_{i,obs} - P_{w,obs} \tag{3.33}$$

Now, the data misfit between the simulation response and observation can be written as

$$\begin{aligned} \delta d_i &= \Delta P|_{w,obs}^i - \Delta P|_{w,cal}^i \\ &= \left(P_{i,obs} - P_{w,obs}\right) - \left(P_{i,cal} - P_{w,cal}\right) \\ &= \left(P_{i,obs} - P_{i,cal}\right) - \left(P_{w,obs} - P_{w,cal}\right) \end{aligned} \tag{3.34}$$

The first term is the pressure difference at location *i*, and the second term is the bottom hole pressure difference at well *w*.

3.4.5 Pressure Drop Sensitivity Calculation

The pressure drop along a streamline can be expressed as

$$\Delta P = \int_{\psi} \Delta P(\boldsymbol{x}) dr \tag{3.35}$$

This can be computed by simply summing up the pressure drop across the grid blocks that intersect the streamline as shown in Figure 3-10. Further, we can express the local pressure drop along a streamline using Darcy's law as

$$\Delta P(\boldsymbol{x}) = \frac{q(\boldsymbol{x})\Delta L(\boldsymbol{x})}{A(\boldsymbol{x})\lambda_{rt}k(\boldsymbol{x})} \tag{3.36}$$

where $A(\boldsymbol{x})$ is the cross sectional area, $q(\boldsymbol{x})$ is the flow rate along a streamline, λ_{rt} is the total relative mobility, and $\Delta L(\boldsymbol{x})$ is the arc length of the streamline within the grid block. The pressure drop is a composite quantity involving reservoir properties. We assume that the streamline trajectories, flow rate along streamline, and the total mobility do not change due to small perturbations in permeability. We can now relate the change in local pressure drop to a small change in permeability as

$$\delta\Delta P(\boldsymbol{x}) = \frac{\partial \Delta P(\boldsymbol{x})}{\partial k(\boldsymbol{x})}\delta k(\boldsymbol{x}) \tag{3.37}$$

where the partial derivative is

$$\frac{\partial \Delta P(\boldsymbol{x})}{\partial k(\boldsymbol{x})} \approx \frac{-q(\boldsymbol{x})\Delta L(\boldsymbol{x})}{A(\boldsymbol{x})\lambda_{rt}\big(k(\boldsymbol{x})\big)^2} = -\frac{\Delta P(\boldsymbol{x})}{k(\boldsymbol{x})} \tag{3.38}$$

The pressure drop to a location *i*, $\Delta P|_w^i$ will be given by integration along the streamline trajectory passing through *i* to well *w*,

$$\delta\Delta P|_w^i = \int_\psi \delta\Delta P(\boldsymbol{x})dr = \int_\psi \left[\frac{\partial\Delta P(\boldsymbol{x})}{\partial k(\boldsymbol{x})}\delta k(\boldsymbol{x})\right]dr \tag{3.39}$$

and the pressure drop sensitivity for a particular grid block at location $\boldsymbol{x}$ follows from Eq. 3.39,

$$\frac{\partial\Delta P|_w^i(\psi)}{\partial k(\boldsymbol{x})} = \int_{\text{location}}^{\text{outlet}} \left[-\frac{\Delta P(\boldsymbol{x})}{k(\boldsymbol{x})}\right]dr = -\frac{\Delta P(\boldsymbol{x})}{k(\boldsymbol{x})} \tag{3.40}$$

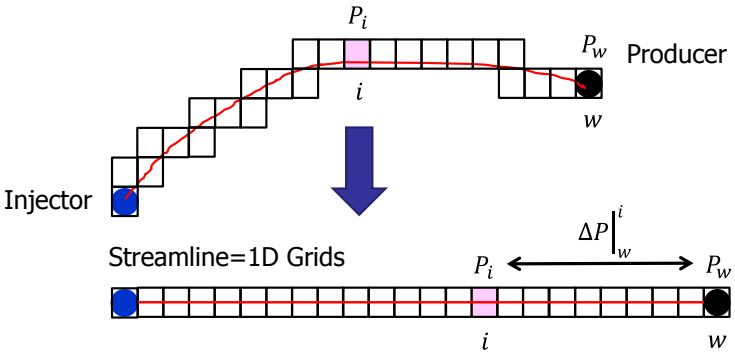

Figure 3-10 A streamline between well pairs connecting grid blocks.

3.4.6 Local Update on the Norne Field

After the global calibration step, we select a few candidate models for the local updates by a cluster analysis in the objective space as shown in Figure 3-9. For the local updates, we need the sensitivity of the acoustic impedance with respect to grid block permeability. This can be obtained via a chain rule,

$$S_{Z_p} = \frac{\delta d_{Z_p}}{\delta k} = \left[\frac{\partial Z_p}{\partial S_w}\frac{\delta S_w}{\delta k} + \frac{\partial Z_p}{\partial S_g}\frac{\delta S_g}{\delta k} + \frac{\partial Z_p}{\partial \mathrm{P}}\frac{\delta \mathrm{P}}{\delta k}\right] \tag{3.41}$$

Here the partial derivatives of acoustic impedance, $\partial Z_p/\partial S_w$, $\partial Z_p/\partial S_g$, and $\partial Z_p/\partial P$ are computed by numerical perturbation from the current saturation and pressure grid block values using Eq. 3.7, while water saturation sensitivity $\partial S_w/\partial k$ is computed by Eq. 3.31.

Notice that we have ignored porosity dependence in Eq. 3.41 and assumed that the changes in porosity because of compaction are not significant. For the gas saturation sensitivity, $\partial S_g/\partial k$, we follow the same derivation as for the water saturation sensitivity in Eq. 3.31. This assumption applies mainly for gas-oil 2 phase system near the top layers of the Norne Field where the free gas cap and oil rim are located. For the pressure sensitivity, we utilize the pressure drop sensitivity given by Eq. 3.40.

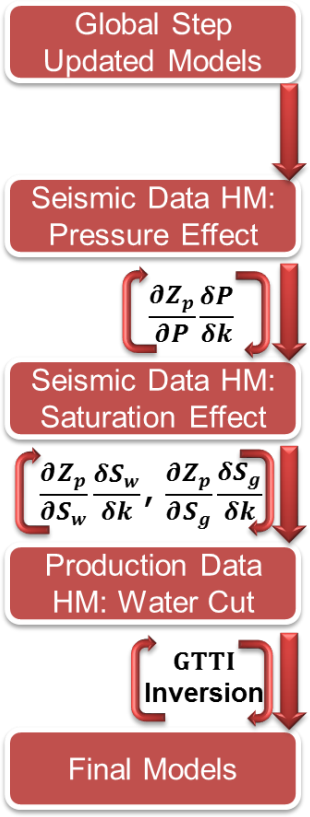

Figure 3-11 Local step streamline-based model calibration workflow.

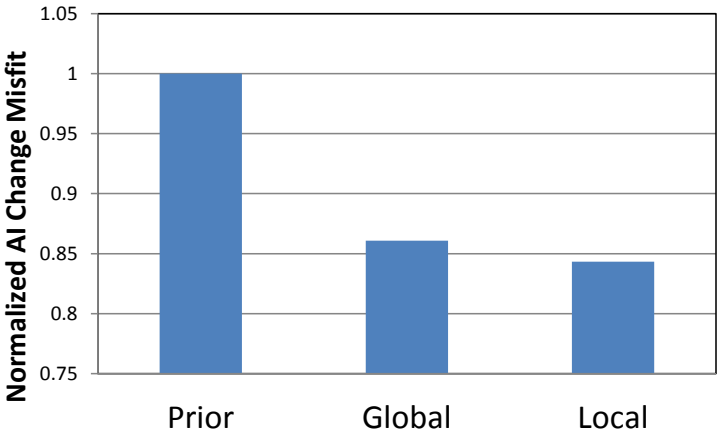

Figure 3-12 The objective function misfit for acoustic impedance change data integration comparisons among the prior model, global step calibrated model, and the final updated model from the local step calibration.

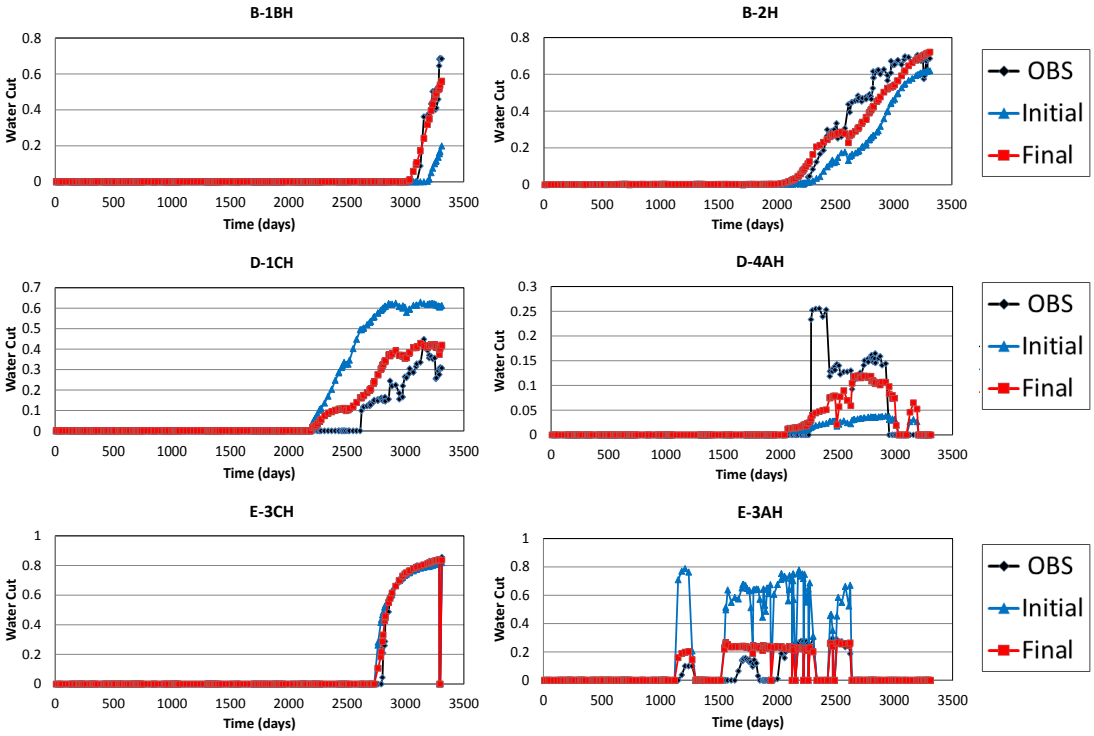

Figure 3-13 Water cut production data history matching comparisons between the initial model and the final updated model.

Our history matching follows a sequential approach (Figure 3-11). To start with, the pressure effects on acoustic impedance changes are integrated to calibrate the model. Next, the saturation effects on the acoustic impedance changes are integrated to update the model. Water saturation sensitivity and gas saturation sensitivity are separately integrated in the inversion process. The inversion performance for acoustic impedance change is shown in Figure 3-12 for one of the models. The majority of the reduction of the acoustic impedance change data misfit was achieved in the global step of the model calibration. Finally, the GTTI (He et al. 2002) is applied to integrate water cut data. The well by well water cut responses are improved as shown in Figure 3-13. The final updated model is shown in Figure 3-14. The final model responses in terms of acoustic impedance changes are compared in Figure 3-15. For the second time-lapse period (2004-2003), a large negative time-lapse acoustic impedance change (red color) misfit in the prior model in the north right part of reservoir (G-segment) was corrected by the inversion. This resulted from an improved matching of the time-lapse pressure change in the final updated model. Overall, the misfit of the time-lapse acoustic impedance change and well production response are improved substantially from the prior model.

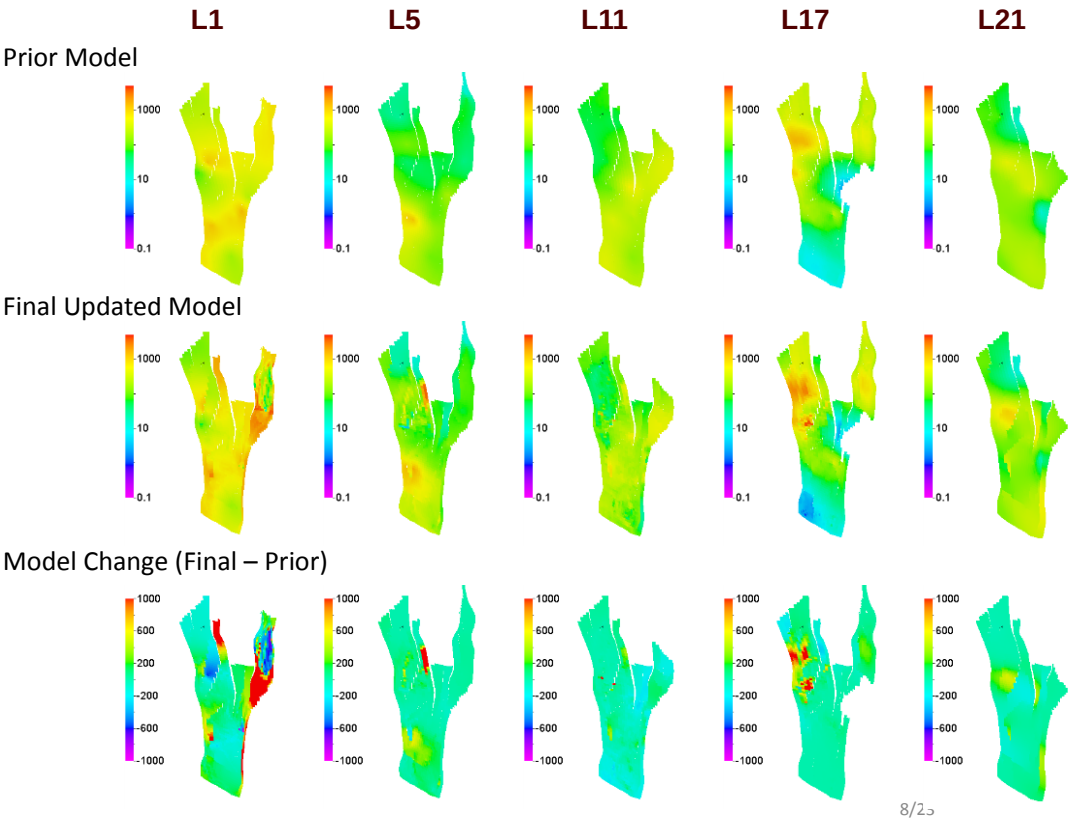

Figure 3-14 Permeability model update comparison by layers: the prior model (Top), the final updated model (middle), and the model changes between the prior and the final models.

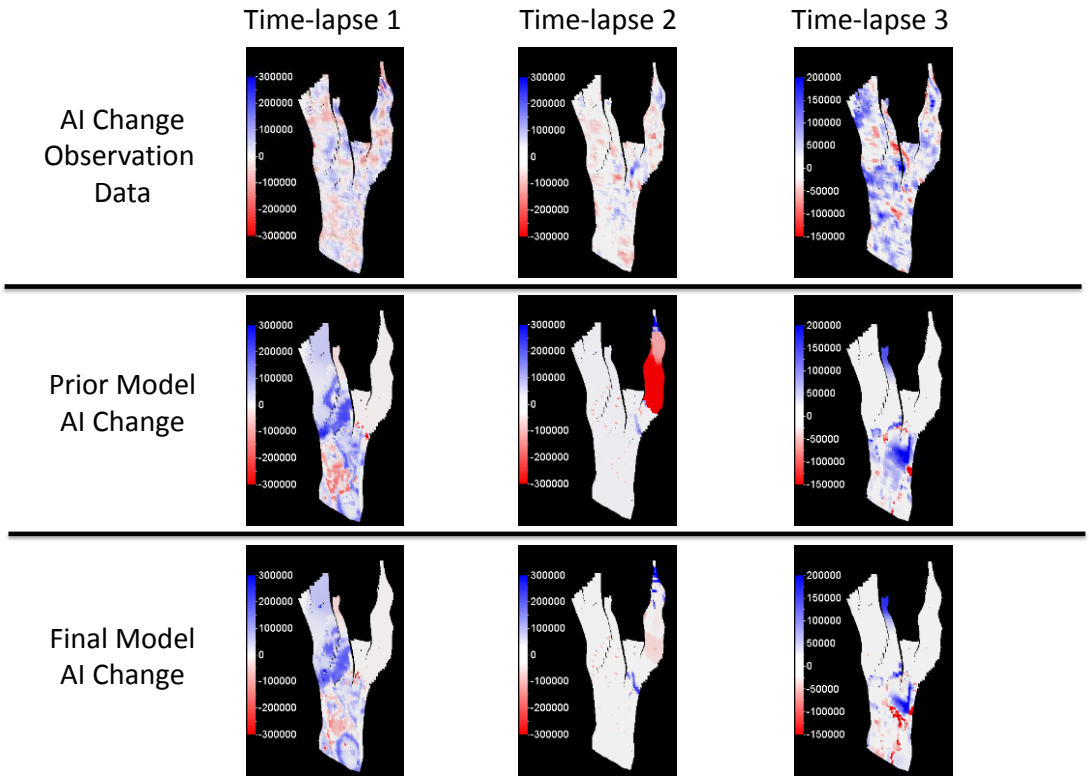

Figure 3-15 Time-lapse acoustic impedance changes comparisons in selected layers among the observation data, the prior model responses, and the final updated model responses.

3.5 Multiobjective Design and Optimization of Polymer Flood Performance

After history matching, the polymer flood optimization is designed based on three selected Norne Field realizations in order to maximize oil production and improve polymer usage efficiency. However, these two objectives are normally conflicting, and then the Pareto-based framework needs to be considered. We first introduce streamline-based rate optimization to allocate production and injection rates in the Norne Field to account for heterogeneity of the reservoirs. Then the optimized production and injection rates are coupled with the Pareto-based polymer optimization to find a trade-off between oil production maximization and polymer usage efficiency improvement.

3.5.1 Streamline-based Rate Optimization

Streamline-based rate optimization is used to allocate production and injection rates for maximizing sweep efficiency while accelerating production/injection before applying polymer optimization. As shown in Eq. 3.42 (Taware et al. 2010), the objective function we need to minimize contains two terms. The first term minimization is for maximizing sweep efficiency by reducing the variance of water arrival time in producers. $t_{i,m}$ is the calculated arrival time of well *i* in group *m*, and $t_{d,m}$ is average arrival time of all the wells in group *m*. The vector **q** includes the production/injection rates and the number of well rates to be optimized (Alhuthali et al. 2007). The second term minimization is for accelerating production/injection by reducing the magnitude of arrival times to avoid delayed water breakthrough because of reducing production and injection rates of the wells too much. The weight η controls the balance between the maximizing sweep efficiency and accelerating production/injection.

$$p(q) = \sum_{m=1}^{N_{group}} \sum_{i=1}^{N_{prod,m}} \left[t_{d,m}(\boldsymbol{q}) - t_{i,m}(\boldsymbol{q})\right]^2 + \eta \sum_{m=1}^{N_{group}} \sum_{i=1}^{N_{prod,m}} \left[t_{i,m}(\boldsymbol{q})\right]^2 \quad (3.42)$$

The arrival time t is defined as the travel time from waterfront current position to the producer. For calculation purpose, we take the time of flight of the top 20% (user defined parameter) fast streamlines as the average arrival time. As shown in Eq. 3.43, $N_{fsl,i}$ represents the number of fast streamlines connected to the producer *i* in group *m*, and $\tau_{l,i}$ represents the time of flight of streamline *l* connected to the producer *i* in group *m*. The streamline time of flight equation is defined in Eq. 3.13. $t_{d,m}$, the average arrival time of

all the wells in group *m*, is an arithmetic average of the calculated arrival time of all the wells in group *m* (Eq. 3.44),

$$t_{i,m}(\boldsymbol{q}) = \frac{1}{N_{fsl,i}} \sum_{l=1}^{N_{fsl,i}} \tau_{l,i,}(\boldsymbol{q}) \tag{3.43}$$

$$t_{d,m}(\boldsymbol{q}) = \frac{1}{N_{prod,m}} \sum_{i=1}^{N_{prod,m}} t_{i,m}(\boldsymbol{q}) \tag{3.44}$$

The objective function Eq. 3.42 is minimized using streamline-based analytic sensitivities and a Sequential Quadratic Programming (SQP) technique (Alhuthali et al. 2007).

3.5.2 Polymer Flood Mechanism and Performance Measures

Polymer Flood Mechanism

Polymer injection during water flooding can effectively reduce viscous fingering and increase sweep efficiency by decreasing the mobility of the injected water, which results from increase of water viscosity and reduction of rock permeability to water. The ECLIPSE reservoir simulation software is used to model polymer property and simulate polymer flooding (Schlumberger 2012).

The increase of the polymer concentration drives up the water viscosity, leading to mobility decrease of the injected water. As shown in Eq. 3.45, the partially mixed water viscosity is the multiplication between the viscosity of a fully mixed polymer solution ($\mu_m(C_p)$) and water viscosity (μ_w). ω is the Todd-Longstaff mixing parameter, describing

the degree of segregation between the water and polymer solution in the range of 0 to 1. $\mu_m(C_p)$, an increasing function of the polymer concentration in solution (C_p), should be input as a table format, and then the calculated $\mu_{w,e}$ is used to obtain the effective water viscosity, which is fed into the polymer flood simulation model (Schlumberger 2012).

$$\mu_{w,e} = \mu_m(C_p)^{\omega} * {\mu_w}^{1-\omega} \tag{3.45}$$

The increase of the polymer concentration also drives up the amount of adsorbed polymer by the rock. The polymer adsorption, which is considered as an instantaneous effect in the model, results in a reduction in the permeability of the rock to the aqueous phase. In the polymer flood simulation, the permeability reduction factor (R_k) is proportional to the amount of adsorbed polymer in the rock formation shown by Eq. 3.46 (Schlumberger 2012). C_p^{amax} denotes the maximum absorbed concentration, and C_p^a represents absorbed polymer concentration in the rock. When the adsorbed polymer reaches the maximum, R_k is equal to RRF, which is the residual resistance factor.

$$R_k = 1.0 + (RRF - 1.0)\frac{C_p^a}{C_p^{amax}} \tag{3.46}$$

Performance Measures

To consider economics of polymer flooding, the optimal slug size and polymer concentration are selected as control variables, and they are important factors for successful operation (Al-Sofi and Blunt 2011). There are two conventional measurements to evaluate polymer flood performance. One is incremental oil production (ΔN_p), which is the difference between cumulative oil production with and without polymer (Eq. 3.47).

The other measurement is polymer utility factor (UF), which is the ratio between total injected polymer and incremental oil production (Eq. 3.48). UF describes the polymer injection efficiency.

$$\Delta N_p = N_p(with\ polymer\ ) - N_p(without\ polymer\ ) \tag{3.47}$$

$$UF = \frac{Total\ injected\ polymer}{\Delta N_p} \tag{3.48}$$

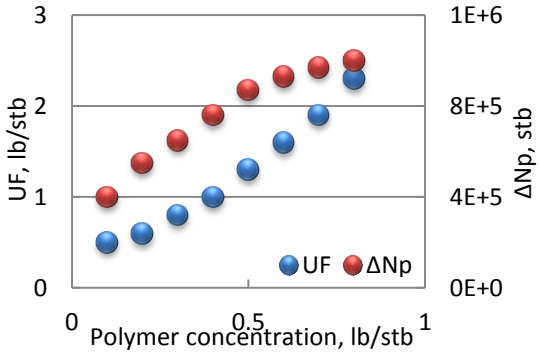

(a) Sensitivity analysis of ΔN_p and UF on polymer concentration

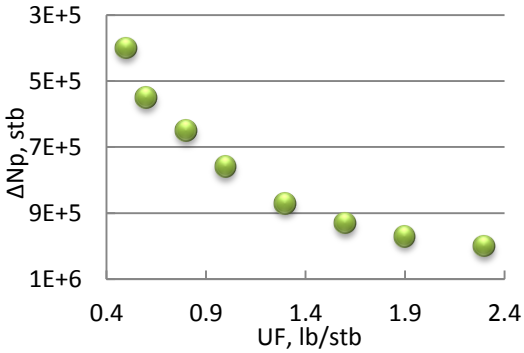

(b) Trade-off between ΔN_p and UF (polymer concentration sensitivity)

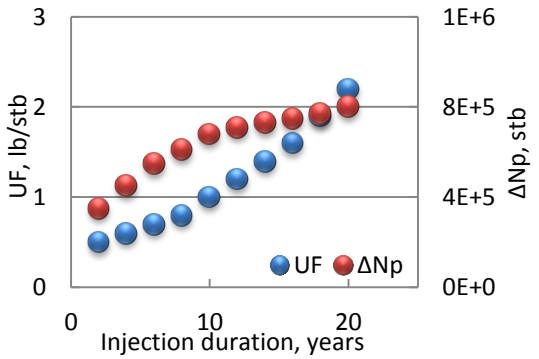

(c) Sensitivity analysis of ΔN_p and UF on slug size

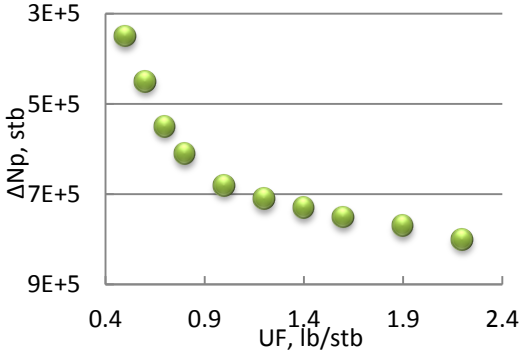

(d) Trade-off between ΔN_p and UF (slug size sensitivity)

Figure 3-16 ΔN_p and UF conflicting feature analysis.

Unfortunately, large oil production improvement always comes with poor polymer usage efficiency. As shown in Figure 3-16 (a), sensitivity analysis of ΔN_p and UF is conducted on polymer concentration. With increase of polymer concentration, ΔN_p increases, and polymer performance become worse. After projecting solution into objective space, Figure 3-16 (b) shows the conflicting feature clearly between ΔN_p and UF. The slug size sensitivity analysis comes to the same conclusion (Figure 3-16 (c) and Figure 3-16 (d)). Because of the conflicting features of these two objectives, the multiobjective Pareto-based optimization framework is employed in the polymer flood optimization. Thus, our optimal strategy is that we want to find optimal combination of polymer concentration and slug size to increase ΔN_p while maintaining high polymer usage efficiency.

3.5.3 Pareto-based Polymer Optimization

To consider ΔN_p and UF these two conflicting objectives, the Pareto-based framework is utilized again in the optimization stage, and the workflow (Figure 3-17) is similar with that in the global history matching stage. First, the polymer concentration and slug size are initialized using Latin hypercube sampling. Next, all the models with difference combination of polymer concentration and slug size are fed into forward reservoir simulation running. Further, the Pareto-based model ranking are implemented based on the simulation results in the objective space (ΔN_p and UF). Then highly ranked models are selected to be utilized by genetic operations: crossover and mutation. After several generations, the optimal solution is chosen from the Pareto front of the last generation.

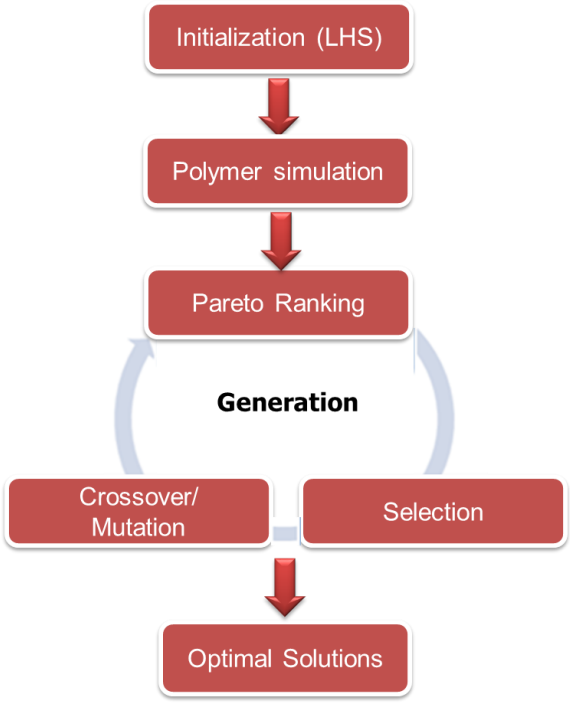

Figure 3-17 Pareto-based polymer optimization workflow.

The workflow is illustrated using the mathematical minimization problem. We want to minimize f_1 and f_2 simultaneously and find an optimal solution for these two objectives (Eq. 3.49). By applying the Pareto-based optimization workflow, Figure 3-18 shows Pareto front movement with the increase of generation. In the 1st generation, there are many uncompetitive solutions in the objective space. Those uncompetitive solutions becomes less in the 3rd generation, and they all convert to Pareto optimal solutions in the 7th generation. Pareto optimal solutions on the trade-off curve include (0,0) point, which optimizes f_1 only, and (5,5) point, which optimizes f_2 only. Mathematically, it is difficult to make the decision that which solution is better than the other. However, in practice, we need to pick up an optimal solution to consider the trade-off between these two conflicting

objectives. Here, mean square error (MSE) algorithm is adopted to choose the optimal solution (Talbert et al. 2008).

$$f_1(x) = x_1^2 + x_2^2$$
$$f_2(x) = (x_1 - 5)^2 + (x_2 - 5)^2 \quad (3.49)$$

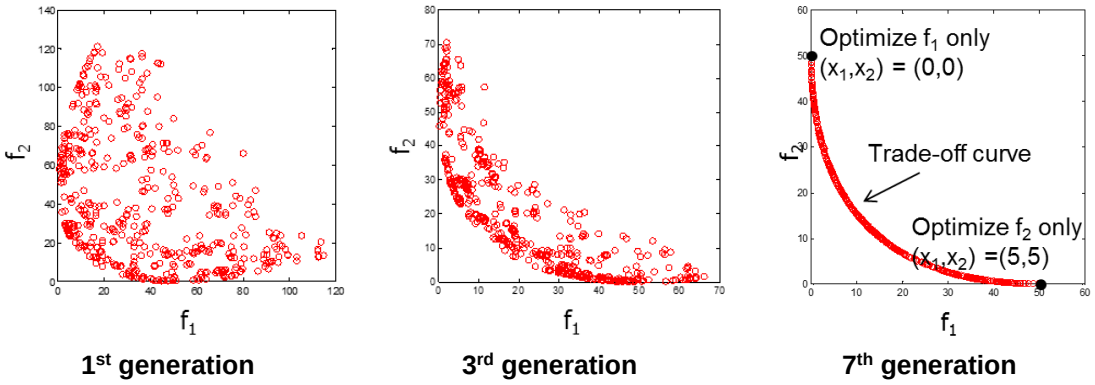

Figure 3-18 Pareto-based optimization workflow illustration.

MSE aims to search the solution with the smallest square error, which is the compromised solution between the two objectives. First, final trade-off curve between ΔN_p and UF is obtained (Figure 3-19 (b)), and the data is sorted from minimum to maximum with respect to UF (or ΔN_p). For each point on the curve, draw regression line for both left and right sides, and calculate sum square error for both sides. Thus, each point has one square error, and the square errors of all the points are plot with respect to UF (or ΔN_p) (Figure 3-19 (a)). Finally, select the point with the minimal square error (red point in Figure 3-19 (a)), which is the optimal point on the trade-off curve (red point in Figure 3-19 (b)).

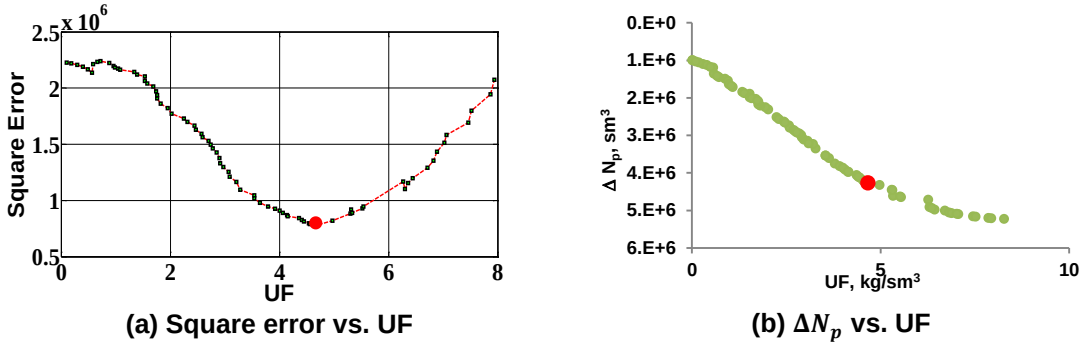

(a) Square error vs. UF

(b) ΔN_p vs. UF

Figure 3-19 MSE algorithm for trade-off optimal point selection.

3.5.4 Two-Step Polymer Flood Optimization Workflow

All the information are summarized in the two-step polymer flood optimization workflow (Figure 3-20). Streamline-based rate optimization is used to modify production/injection rates to capture reservoir heterogeneity, and the Pareto-based polymer optimization is applied to get an optimal combination of polymer concentration and slug size to generate an optimal trade-off between ΔN_p and UF. The explanation for this two-step worflow is as follows:

(a) Run reservoir forward simulation and trace streamline.

(b) Compute analytical sensitivity and use SQP to minimize the objective for maximizing sweep efficiency while accelerating production/injection.

(c) The optimized production/injection rates are fed into polymer optimization step.

(d) LHS is utilized to initialize polymer concentration and slug size values.

(e) The multiobjective genetic algorithm is implemented to get Pareto front trade-off.

(f) Pick the optimal compromised solution from trade-off curve using MSE algorithm.

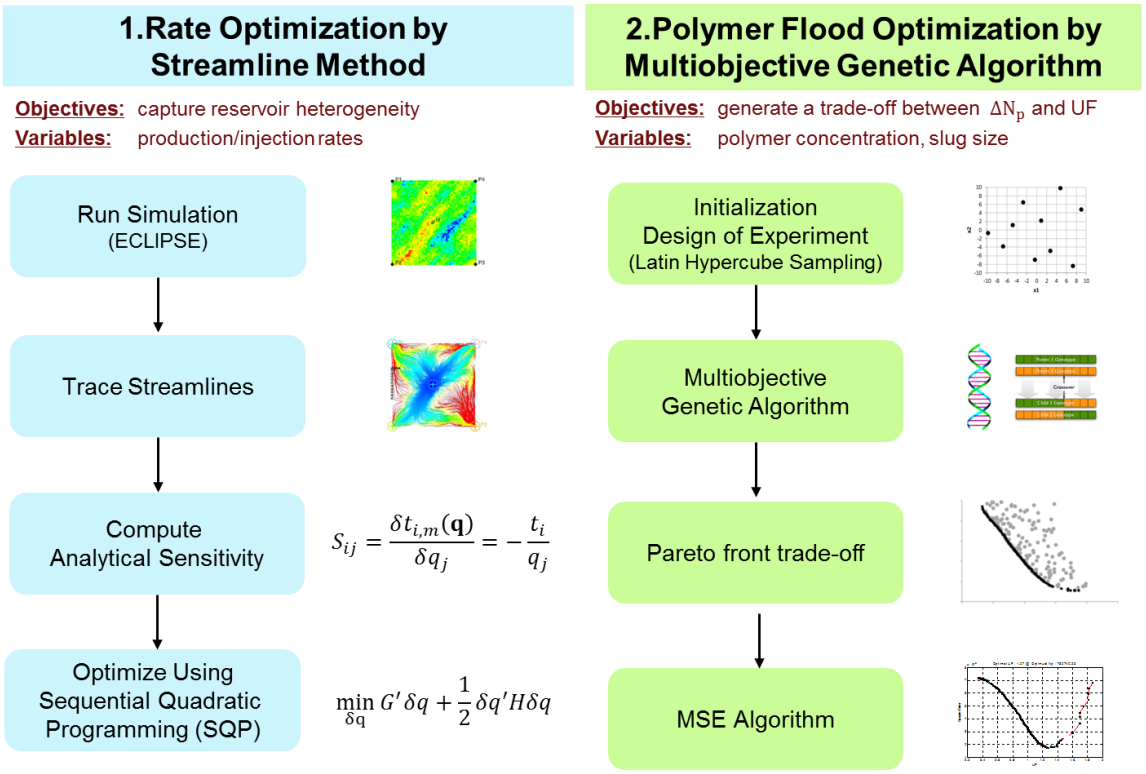

Figure 3-20 Two-step polymer flood optimization workflow.

3.5.5 Norne Field Polymer Flood Optimization

Here, we apply the two-step polymer flood optimization workflow to the Norne Full Field. We have got three history matched realizations under the Global-Local hierarchical history matching workflow in section 3.2 and 3.3. Figure 3-21 shows the first realization history matched model for gas, oil and water saturation. From the property distribution, it is clear to see that gas is on the top, oil locates in the middle and water is at the bottom.

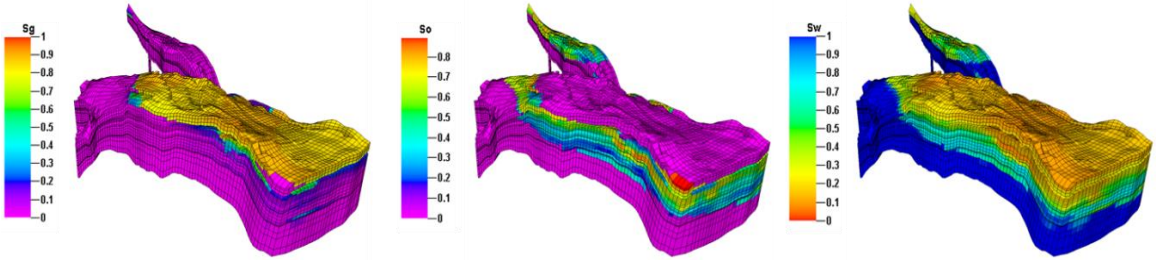

(a) Gas saturation model **(b) Oil saturation model** **(c) Water saturation model**

Figure 3-21 1st realization history matched models.

Well Configuration

Figure 3-22 (a) shows the well schedules at the end of history matching period (Dec. 01, 2006). There are only five injectors: two water injectors and three gas injectors. If we keep the original schedule, F-1H and F-2H are the only two choices to inject polymer and the Norne Field cannot be swept efficiently by polymer. That's why we develop the new well schedules as follows (Figure 3-22 (b)):

(a) Reopen eight wells (C-4H, D-1H, D-4H, F-3H, B-4BH, B-1H, B-4H, and C-2H) and close three wells (B-4DH, E-1H, and E-2AH). Injectors are around the boundary of Norne Field in order to control the whole field area and increase sweep efficiency.

(b) Turn injectors C-1H and C-2H to producers and turn producers D-4H and D-1H to injectors.

(c) Keep C-4AH injecting gas, F-1H and F-2H injecting water, and the rest five injectors injecting water and polymer.

The new schedule is adjusted based on well location, well perforation, and oil saturation distribution, etc. For example, the reason why F-1H and F-2H do not inject

polymer is that these two wells locate near the edge water (Figure 3-23 (a)). If we inject polymer, polymer will be mixed in edge water largely, and the portion which displace oil become less. Hence, it may become unfavorable for oil sweep efficiency and NPV calculation. Also, well location and oil saturation distribution are another reasons to make producer-injector transformation. Figure 3-23(b) shows that two well groups are clearly formed after producers D-4H and D-1H are turned to the injectors. D-4H and D-1H locate in the middle of their respective well groups, which help injected polymer of D-4H and D-1H evenly distribute in the reservoir. It is beneficial for the uniform water front arrival from injectors to producers, and then rate optimization algorithm can converge faster.

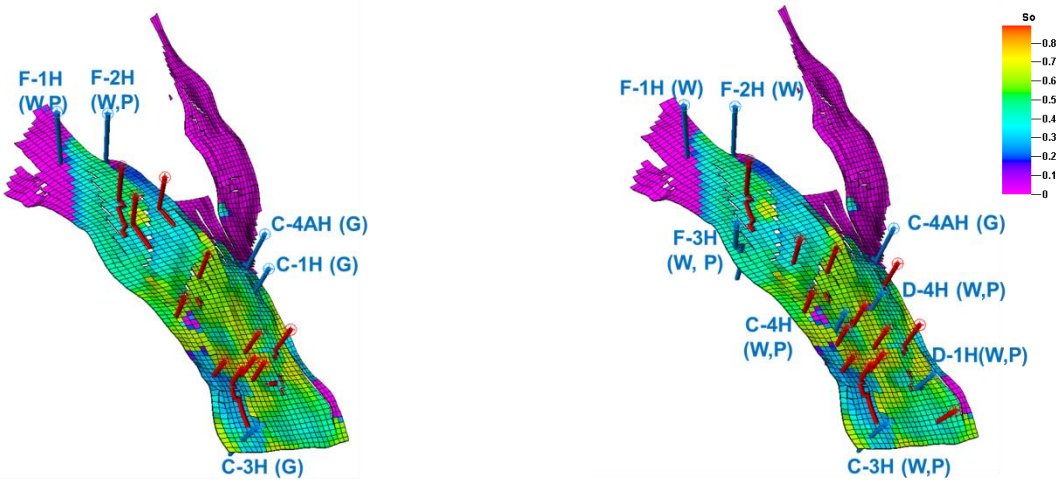

(a) Original Schedule **(b) New Schedule**

Figure 3-22 Comparison between original and new schedules (layer 6 oil saturation map of the 1st realization).

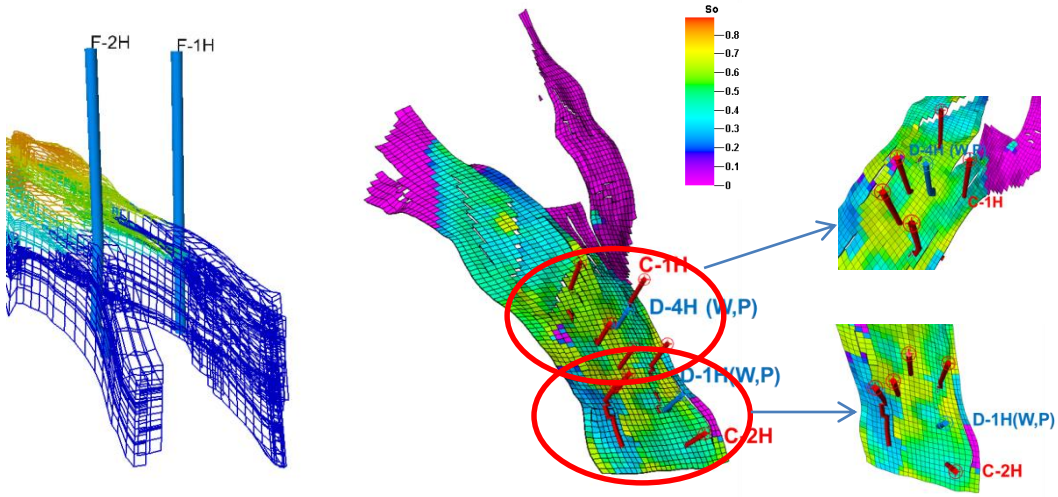

(a) F-1H & F-2H well location. **(b) D-4H&D-1H well groups.**

Figure 3-23 New schedule illustration.

Rate Optimization

Based on the new schedule, the Norne Field injection and production rates are optimized by the streamline-based method to capture reservoir heterogeneity under the production constraints (Table 3.4). The rate of selected injectors and producers are shown in Figure 3-24. With the help of the optimized injection and production rates, it is much easier for polymer to reduce viscous fingering.

Rate optimization performance can be measured by ΔN_p and NPV. Figure 3-25 compare these two measurements in two cases: (I) the base case using injection and production rates without optimization; (II) the new case with optimized rates before polymer optimization. Economic parameters in Table 3.5 are applied in NVP calculation. It is clearly to see that rate optimization can help improve ΔN_p and NPV significantly.

Table 3.4 Rate optimization production constraints	
Parameters	Input Values
Max. Inj. BHP, [Bar]	450
Min. Prod BHP, [Bar]	150
Max. Water Inj. Rate, [sm^3/day]	12,000
Max. Liquid Prod Rate, [sm^3/day]	6,000
Max. Water Cut, [%]	95

Table 3.5 Polymer flooding optimization economic parameters	
Parameters	Input Values
Discount Rate, [%]	10
Oil Price, [$/bbl]	80
Water Inj./Prod. Cost, [[$/bbl]	6
Gas Inj. Cost, [$/Mscf]	1.2
Polymer Inj/Prod Cost, [$/lb]	10

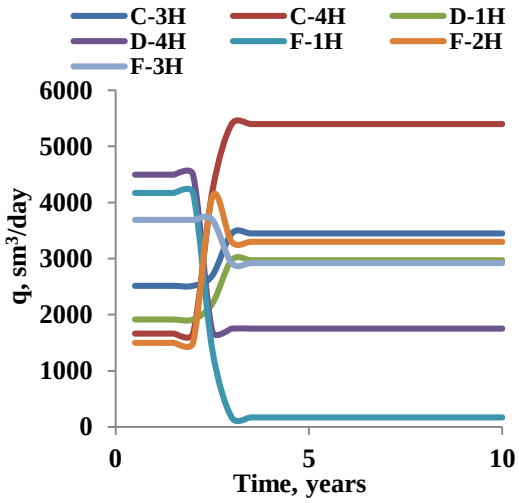

(a) Optimized rates of selected injectors

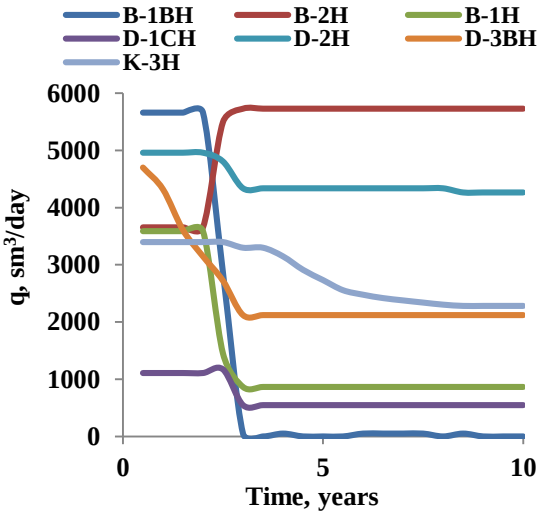

(b) Optimized rates of selected producers

Figure 3-24 Optimized injection and production rates.

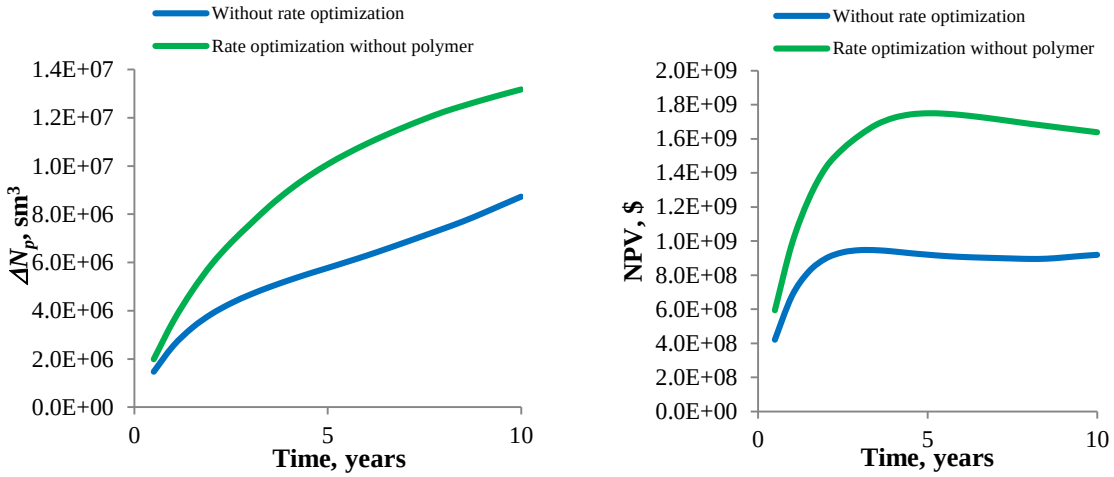

(a) ΔN_p VS Time **(b) NPV Vs Time**

Figure 3-25 Plots comparing base case without rate optimization and new case with rate optimization.

Polymer Optimization

After rate optimization, it is followed by polymer optimization. Polymer concentration ranges between 0 and 1 kg/sm^3, and slug size ranges between 1 and 10 years. To address geologic uncertainty and find an approach to pick an optimal solution from multiple realizations, the average objectives are calculated from three realization objectives (Eq. 3.50 and Eq. 3.51), and then the average Pareto front is generated where we pick the optimal point. In Figure 3-26, red, blue, and purple lines are optimal Pareto fronts of three realizations, and green line, which locates among the three lines, is the average Pareto front between ΔN_p and UF. The average Pareto front avoids extreme pessimistic or optimistic realizations and becomes a good representative to capture geologic uncertainty.

The red point, the comprised optimal solution between production improvement and polymer efficiency, is picked by MSE algorithm from the average Pareto front.

$$\Delta N_{p_{avg}} = \sum_{i=1}^{N_{realization}} \Delta N_{p_i} \tag{3.50}$$

$$UF_{avg} = \sum_{i=1}^{N_{realization}} UF_i \tag{3.51}$$

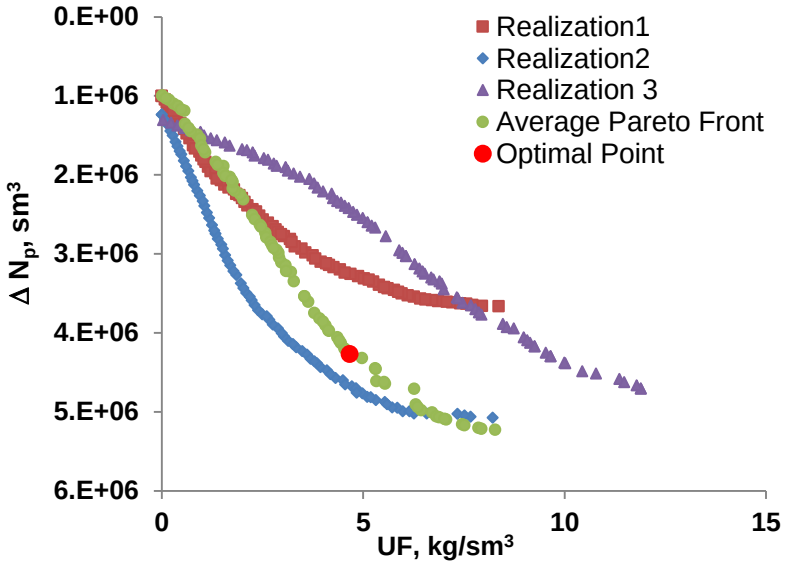

Figure 3-26 Three realizations Pareto front and average Pareto front.

Figure 3-27 shows the ΔNp and NPV performance among three cases. (I) the base case using injection and production rates without the rate optimization (blue line); (II) the case using optimized rates without the polymer optimization (green line); (III) the case using optimized rates with the polymer optimization (red line). We can see that the rate optimization and polymer optimization improves ΔN_p and NPV sequentially. This

optimization workflow considers two objectives concurrently and gives a balanced candidate, which results in higher oil production increment and profit. In Figure 3-27 (b), there is a turning point, which is around 3 years. Before the turning point, the green line is a little higher than the red line, while after the turning point, the red line outperforms the green line. That's because the polymer should need a period of time to take effect before forming favorable water front, and even play a negative role in the reservoir dynamic flow behavior at the beginning.

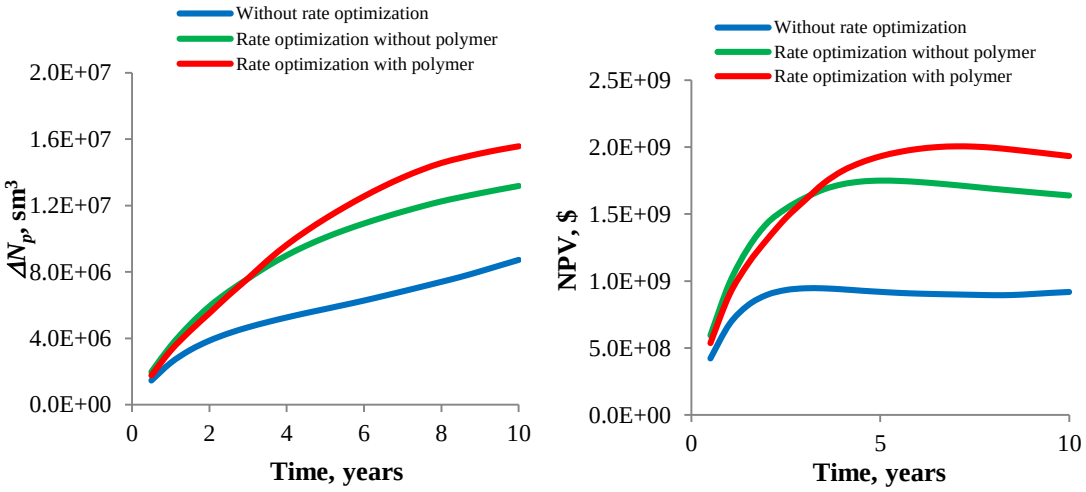

(a) ΔN_p VS Time **(b) NPV Vs Time**

Figure 3-27 Plots comparing polymer optimization, rate optimization without polymer and base case.

3.6 Summary

In this chapter, we have presented the Norne Field history matching using a global-local history matching workflow, and then applied a two-step polymer flood optimization workflow including the streamline-based rate optimization and the Pareto-based polymer

optimization on the Norne Field production optimization. The main findings are summarized as follows:

1. The Norne Field application demonstrates the practical feasibility of the multiobjective Pareto-based framework in the history matching and production optimization.
2. The hierarchical history matching workflow consisting of global and local updates can be successfully applied to Norne Field. This approach is particularly well-suited for the calibration of the reservoir properties of high-resolution geologic models. Through the global and fine scale updates, the acoustic impedance changes and well by well water cut data matching are improved substantially.
3. The Pareto-based approach integrates production and seismic conflicting objectives simultaneously and discovers trade-off between them, accounting for the influence of each objective in the global history matching update.
4. The streamline-based inversion workflow can reduce data misfit further through integration with seismic (pressure and saturation effects) and production data (water-cut) sequentially in the local updates.
5. The coupling of rate optimization and multi-objective genetic algorithm provides an effective approach for the optimization of slug size and polymer concentration in the Norne Field. The selected optimal solution from the average Pareto front of three realizations provides a compromise for ΔN_p and UF. The rate optimization and polymer optimization improves ΔN_p and NPV sequentially and significantly.

6. The rate optimization allocates production and injection rates for maximizing sweep efficiency and accelerating production/injection. The optimized production and injection rates can help to improve the role of polymer in reducing viscous fingering in the polymer optimization.
7. The multi-objective genetic algorithm generates a set of optimal solutions, which represent a compromise for maximizing oil production while maintaining low polymer utility factor. The average Pareto front from three realizations captures geologic uncertainty and avoids extreme pessimistic or optimistic results.

CHAPTER IV

A COMPARATIVE ANALYSIS OF REPARAMETERIZATION METHODS FOR HISTORY MATCHING CHANNELIZED RESERVOIRS

In this chapter, a novel two-step history matching workflow is proposed where the channel geometry is modeled using the level sets, and the internal heterogeneity within the channel facies is modeled using the parameterization with linear basis functions, specifically the Grid Connectivity Transform (GCT) basis. Facies boundaries are represented by the level set function where seismic information is incorporated, and the boundaries are gradually moved by solving the level set equation under the seismic constraint. For history matching, the Markov Chain Monte Carlo (MCMC) method is employed to minimize production data misfit by adjusting channel geometry and also channel petrophysics by perturbing the GCT coefficients. Moreover, seismic constraint, for the first time, is incorporated into the level set method to improve the facies calibration performance.

4.1 Introduction

Identification of the channel geometry, facies boundaries and characterization of channel petrophysical properties are critical for performance prediction of channelized reservoirs. The sharp contrast between facies, the orientation and geometry of channels with high permeability contribute most to the fluid flow, followed by the heterogeneity within the channel. Thus, it is important to efficiently update channel geometry as well as channel petrophysics during history matching.

There are many difficulties for traditional geostatistical techniques, such as the two-point geostatistical method, the object-based modeling approach, and the multi-point geostatistical method, to calibrate channelized reservoirs. The two-point geostatistical method is inappropriate for the channel geometry reproduction because a variogram cannot represent spatial continuity at more than two locations simultaneously (Koltermann and Gorelick 1996). Although the object-based method (Deutsch and Wang 1996) has been widely used in generating channelized facies distributions, it is difficult and time-consuming to incorporate into history matching to honor dynamic data. The multi-point geostatistical (Strebelle and Journel 2001) method, overcoming the downsides of the two-point and object-based methods, heavily relies on the quality of the training image, which possesses too many uncertainties.

Parameterization methods have been successfully applied in the image reconstruction (Bhark et al. 2011; Jafarpour 2011; Jafarpour et al. 2009b) and the inverse problem (Awotunde and Horne 2010; Jafarpour et al. 2009a; Kang et al. 2014) by reducing parameter dimensionality. Especially in the history matching of channelized reservoirs, Parameterization may mitigate the issues brought by geostatistical approach in term of keeping the large-scale channel continuity while honoring dynamic data. The Discrete Cosine Transform (DCT) uses a small number of coefficients to capture dominant features of reservoir permeability distributions and helps capture spatial continuity of geological facies in channelized environments during history matching (Jafarpour and McLaughlin 2009). Currently, the main limitation of the DCT is that it can only be used in spatial domains with regular spatial structure. In contrast, the GCT can be extended from structure

grids to unstructured grids (Bhark et al. 2011b; Bhark et al. 2012). The Discrete Wavelet Transform (DWT) is another attractive approach for the history matching of channelized reservoirs on account of its ability of capturing both frequency and location information. Jafarpour (2011) calculated the sensitivity of flow response with respect to important wavelet coefficients and used the Ensemble Kalman Filter (EnKF) to update this subset of wavelet coefficients to approximate the spatial distribution of permeability. The DWT is also powerful in the integration of different sources of data. For the integration, production and variogram information can be integrated sequentially into the reservoir model by calculating a sensitivity matrix of production response to wavelet coefficients (Kind and Quinteros 2007; Sahni and Horne 2005, 2006a, 2006b). However, the difficulties in location and estimation of significant DWT coefficients become the bottleneck to improve the DWT performance in the inverse problem.

The level set method, as a numerical algorithm for surface and shape tracking (Osher and Fedkiw 2002; Osher and Sethian 1988; Osher and Santosa 2001), has shown great promise to effectively parameterize facies boundaries and allows for changing channel geometry and connectivity during history matching. Xie et al. (2011) applied the two-stage MCMC to perturb the coefficients of velocity eigenvectors, followed by the channel boundaries evolution through solving the level set equation. Ping and Zhang (2014) parameterized channelized reservoirs into a group of parameters: level set function, real radius and virtual radius, which are updated by the EnKF. These approaches simply assumed constant properties within each facies, ignoring the heterogeneity of the reservoir field. In that line, Agbalaka and Oliver (2011) and Lorentzen et al. (2012) used the EnKF,

combined with the level set method, to jointly update facies boundaries and estimate petrophysical properties within each facies. The approaches listed above mainly focus on conditioning models to well data but seismic constraint in the level set has not been mentioned in the current literature. The successful integration of seismic constraint can help to not only significantly improve channelized reservoir history matching performance, but also extend the level set from simple channelized models to more complicated ones.

Here, we propose a history matching workflow for conditioning the calibrated realizations to the production data, facies observation at the wells, and seismic constraint. The proposed approach is applied to a 2D example. First, we examine the effectiveness of the level set approach by comparison with other approaches for channelized reservoirs: for example, the DCT, GCT, and DWT. The level set approach is shown to significantly outperform in terms of reproducing channel geometry. Second, we show that the use of seismic constraint helps preserve the structure of facies distribution and geologic realism during history matching. Finally, the calibrated facies models are further updated by adjusting the internal channel permeability distribution to fine-tune the history matching. The GCT method is selected to carry out heterogeneity characterization, since it has been successfully applied in the field-scale history matching (Watanabe et al. 2013). In this sense, the GCT integration in the model characterization can help enhance the applicability and stability of the level set in the field-scale application.

4.2 Traditional Parameterization Methods for Channelized Reservoirs

Traditional parameterization methods, such as the DCT, GCT, and DWT, show great promise to effectively parameterize property model in the non-channel system. However, direct application of these methods on the channelized reservoirs is questionable. In this section, we first discuss the DCT and DWT methodologies. Then the DCT, GCT, and DWT are compared in the image reconstruction and history matching performances to have an understanding for these three methods before introducing the level set method.

4.2.1 Discrete Cosine Transform Method

The Discrete Cosine Transform is a Fourier-based transform widely used for data compression (Gonzalez and Woods 2002). For a 2-D reservoir model including $N_x \times N_y$ grids, $u(x,y)$ is the property parameter needed to be estimated. The forward equation of the DCT is written as (Gonzalez and Woods 2002):

$$v(r,s) = \alpha(r)\alpha(s) \sum_{x=0}^{N_x-1} \sum_{y=0}^{N_y-1} u(x,y) \cos\left[\frac{(2x+1)r\pi)}{2N_x}\right] \cos\left[\frac{(2y+1)s\pi)}{2N_y}\right] \quad (4.1)$$

where $r = 0, 1, 2, \ldots, N_x - 1$ and $\alpha(r=0) = \sqrt{\frac{1}{N_x}}$ and $\alpha(r \neq 0) = \sqrt{\frac{2}{N_x}}$. N_y and $\alpha(s)$ take the same expression. $v(r,s)$ is the DCT coefficient and the product of cosine functions is the DCT basis. Eq. 4.1 can be rewritten as matrix-vector form:

$$\mathbf{v} = \mathbf{\Phi}^{\mathbf{T}}\mathbf{u} \quad (4.2)$$

where $\mathbf{v}$ and $\mathbf{u}$ are in the vectors form of the DCT coefficients and property parameter set respectively, and $\mathbf{\Phi}$ is the matrix form of the DCT basis. Figure 4-1 shows the DCT basis

in an 8×8 grids reservoir. The basis images are arranged based on orientation and frequency in a descending order from upper left to lower right (Bhark et al. 2011a; Jafarpour and McLaughlin 2009).

The linear combination of the DCT basis and coefficient can help us reconstruct the original property model and carry out history matching based on Eq. 4.3, which is the inverse equation of the DCT.

$$\mathbf{u} = \Phi \mathbf{v} \tag{4.3}$$

Although the DCT has strong image compression and is suited for dimension reduction in history matching, the main problem for the DCT is that it is limited to spatial domains with regular spatial structure. In contrast, the GCT can be extended from structured grids to unstructured grids (Bhark et al. 2011b; Bhark et al. 2012).

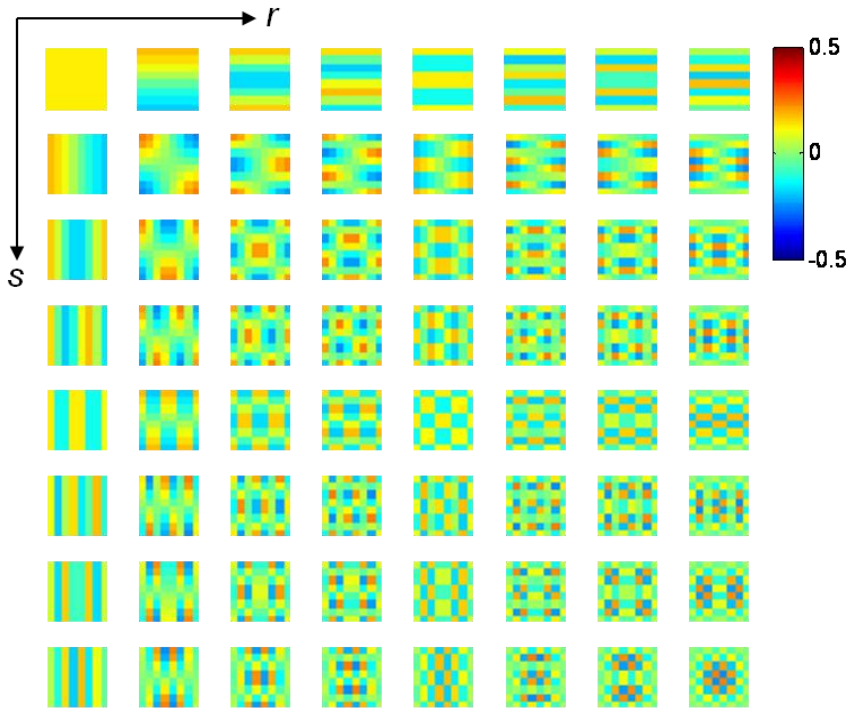

Figure 4-1 DCT basis for a 2-D model

4.2.2 Discrete Wavelet Transform Method

The Discrete Wavelet Transform is any wavelet transform for which the wavelets are discretely sampled (Mistry and Banerjee 2013), which is widely used in the image compression. The forward equation of the DWT is shown by Eq. 4.4 and Eq. 4.5, and the inverse equation is shown by Eq. 4.6.

$$\alpha(j,k) = \sum_{t} u(t)\, \phi_{j,k}(t) \tag{4.4}$$

$$\beta(j,k) = \sum_{t} u(t) \psi_{j,k}(t) \tag{4.5}$$

$$u(t) = \sum_{k} \alpha(j_0,k)\, \phi_{j_0,k} + \sum_{j=j_0}^{\infty} \sum_{k} \beta(j,k) \psi_{j,k} \tag{4.6}$$

where $t = 0, 1, 2, \ldots, N-1$, and $u(t)$ is the property parameter set. In Eq. 4.6, the scaling part, shown by the scaling coefficient $\alpha(j_0,k)$ and the scaling function $\phi_{j_0,k}(t)$, contains low frequency information, and the wavelet part, shown by the wavelet coefficient $\beta(j,k)$ and the wavelet function $\psi_{j,k}(t)$, contains high frequency information, which help depict reservoir boundaries shape and location. Jafarpour (2011) summarized that the scaling coefficients $\alpha(j,k)$ at scale j can be decomposed into the scaling coefficients $\alpha(j+1,k)$ and the wavelet coefficients $\beta(j+1,k)$ at the next coarser scale level j+1.

As shown in Figure 4-2 (b), after six levels of decomposition of a 2-D channelized reservoir (Figure 4-2 (a)), the first level in the upper left contains the scaling coefficients, corresponding to the average energy of the reservoir. The other five levels contain the wavelet coefficients, related with the detail information of the reservoir. The wavelet

coefficients, showing clear channel boundary shape in Figure 4-2 (b), are named as boundary coefficients, which helps depict the channel boundaries. For the DCT, Figure 4-2 (c) shows that the left corner contains high energy coefficients and no localization advantage is observed.

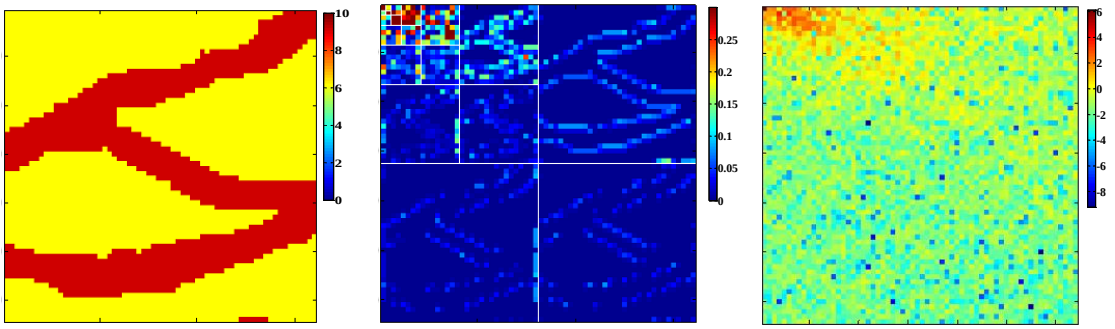

(a) 2-D channelized reservoir **(b) Scaled DWT coefficients** **(c) DCT coefficients**

Figure 4-2 Comparison between DWT and DCT parameterization coefficients: (a) 2-D channelized reservoir, (b) scaled DWT coefficients and (c) DCT coefficients.

Although compared to the DCT, the DWT can capture frequency and location information in the image reconstruction because of the existence of boundary coefficients, there are some obstacles for the DWT to be effectively used in the history matching. First, it is difficult to locate and estimate the significant DWT coefficients properly in the inverse problem (Jafarpour 2011). Second, the significant DWT coefficients, such as boundary coefficients, may not be sensitive to the observed data. We still can apply the DWT in history matching regardless of the coefficients' location and sensitivity to the observed data, although the breakthrough of these difficulties can improve the DWT history matching performance significantly.

4.2.3 Image Reconstruction Performance Comparison

In this section, the image reconstruction performance is compared among the DCT, GCT, and DWT. For each reparameterization method, 50, 500, and 1000 coefficients are taken to reconstruct the original image: the 2-D channelized reservoir shown in Figure 4-2 (a). The Root Mean Square Error (RMSE) (Eq. 4.7) is calculated to show the definition of reconstructed image. The less the RMSE value is, the smaller the difference between original image and reconstructed image.

$$RMSE = \sqrt{\frac{1}{n}\sum_{i=1}^{n}(y_i - \hat{y}_i)^2} \tag{4.7}$$

Figure 4-3 shows that for each reparameterization method, with the increase of number of coefficients, the images become clearer because more bases and energy are introduced. When the number of the coefficients is 50, the DCT reconstructed image is closer to the original one. However, when it increases to 500 or 1000, the DWT has the clearer definition of image with the smallest RMSE value compared with the other two, especially for the depiction of the channel boundary.

If the number of coefficients are introduced continuously, the RMSE is reduced with the increase of number of coefficients (Figure 4-4). With less than around 280 coefficients, the DCT is better than the others with the smallest RMSE value, while with more than 280 ones, the DWT shows the super performance. That is because we have more chances to include more boundary coefficients to help depict the image more clearly with the increase of number of coefficients. Figure 4-3 and Figure 4-4 stress the GCT's smooth effect compared with the DCT and DWT.

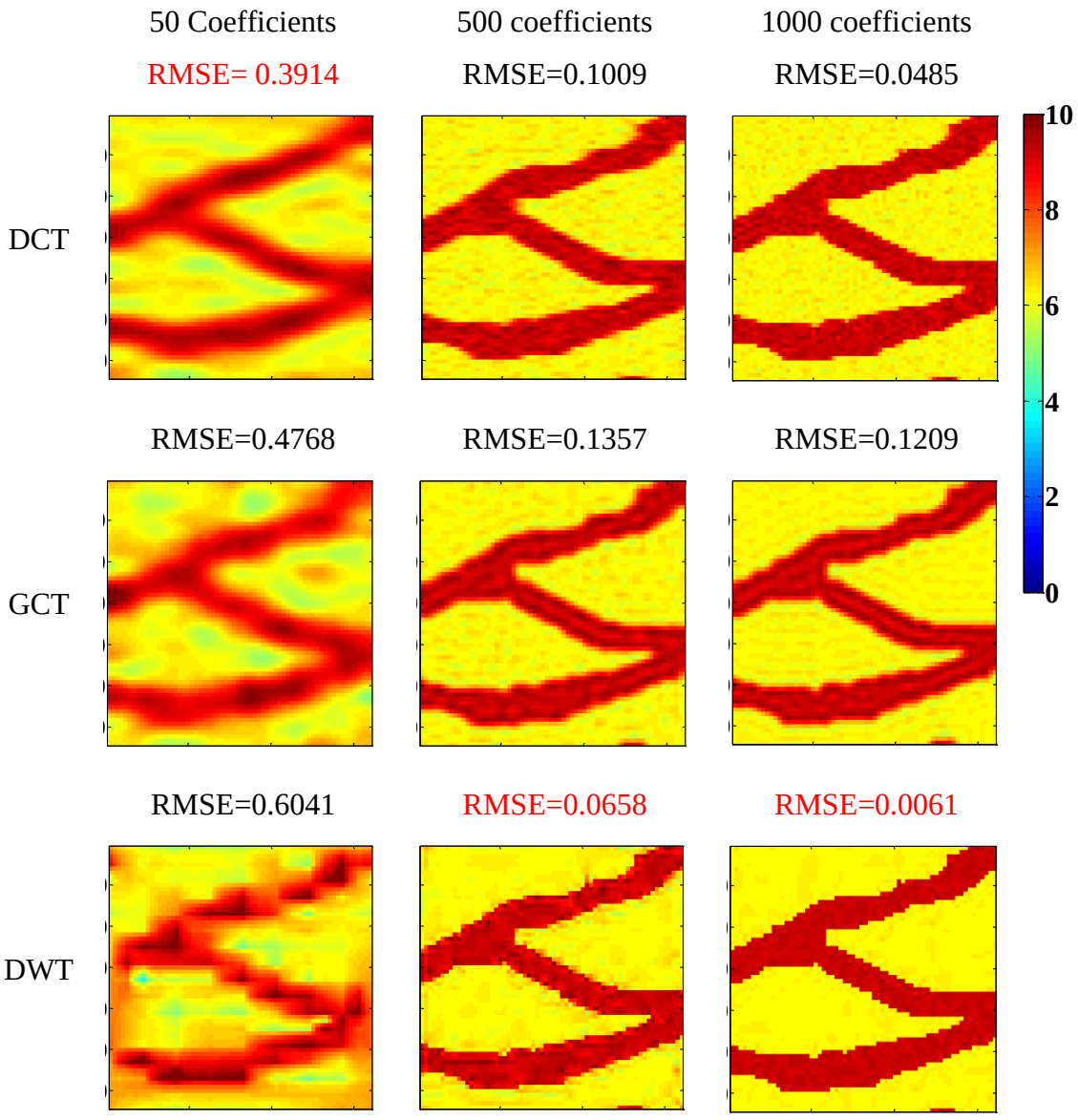

Figure 4-3 Image reconstruction performance comparison.

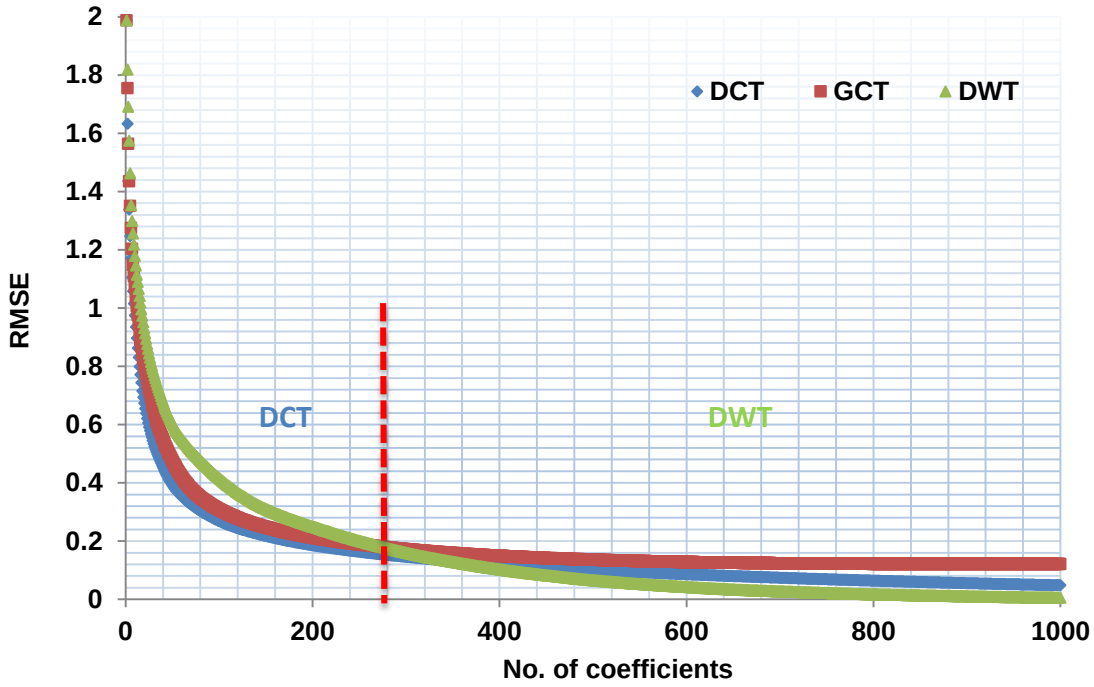

Figure 4-4 RMSE versus number of coefficients for the DCT, GCT, and DWT.

4.2.4 History Matching Performance Comparison

The channelized reservoir used for history matching has $50 \times 50 \times 1$ meshes with rectangular coordinates, and the two phases flow (oil and water) is considered. Three injectors are under pressure control, and four producers are under oil rate control. The true permeability model is heterogeneous, and the initial model is homogeneous within the channel (Figure 4-5). The average permeability of channel for both models is 300md, and floodplain's perm is 0.01md. Here, we assume the flow dynamics are bounded within the channel, and the floodplain's flow effect is negligible. Compared to the true model, the initial model connects the path between producer 2 and injector 2, and disconnects the path between producer 1 and producer 3. Through history matching oil rate, water cut,

producer BHP, and water injection rate, we aim to reproduce the main structure of the true model starting from the initial model.

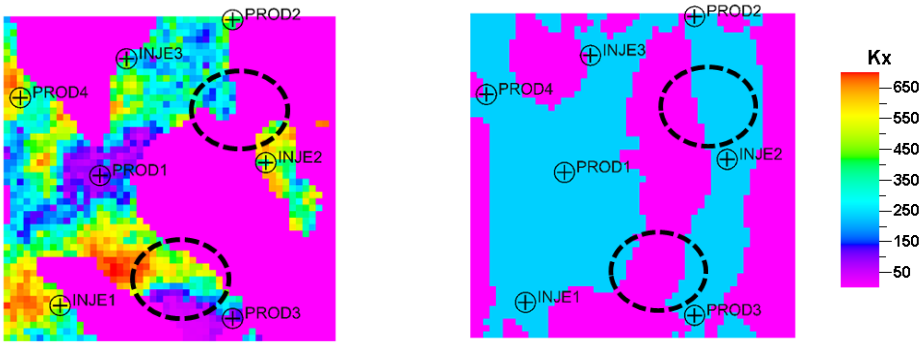

(a) True model **(b) Initial model**

Figure 4-5 The true and initial models in a 2-D case.

History matching objective is the summation of four objectives misfit — oil rate, water cut, producer BHP, and water injection rate — between observed historical data and calculated reservoir simulation results. The MCMC (Hastings 1970; Xie et al. 2011) is employed to update reparameterization coefficients in order to minimize history matching objective. Figure 4-6 (a) shows the acceptance rate variation of the DCT, GCT, and DWT with the increase of iterations. Although the acceptance rate can reduce to the stationary state after 500 iterations, the low value (below 10%) means that the proposals brought by these three parameterization methods are not good enough. Also, the overall data misfit is reduced from 4000 to 2000, which is still relatively high. The level set method can reduce the data misfit further, which will be shown in the next section. Only one sample is picked from the stationary state of these three methods respectively to compare updated permeability models with the true model (Figure 4-7). Although the low permeability is

around producer 1 can be captured, the channel boundaries are smeared, which causes the low acceptance rate and relatively high history matching data misfit. In the respect of history matching results, there is no big difference between the three parameterization methods. Generally, direct application of the DCT, GCT, and DWT on channelized reservoir history matching is not satisfied.

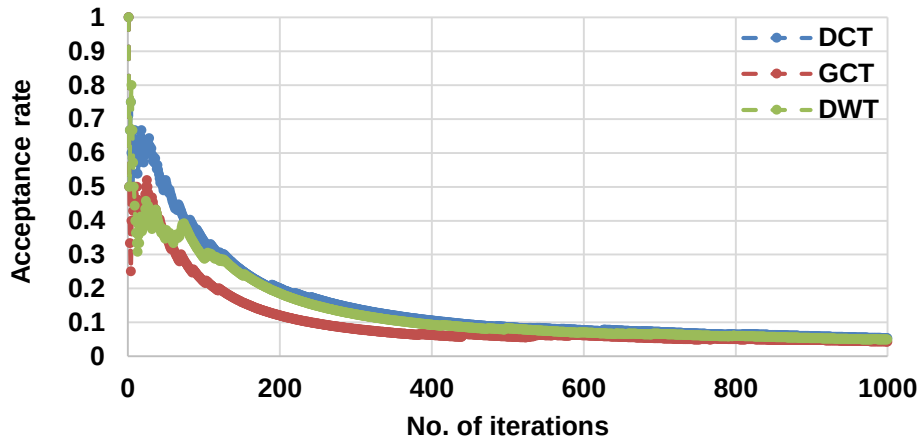

(a) Acceptance rate versus number of iterations for Markov chain.

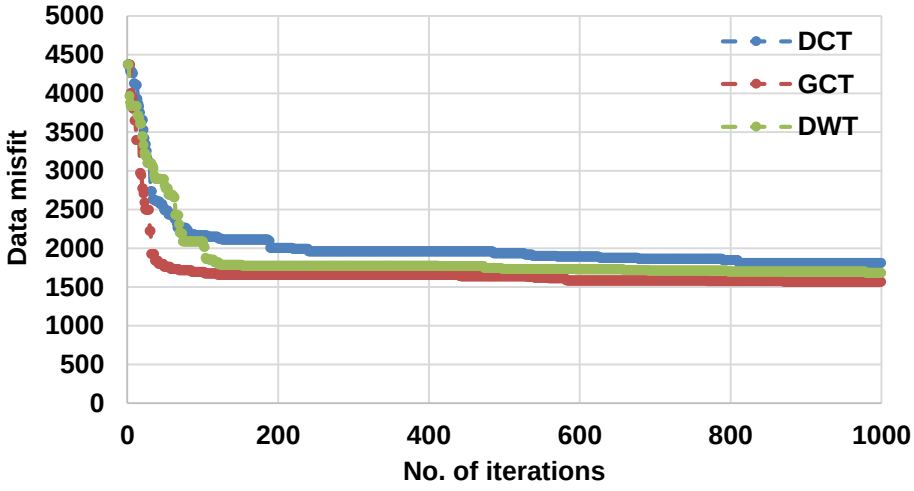

(b) Data misfit versus number of iterations for Markov chain.

Figure 4-6 MCMC simulation performance: (a) acceptance rate, (b) data misfit

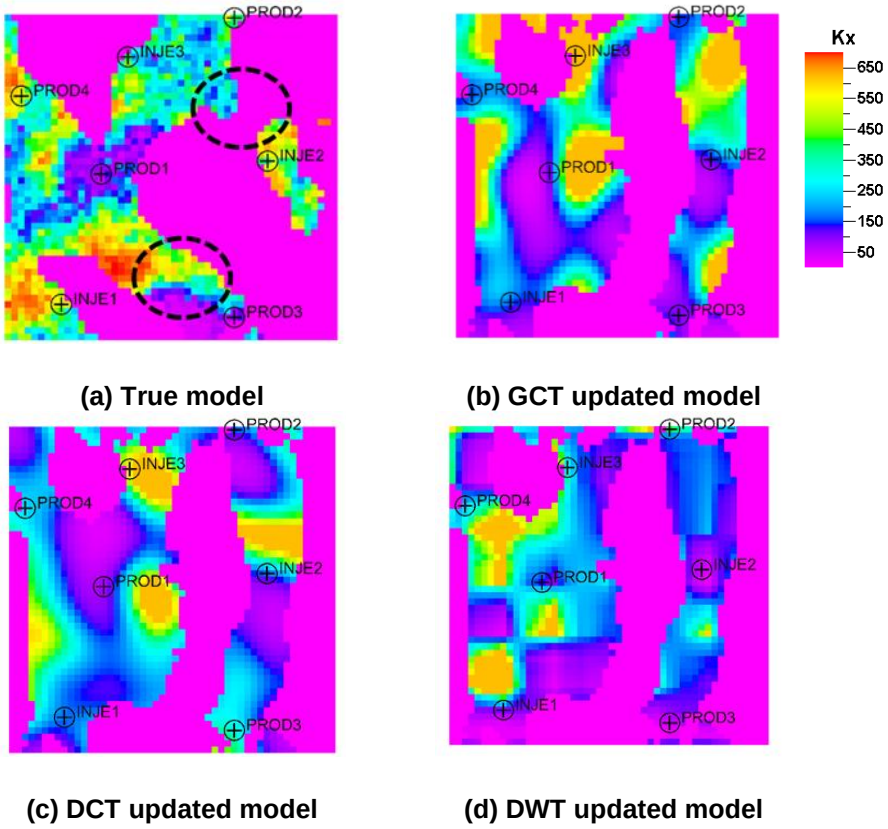

(a) True model **(b) GCT updated model**

(c) DCT updated model **(d) DWT updated model**

Figure 4-7 Update models for synthetic case.

4.3 Level Set Method as an Alternative

The level set method can be used to update facies model as an alternative. In this section, we first introduce the level set method to show how the level set method transform discrete facies into continuous variables, and how it gradually changes channel geometry in the continuous domain, followed by property model calibration using GCT. Then we demonstrate our approach using a 2-D channelized reservoir example.

4.3.1 Level Set Method Methodology

The level set method is a numerical algorithm for dynamic implicit surfaces and evolution (Osher and Fedkiw 2002; Osher and Sethian 1988; Osher and Santosa 2001). The implicit surface is defined as function $\varphi(t,x)$.

$$\begin{aligned} \Gamma &= \{x \in \Omega | \varphi(t,x) = 0\} \\ \Omega^+ &= \{x \in \Omega | \varphi(t,x) > 0\} \\ \Omega^- &= \{x \in \Omega | \varphi(t,x) < 0\} \end{aligned} \tag{4.8}$$

Take the 2-D channel model for example (Figure 4-8 (a)). Domain Ω^+ is surrounded by a closed curve Γ. Outside domain area is Ω^-. When $\varphi(t,x) > 0$, it represents the area within the domain (Ω^+), corresponding to the channel/sand facies in the 2-D channel model. When $\varphi(t,x) > 0$, it represents the area outside domain (Ω^-), corresponding to the floodplain/shale facies. When $\varphi(t,x) = 0$, it is the closed curve (Γ), which is called zero level set of the function $\varphi(t,x)$, corresponding to facies boundary.

However, the implicit surface is discontinues, which is difficult to be solved for facies boundary evolution. The signed distance function (SDF), $\varphi_d(t,x)$, can be used to avoid discontinuous the implicit surface. The signed distance function is defined as the smallest distance between any point in the reservoir and facies boundary (Xie et al. 2011). When the point is within the channel, the positive distance is assigned to $\varphi_d(t,x)$. Otherwise, the negative one will be assigned (Eq. 4.9).

$$\varphi_d(t,x) = \begin{cases} distance\ (x,\Gamma) & \forall x \in \Omega^+ \\ -distance(x,\Gamma) & \forall x \in \Omega^- \end{cases} \tag{4.9}$$

To achieve the signed distance function, the reinitialization equation Eq. 4.10 need to be solved.

$$\frac{\partial \varphi_d(t,x)}{\partial t} + sign\big(\varphi_d(0,x)\big)(|\nabla \varphi_d(t,x) - 1|) = 0 \tag{4.10}$$

where

$$sign\big(\varphi_d(0,x)\big) = \begin{cases} 1 & x \in \Omega^+ \\ -1 & x \in \Omega^- \end{cases} \tag{4.11}$$

After the reinitialization equation reaches the stead state, SDF has a nice property:

$$|\nabla \varphi_d(t,x)| = 1 \tag{4.12}$$

Figure 4-8 (b) shows the signed distance function after solving the reinitialization equation of the 2-D channel model (Figure 4-8 (a)).

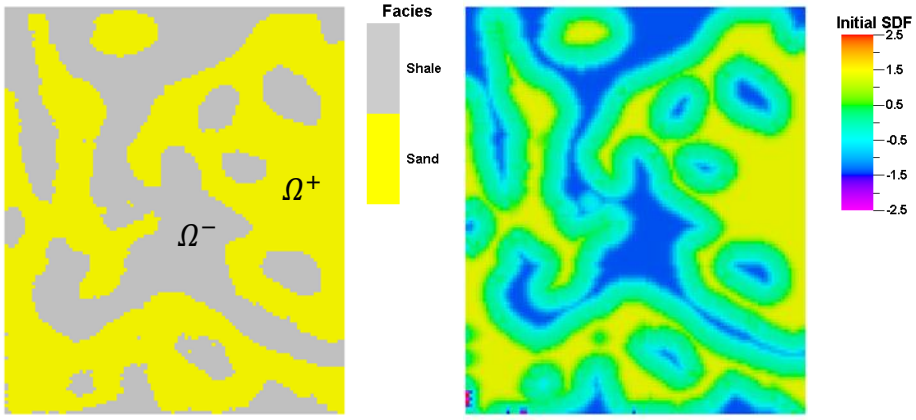

(a) 2-D Channel model **(b) Signed distance function**

Figure 4-8 2-D channel model and its singed distance function.

Then, Eq. 4.12 is applied into the level set equation Eq. 4.13, which is related with the facies boundary evolvement.

$$\frac{\partial \varphi_d(t,x)}{\partial t} + v_n(x)\left|\nabla \varphi_d\,(t,x)\right| = 0 \tag{4.13}$$

$v_n(x)$ is the normal velocity. Discretize Eq. 4.13, which is can be rewritten as Eq. 4.14:

$$\frac{\varphi_d^{t+1} - \varphi_d^t}{\Delta\, t} = -v_n(x) \tag{4.14}$$

Finally, we get the following equation:

$$\varphi_d^{t+1} = \varphi_d^t - v_n(x)\Delta t \tag{4.15}$$

Δt is the artificial time, rather than the physical time, which can be assigned any values here. φ_d^t is the current SDF starting from the initial model's SDF, like the one shown in Figure 4-8 (b). In order to get φ_d^{t+1}, which is the next time step SDF, the only unknown is $v_n(x)$.

The Sequential Gaussian Simulation (SGSIM) is used to generate the Gaussian random field (GRF) as velocity (Remy et al. 2009; Xie et al. 2011). If we want to condition the new facies model to facies observations at well locations, we can easily set the GRF as 0 at wells. Thus, there is no variation for $\varphi_d(t,x)$ over time.

Figure 4-9 illustrates how to update facies model by conditioning hard data. First, solve the reinitialization equation to get initial model's SDF. Second, generate the GRF as velocity field, and condition the GRF to 0 at well locations to preserve facies observation. Third, by adding velocity field (GRF) to initial model's SDF, obtain the deformed SDF. Finally, transform back from the deformed SDF to the new facies based on the principle that positive value in the deformed SDF corresponds to the channel in new facies model and negative value corresponds to the floodplain facies.

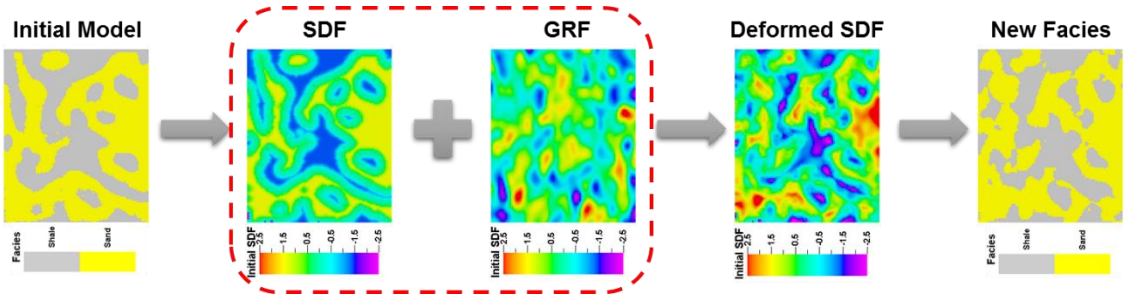

Figure 4-9 Facies boundary perturbation flowchart.

4.3.2 Two-Step Channelized Reservoir Calibration Workflow

After facies calibration, property modeling within the channel is evolved. Figure 4-10 shows a two-step history matching workflow for channelized reservoirs involving facies modeling and property modeling. The property modeling is as same as the process mentioned in section 4.2.4. The difference is that we update facies model first, followed by property calibration using the GCT. The reason why we choose the GCT here is that the DCT is limited in the regular grid structure and the DWT's localization advantage is difficult to be fully used in the history matching. Also, the GCT method has been successfully applied in the field-scale history matching (Watanabe et al. 2013), which can help enhance the applicability and stability of the level set in the field-scale application. Furthermore, since channels dominate the flow dynamics, we only update permeability within the channel, and keep the floodplain's properties unchanged. The explanation for this flowchart is as follows:

(a) Transform initial model to the SDF domain.

(b) By adding the GRF, transform back and propose new channel model.

(c) Check the proposed channel model with the sand/shale ratio. If it is satisfied, run forward reservoir simulation. Otherwise, go back to propose another new channel model.

(d) Based on the MCMC acceptance probability to accept or reject the new facies proposals. After reaching stop criteria, the calibrated facies models are fed into property modeling process.

(e) Utilize the GCT to parameterize property model into the linear combination the GCT bases and GCT coefficients.

(f) Apply the MCMC to optimize the GCT coefficients in order to propose new property models.

(g) Still based on the MCMC acceptance probability to accept or reject the new property proposals. The final calibrated reservoir models can be got after reaching stop criteria.

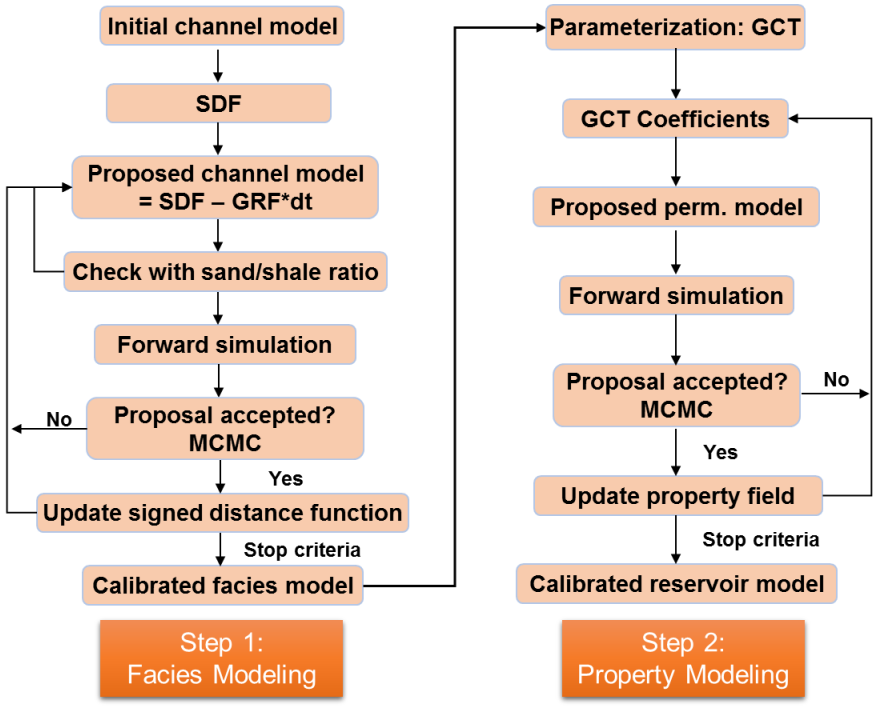

(a) Step 1: Facies modeling **(b) Step2: Property modeling**

Figure 4-10 A two-step history matching workflow: (a) facies modeling, (b) property modeling.

4.3.3 A 2-D Case Application

As mentioned in the section 4.2.4, the calibration on property without facies update using traditional parameterization methods does not apply very well on the channelized reservoirs. For comparison purpose, we applied the level set method on the same 2-D example (Figure 4-5) to calibrate facies first, followed by property calibration using the GCT.

Through the facies modeling workflow (Figure 4-10 (a)), Figure 4-11(a) shows that after 500 iterations, the acceptance rate in the MCMC using the level set method reaches to around 20% (orange line), which is higher than that of the other three methods. Also,

the data misfit (orange line) is reduced down to 500, which is lower than the other three (Figure 4-11 (b)). Four realizations sampled from the stationary state are displayed in Figure 4-12. Although the channel distributions are different with each other, the key feature of channel architecture is captured. For instance, the path between producer 2 and injector 2 is reconnected, and the one between producer 1 an producer 3 is disconnected in comparison with true and initial models. Since the channel distribution dominates reservoir fluid flow, and updated facies models can reproduce the pivotal flow path of the true model, the good proposals make acceptance rate higher and history matching data misfit lower.

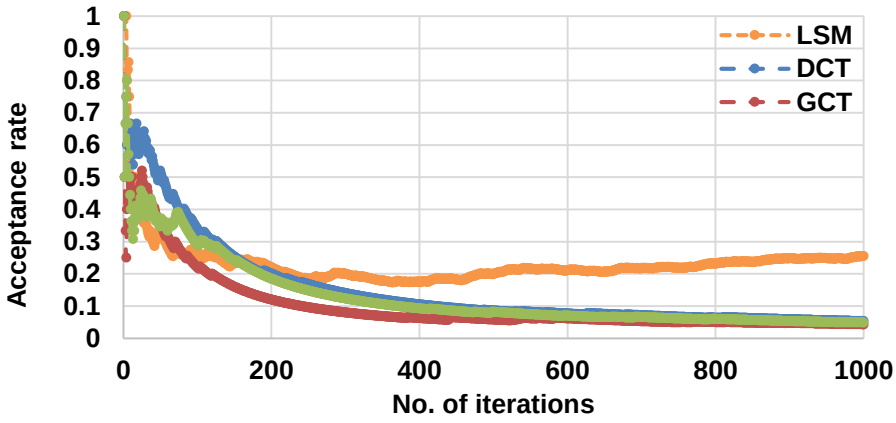

(a) Acceptance rate versus number of iterations for Markov chain.

Figure 4-11 MCMC simulation performance in facies model calibration: (a) acceptance rate, (b) data misfit.

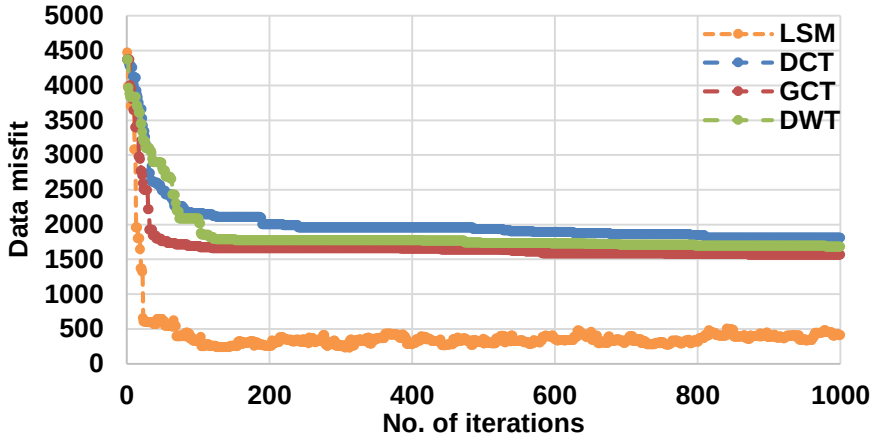

(b) Data misfit versus number of iterations for Markov chain.

Figure 4.11 continued.

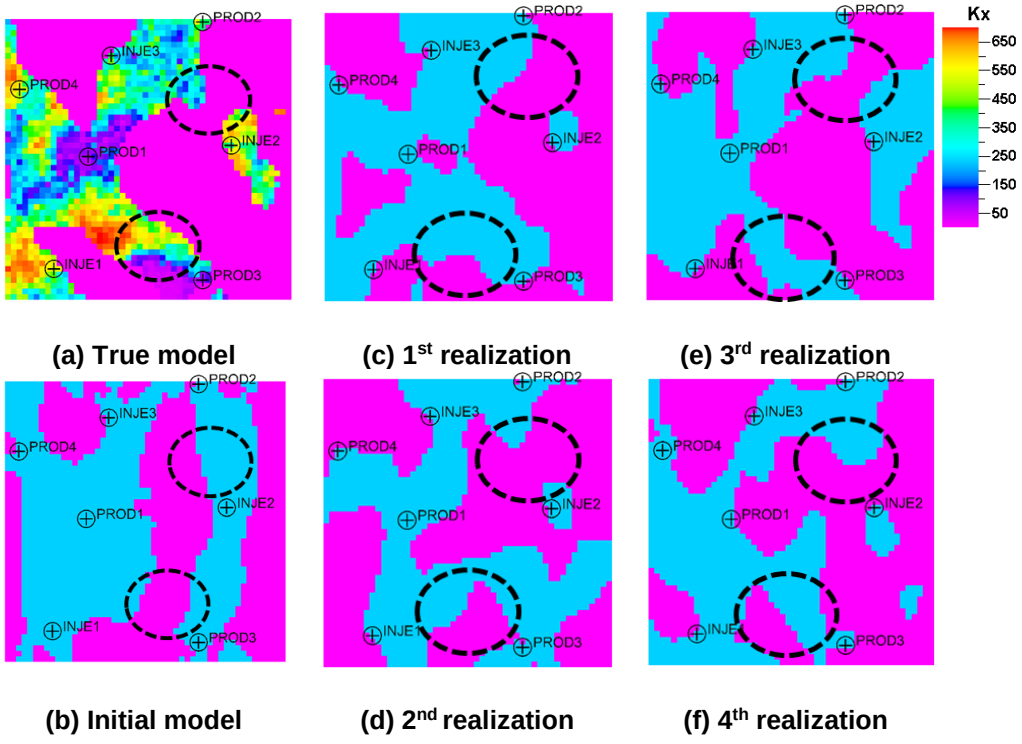

(a) True model **(c) 1st realization** **(e) 3rd realization**

(b) Initial model **(d) 2nd realization** **(f) 4th realization**

Figure 4-12 Calibrated facies models versus true and initial models.

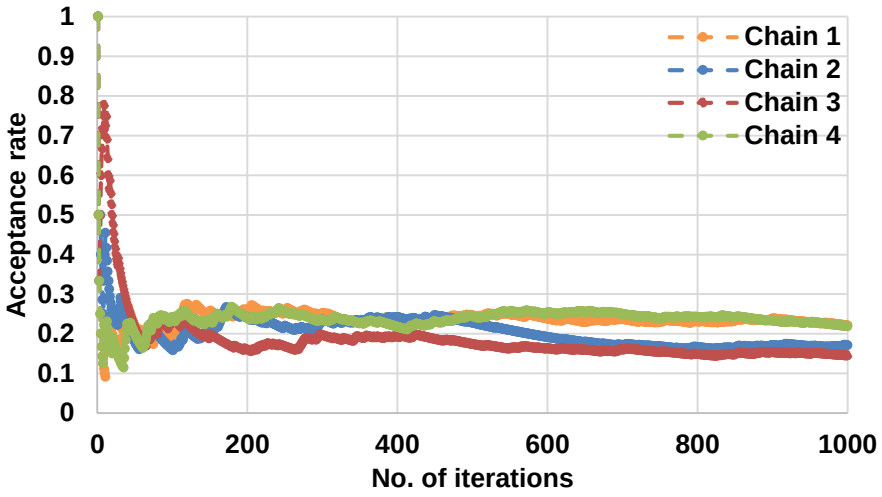

(a) Acceptance rate versus number of iterations for Markov chain

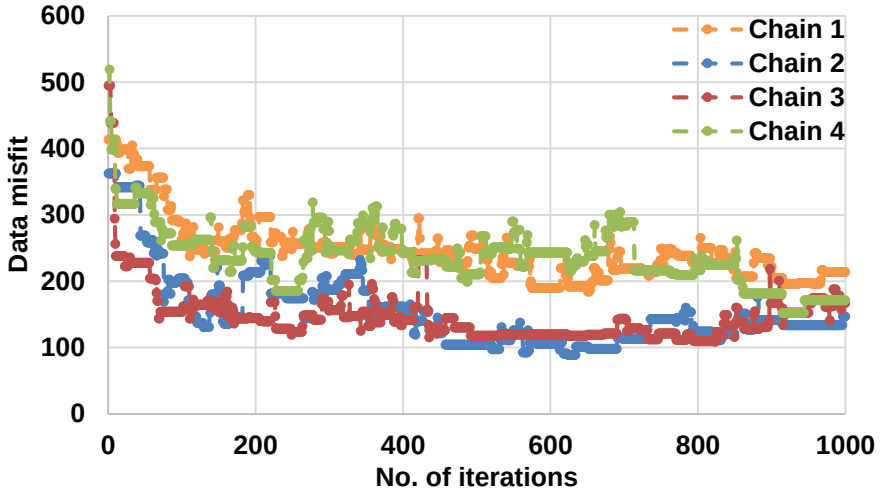

(b) Data misfit versus number of iterations for Markov chain.

Figure 4-13 MCMC simulation performance in property model calibration: (a) acceptance rate, (b) data misfit.

The four facies models (Figure 4-12) serve as starting models in the property models calibration process. The GCT is used to parameterize these four models into spectral domain, and 20 GCT coefficients are updated by the MCMC. Hence, four MCMC chains

are shown in Figure 4-13. It is clearly to see that the acceptance rate of four chains are around 20%, and the data misfit is reduced further from 500 to 200. Another four property realizations are sampled from the stationary state to present property change staring from homogeneous state (Figure 4-14). The high and low permeability regions are clearly depicted within the channel. For example, the feature of low permeability around producer 1 and high permeability around producer 4 are captured. Thus, with the help of facies model updated using the level set method, the property calibration can reach to a better level compared with using parameterization directly on the channelized reservoir. Figure 4-15 shows well by well history matching results. The updated models (blue lines) can match observed data (red dots) very well for oil rate, water cut, producer BHP, and water injection rate.

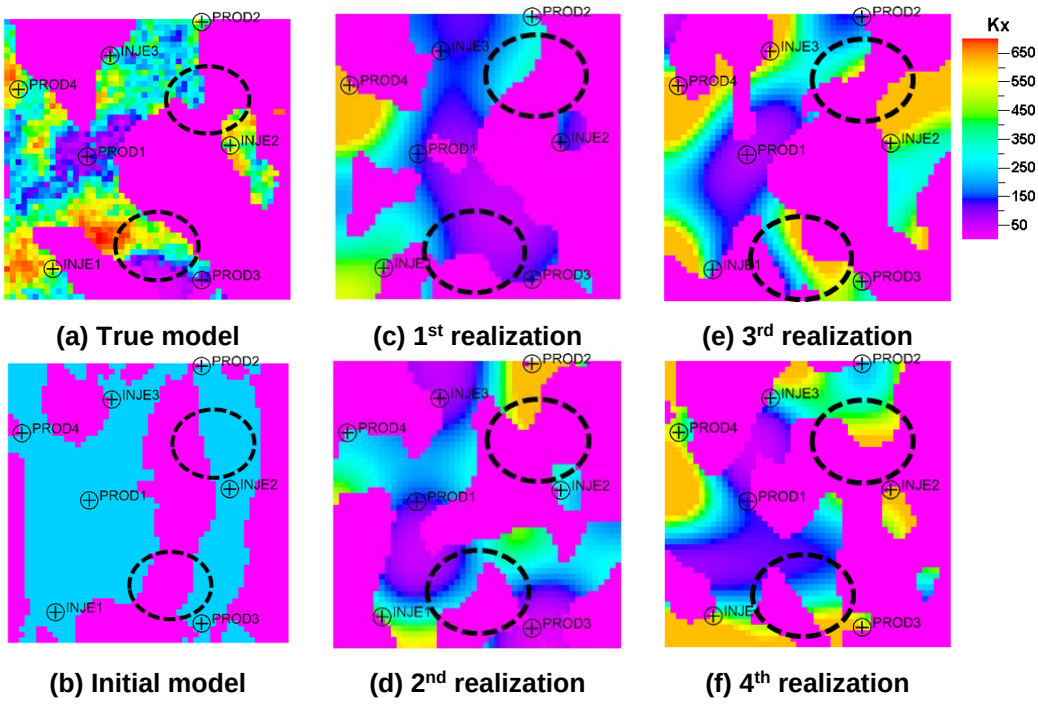

Figure 4-14 Calibrated property models versus true and initial models.

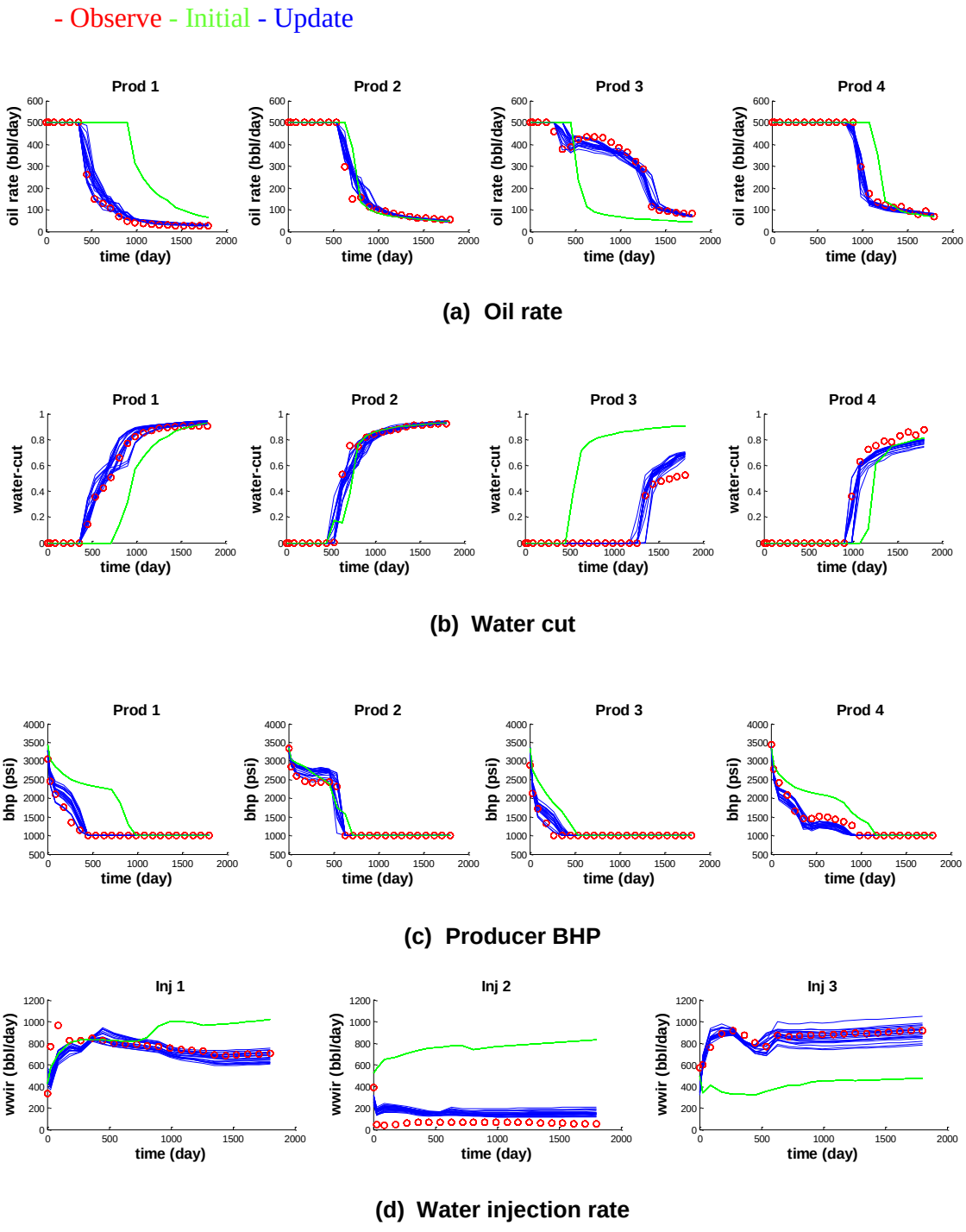

Figure 4-15 History matching results: (a) oil rate, (b) water cut, (c) producer BHP, (d) water injection rate.

4.4 Level Set Method under Seismic Constraint

The seismic constraint plays an important role for the complicated channel reservoirs. Thus, although the level set method serves as a great alternative to change facies boundary, we still need to know how to incorporate seismic information into the level set when seismic data is available. In this section, we first present the methodology of seismic integration in the level set method. Then a 2-D channelized reservoir is used to show how seismic integration can help to reproduce the channel structure.

4.4.1 Level Set Method under Seismic Constraint Methodology

There are many types of seismic derived information. Here, we take the seismic acoustic impedance (AI) for example in the rest of discussion. Assume that the seismic acoustic impedance has the same resolution as the reservoir model after seismic processing after seismic processing, and there is a good relationship between the acoustic impedance values and the types of facie. In this assumption, seismic derived facies can be obtained from given measured AI model. Figure 4-16 shows the seismic data integration flowchart. First of all, the initial facies model is represented by the initial SDF; second, the seismic derived facies is acquired from the measured AI model, followed by the AI SDF; third, the initial SDF and AI SDF are combined together to generate the deformed initial SDF and transform back to get the new initial facies model.

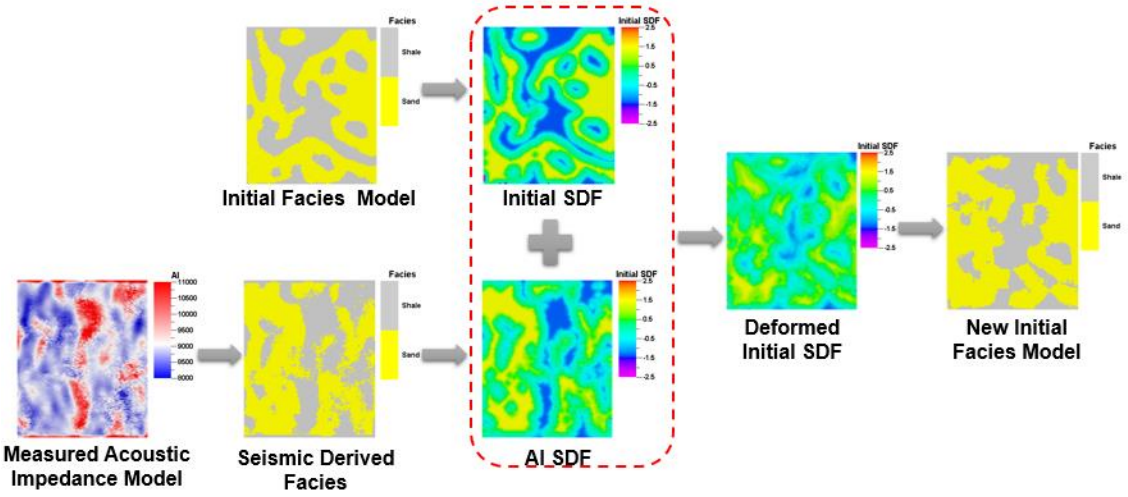

Figure 4-16 Facies boundary perturbation under seismic constraint flowchart.

$$\varphi_d^{t_0} = \varphi_g + w(\varphi_{AI} - \varphi_g) \tag{4.16}$$

Eq. 4.16 shows how to combine the initial SDF and AI SDF. φ_g is the initial SDF, φ_{AI} is the AI SDF, and $\varphi_d^{t_0}$ is the deformed SDF after combination. w is the seismic weight, describing how strong an impact of the AI SDF should have on the deformed SDF. 0 means no correlation at all, while 1 means 100% correlation between φ_{AI} and $\varphi_d^{t_0}$. As shown in Figure 4-17, initially we have the initial facies model and seismic derived facies. A range of w from 0 to 1 at interval of 0.2 is assigned to Eq. 4.16 to get the deformed SDF, which is transformed back to facies model. When w is equal to 0, the transformed facies model is almost identical with the initial facies model without seismic influence. With the increase of w, the transformed facies becomes more similar with the seismic derived facies, away from the initial facies model. When w is equal to 0.6, the transformed facies has captured the main feature of the seismic derived facies. When w is equal to 1, $\varphi_g$is canceled, and only φ_{AI} takes effect without any initial model impact.

The seismic weight plays the same function as the correlation coefficient used to determine the impact of the secondary variable in the co-kriging of the geological modeling. The determination of the seismic weight is subjective, based on the prior knowledge of seismic information and geological knowledge. As shown in Figure 4-18, the only difference in the new two-step history matching flowchart under seismic constraint, compared with the one without seismic, is that the initial model is integrated with seismic information, and the rest of the workflow remains unchanged.

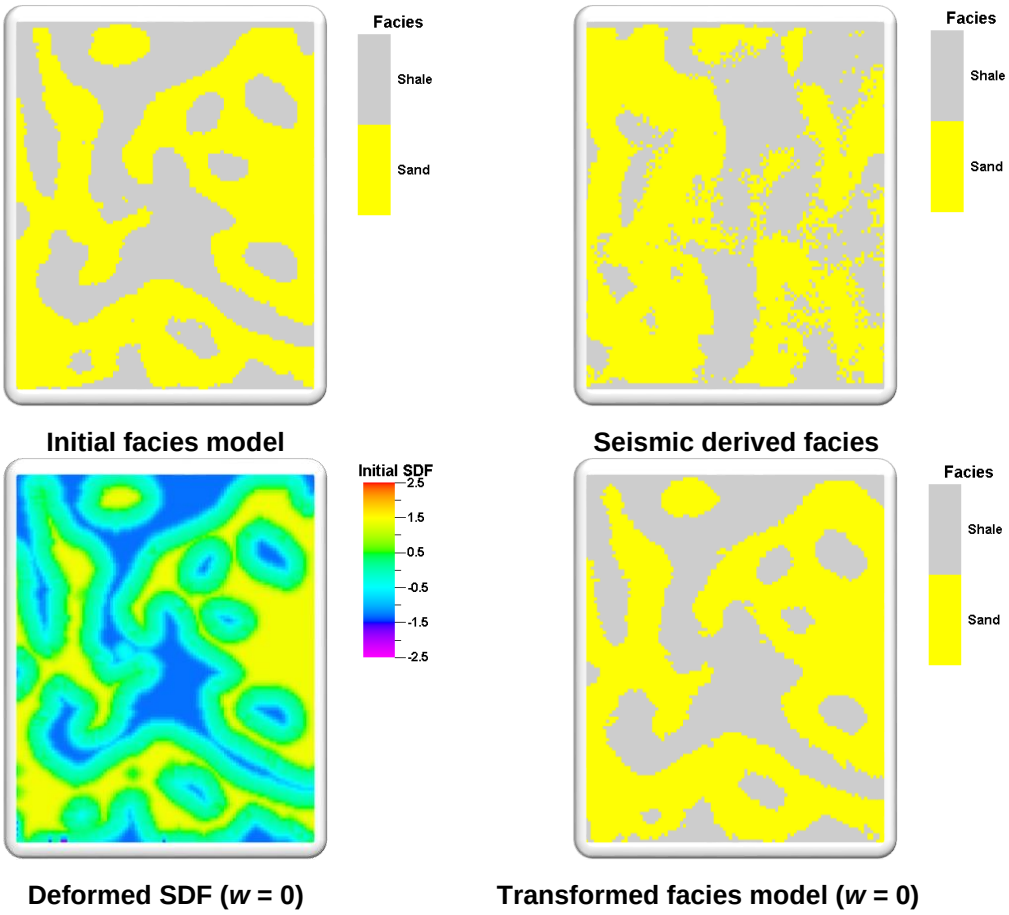

Figure 4-17 Seismic weight impact on facies perturbation.

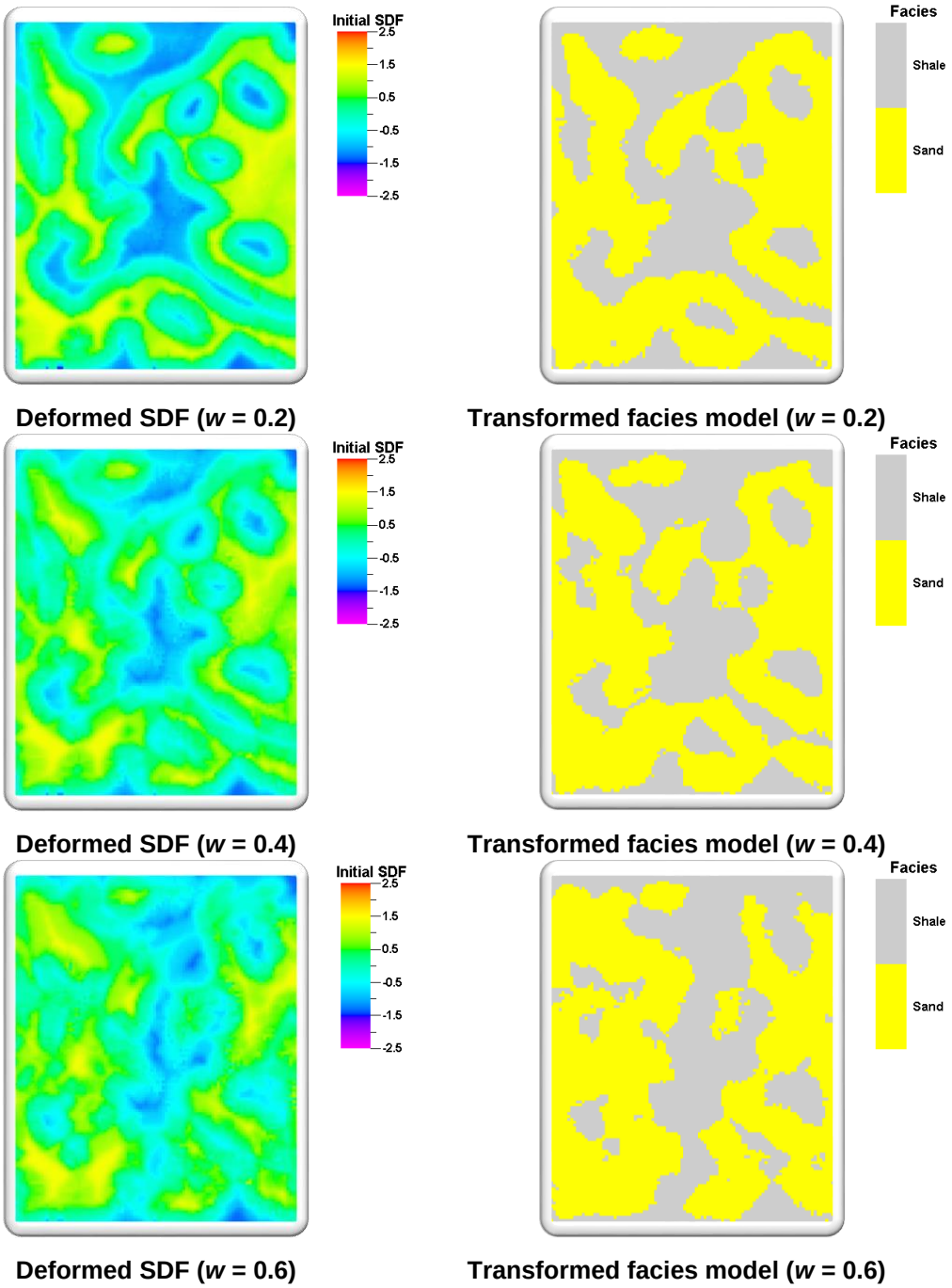

Figure 4.17 continued.

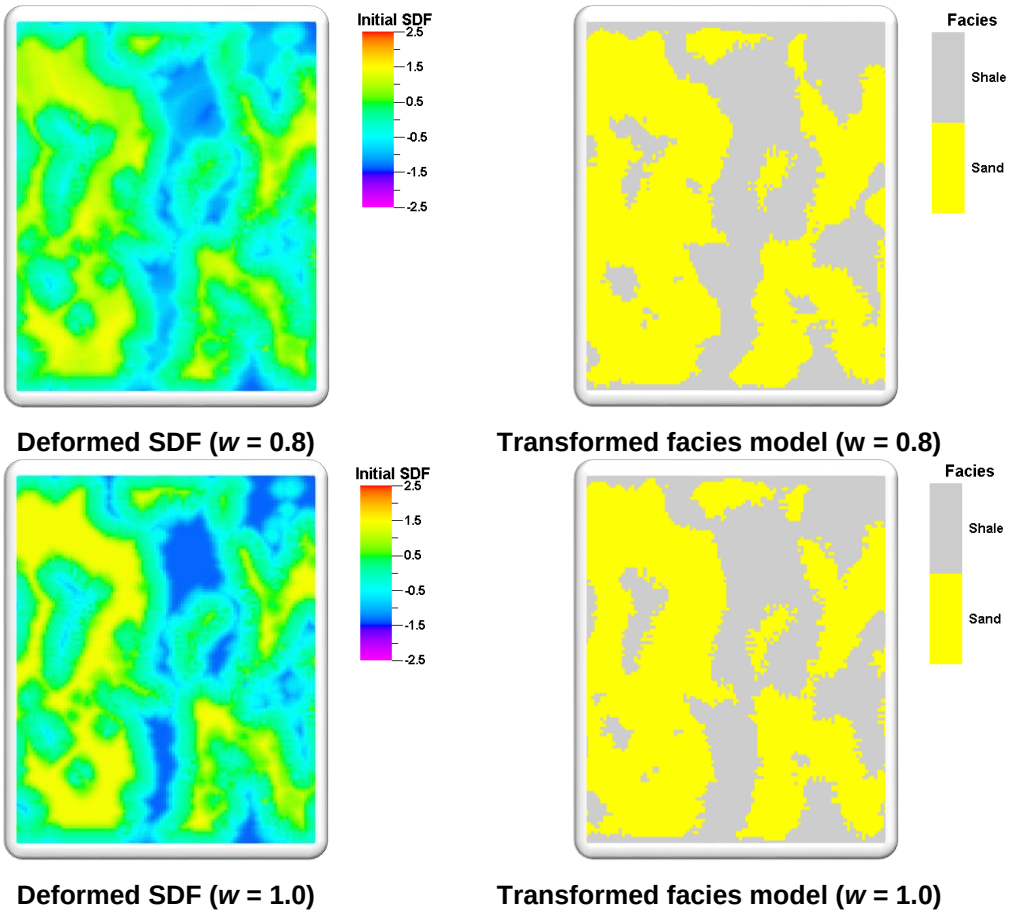

Figure 4.17 continued.

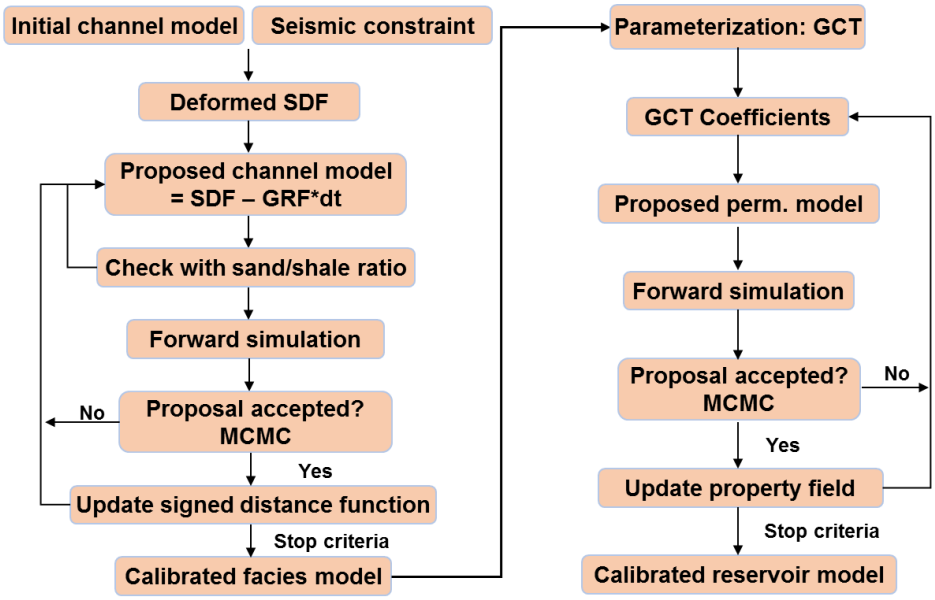

Figure 4-18 A two-step history matching workflow under seismic constraints: (a) facies modeling, (b) property modeling.

4.4.2 A 2-D Case Application

The 2-D channelized reservoir (Figure 4-19) is a modified version of the Stanford V reservoir (Mao and Journel 1999). The reservoir model has 100×120×1 grids, and two-phase flow (oil and water) is considered. There are three injectors at pressure control, and three injectors at oil rate control. As in the 2-D model in section 4.2.4, only flow dynamics within the channel is considered. Also, the true permeability model is heterogeneous, and initial model is homogeneous within the channel. The average permeability of channel for both models is 300md, and floodplain's perm is 0.01md. Compared to the true permeability model (Figure 4-19 (a)), the path is connected between producer 3 and injector 3 in the initial permeability model (Figure 4-19 (b)). The measured acoustic

impedance model (Figure 4-19 (c)) serves as the seismic constraint in the facies model calibration process.

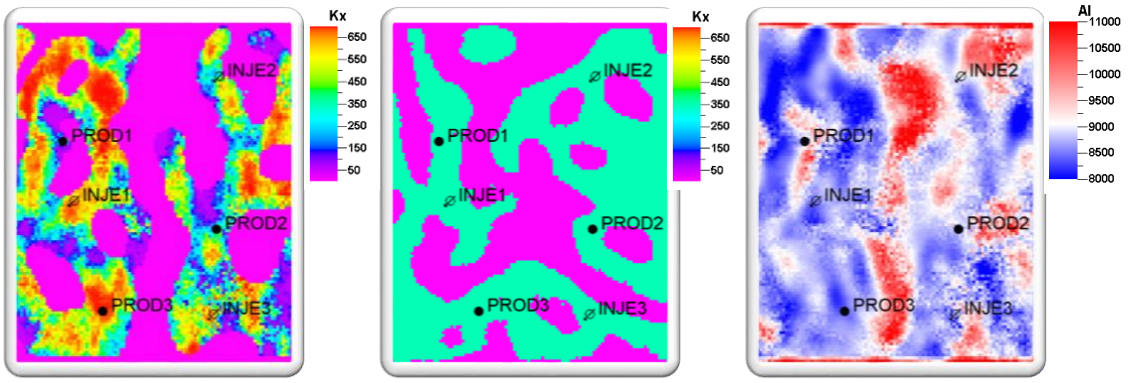

(a) True permeability model **(b) Initial permeability model** **(c) Measured acoustic impedance model**

Figure 4-19 A 2-D synthetic case: (a) true permeability model, (b) initial permeability model, (c) measured acoustic impedance model.

According to the seismic integration workflow (Figure 4-16 and Figure 4-18), different $\boldsymbol{w}$ values are assigned to show the seismic weight influence on the facies model evolution. Figure 4-20 shows the acceptance rate and data misfit within 500 iterations when $\boldsymbol{w}$ is equal to 0, 0.5, 0.7 in the facies update step. For discussion purpose, the cases when $\boldsymbol{w}$ is equal to 0, 0.5, 0.7 are named as case 1, case 2, and case 3 respectively. Data misfit (Figure 4-20 (b)) decreases largely from about 28000 to below 1000. The red dash area is magnified and left corner is focused on in Figure 4-20 (c). Case 2 and 3 with the seismic constraint reach to lower data misfit compared with case 1 without the seismic constraint, and especially larger $\boldsymbol{w}$ contributes to the lower data misfit. Then, three facies realizations are sampled from the stationary sate for each case (Figure 4-21, Figure 4-22 and Figure 4-23). It is clear that with the increase of $\boldsymbol{w}$, the seismic constraint imposes the stronger

impact on facies model evolution, and the three realizations become more similar with the true model. In particular, the path between producer 3 and injector 3 in the 3rd realization is still connected without the seismic constraint (Figure 4-21 (d)), although the data misfit is reduced enough, and acceptant rate is also acceptable (Figure 4-20 (a)).

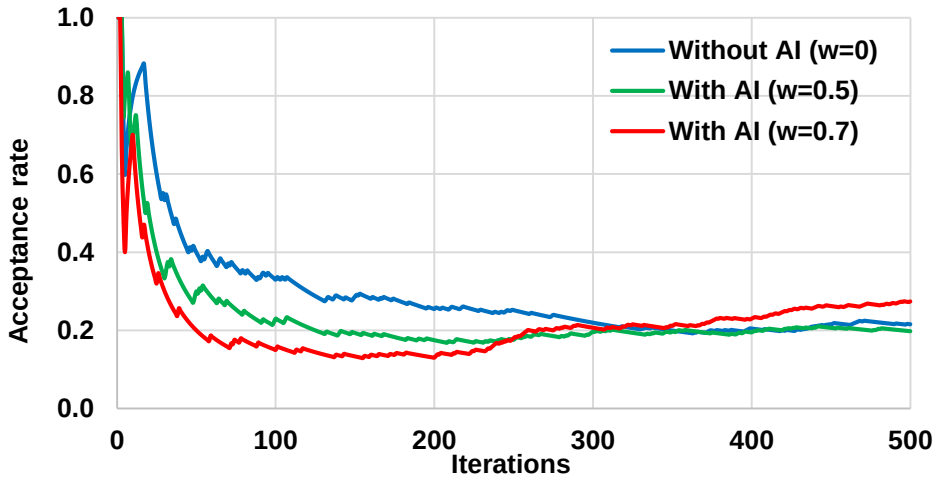

(a) Acceptance rate versus number of iterations for Markov chain.

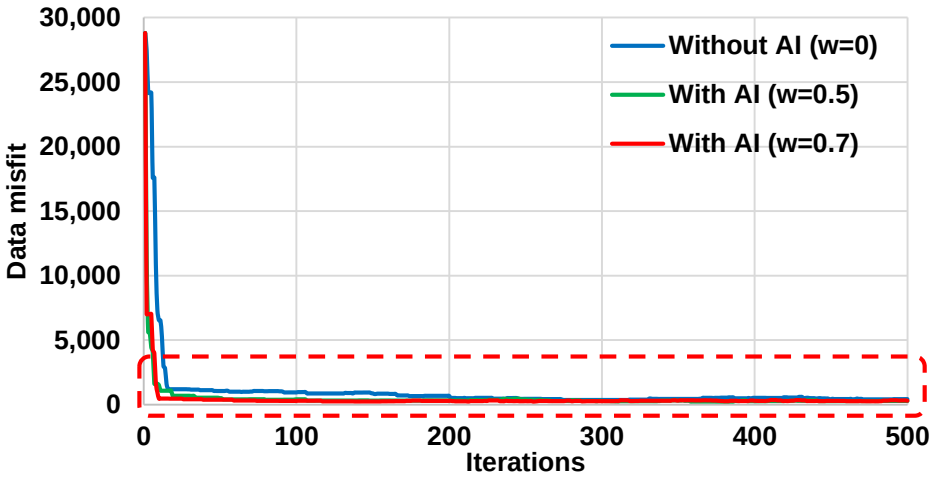

(b) Data misfit versus number of iterations for Markov chain.

Figure 4-20 MCMC simulation performance in facies model calibration: (a) acceptance rate, (b) data misfit, (c) amplified data misfit area.

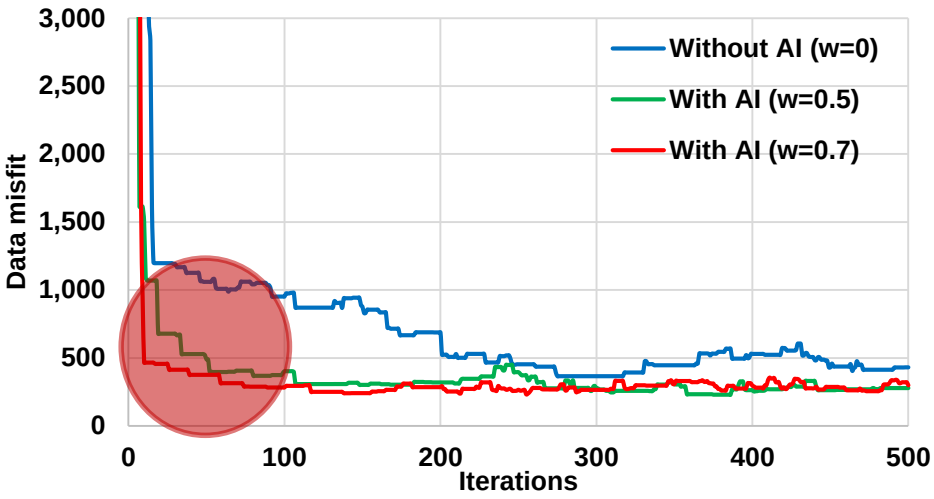

(c) Data misfit versus number of iterations for Markov chain (Amplified area).

Figure 4.20 continued.

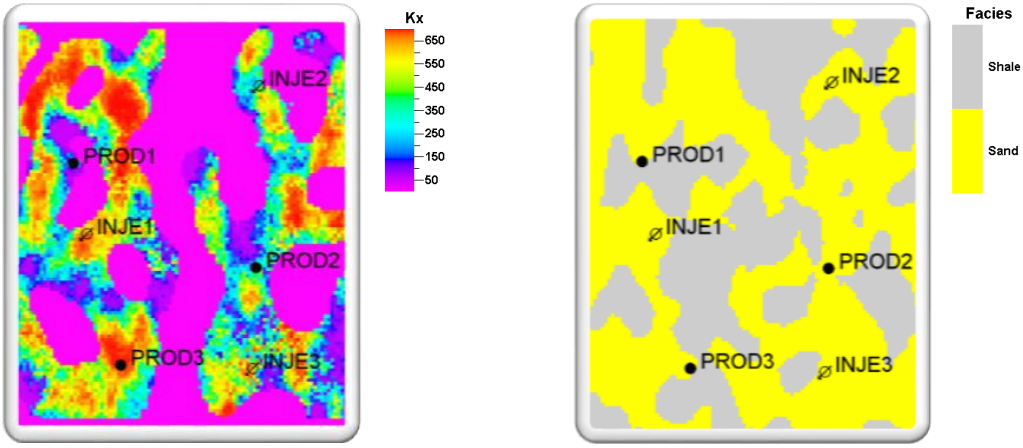

(a) True model **(b) 1st Facies realization**

Figure 4-21 Calibrated facies models versus true model ($w = 0$).

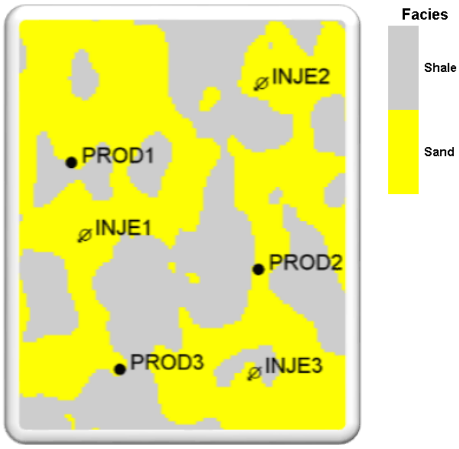

(c) 2nd Facies realization

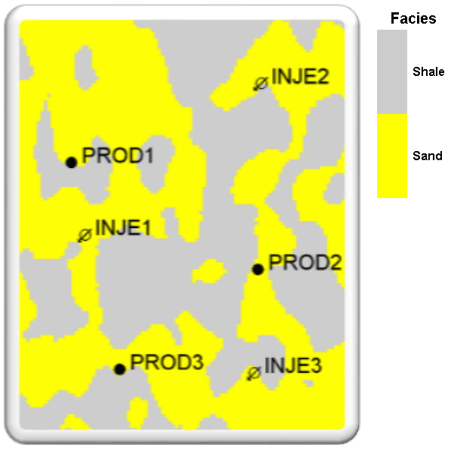

(d) 3rd Facies realization

Figure 4.21 continued.

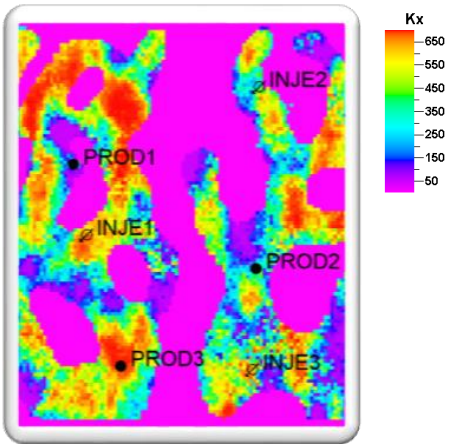

(a) True model

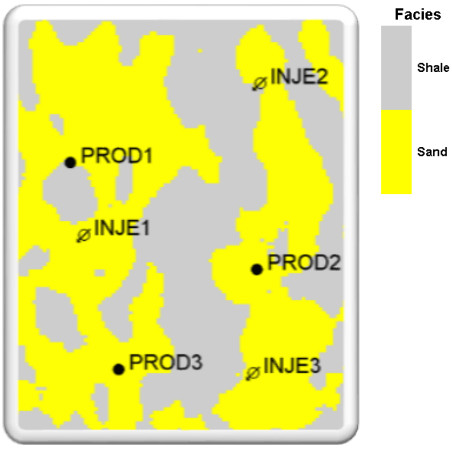

(b) 1st Facies realization

Figure 4-22 Calibrated facies models versus true model ($w = 0.5$).

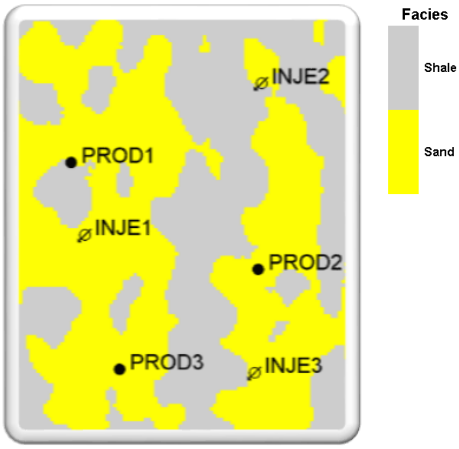

(c) 2nd Facies realization

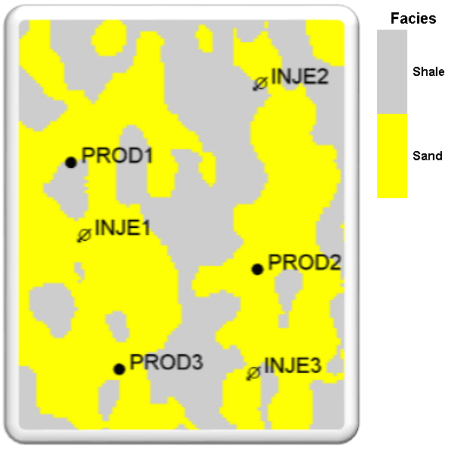

(d) 3rd Facies realization

Figure 4.22 continued.

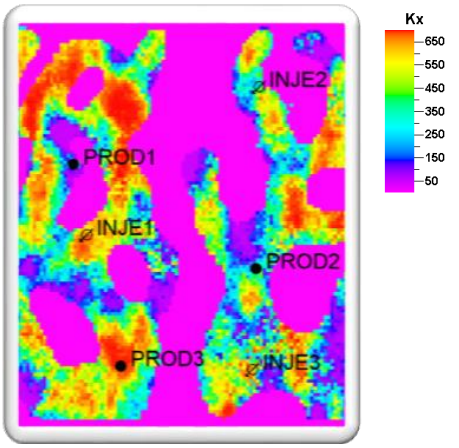

(a) True model

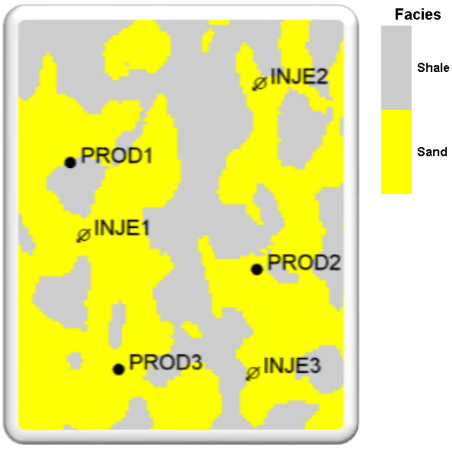

(b) 1st Facies realization

Figure 4-23 Calibrated facies models versus true model ($w = 0.7$).

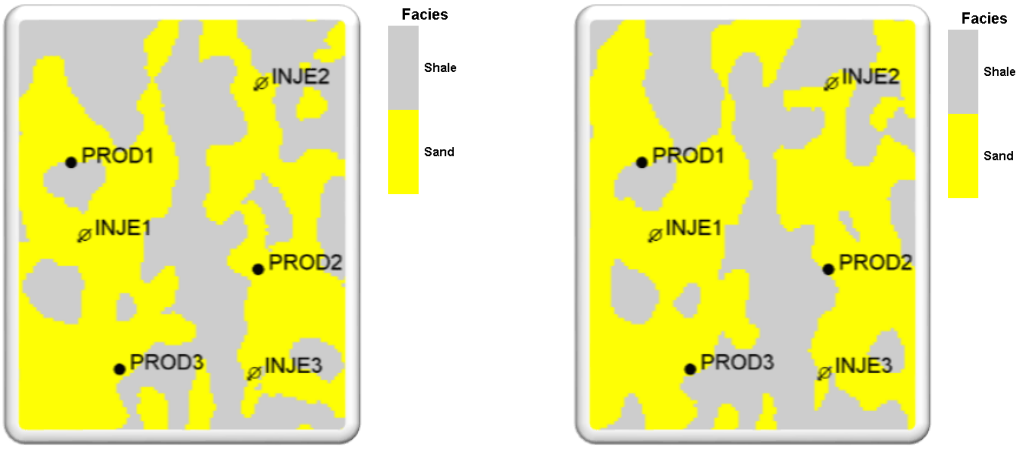

(c) 2nd Facies realization **(d) 3rd Facies realization**

Figure 4.23 continued.

On the basis of the updated facies models, the property model calibration is conducted as follows. Taking 0.2 as the reference acceptance rate for comparison convenience purpose (Figure 4-24), with the increase of seismic weight, the acceptance rate of three MCMC chains increases. Similarly, taking 200 as the reference data misfit, the data misfit displays a lower trend with more weight of seismic constraint. That is because the seismic helps to guide facies variation to the true facies distribution, which establishes an important basis for property modelling. The high and low permeability regions within the channel are clearly depicted (Figure 4-26, Figure 4-27 and Figure 4-28). As mentioned above, the choice of seismic weight is subjective based on the quality of seismic data, and the prior knowledge on the geological evaluation. In our case, 0.7 is the optimal selection compared with 0 and 0.5, but it does not mean that the larger the seismic weight is, the better results we can get in other applications. Oil rate, water cut, producer BHP, and water injection rate are matched very well for all the wells when w is equal to 0.7 (Figure 4-29).

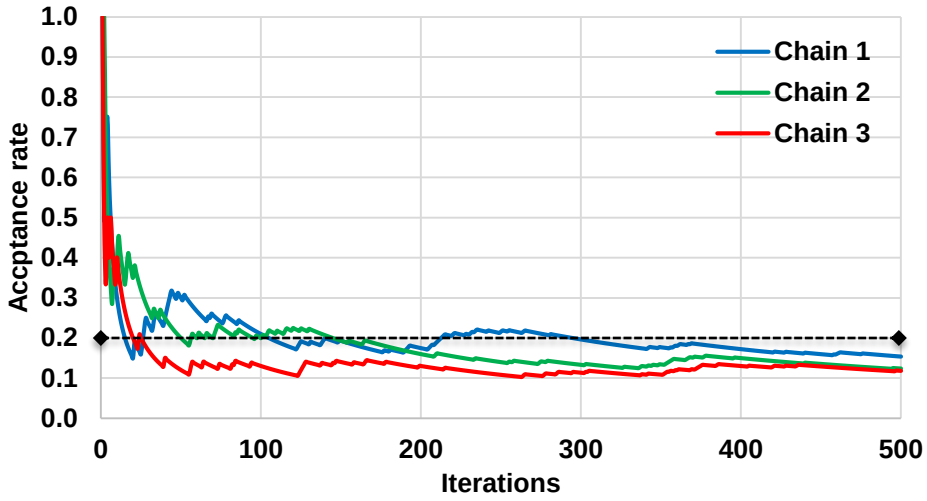

(a) Acceptance rate versus number of iterations for Markov chain ($w = 0$).

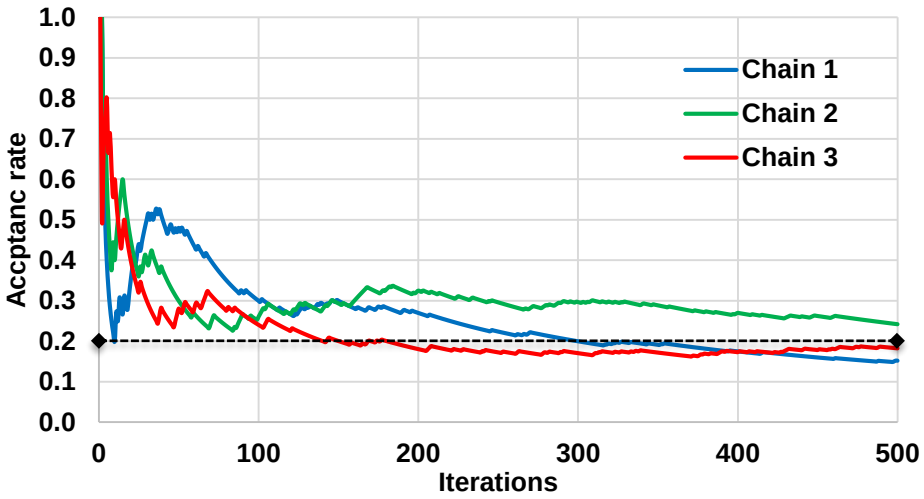

(b) Acceptance rate versus number of iterations for Markov chain ($w = 0.5$).

Figure 4-24 Acceptance rate versus number of iterations for different w.

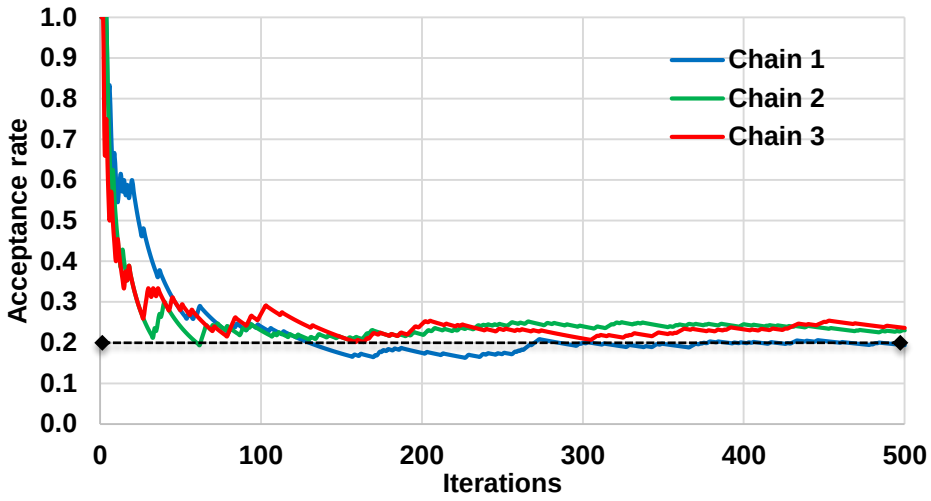

(c) Acceptance rate versus number of iterations for Markov chain ($w = 0.7$).

Figure 4.24 continued.

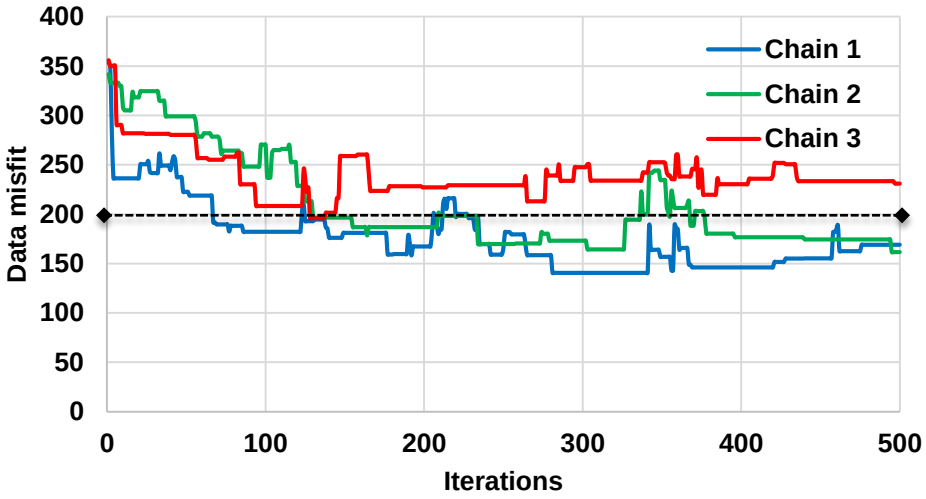

(a) Data misfit versus number of iterations for Markov chain ($w = 0$).

Figure 4-25 Data misfit versus number of iterations for different w.

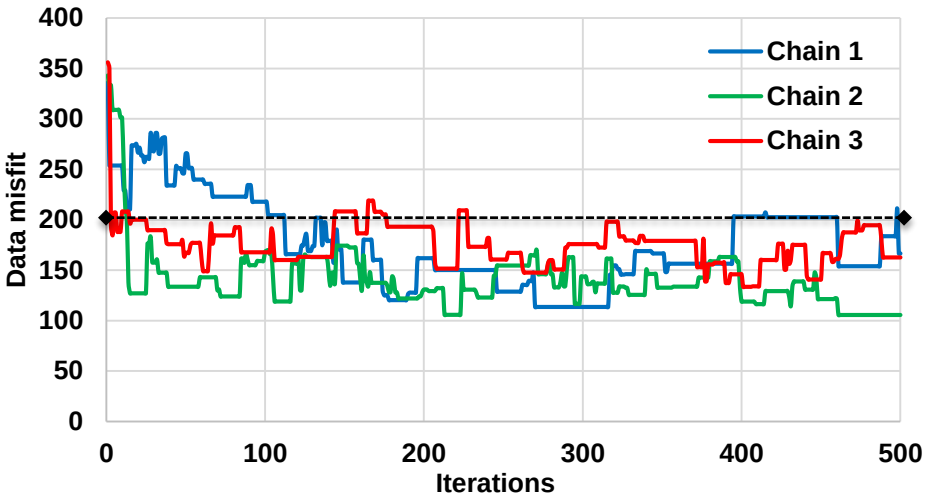

(b) Data misfit versus number of iterations for Markov chain ($w = 0.5$).

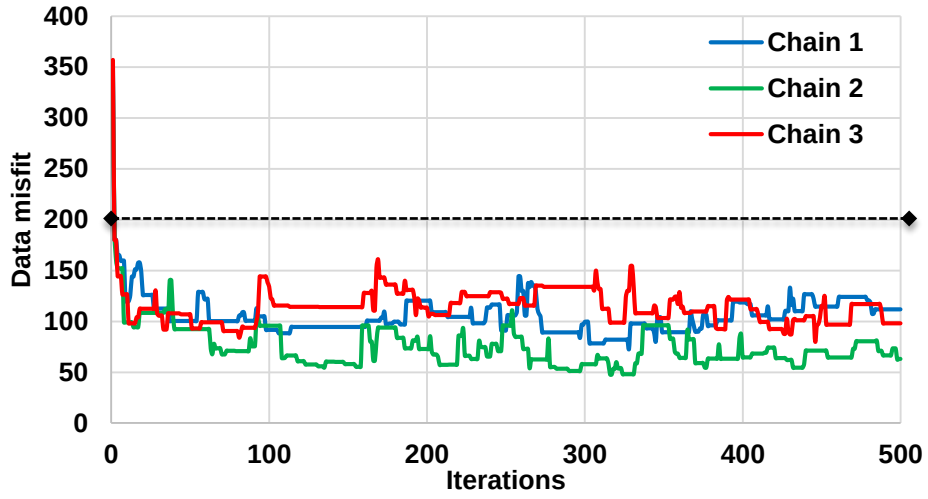

(c) Data misfit versus number of iterations for Markov chain ($w = 0.7$).

Figure 4.25 continued.

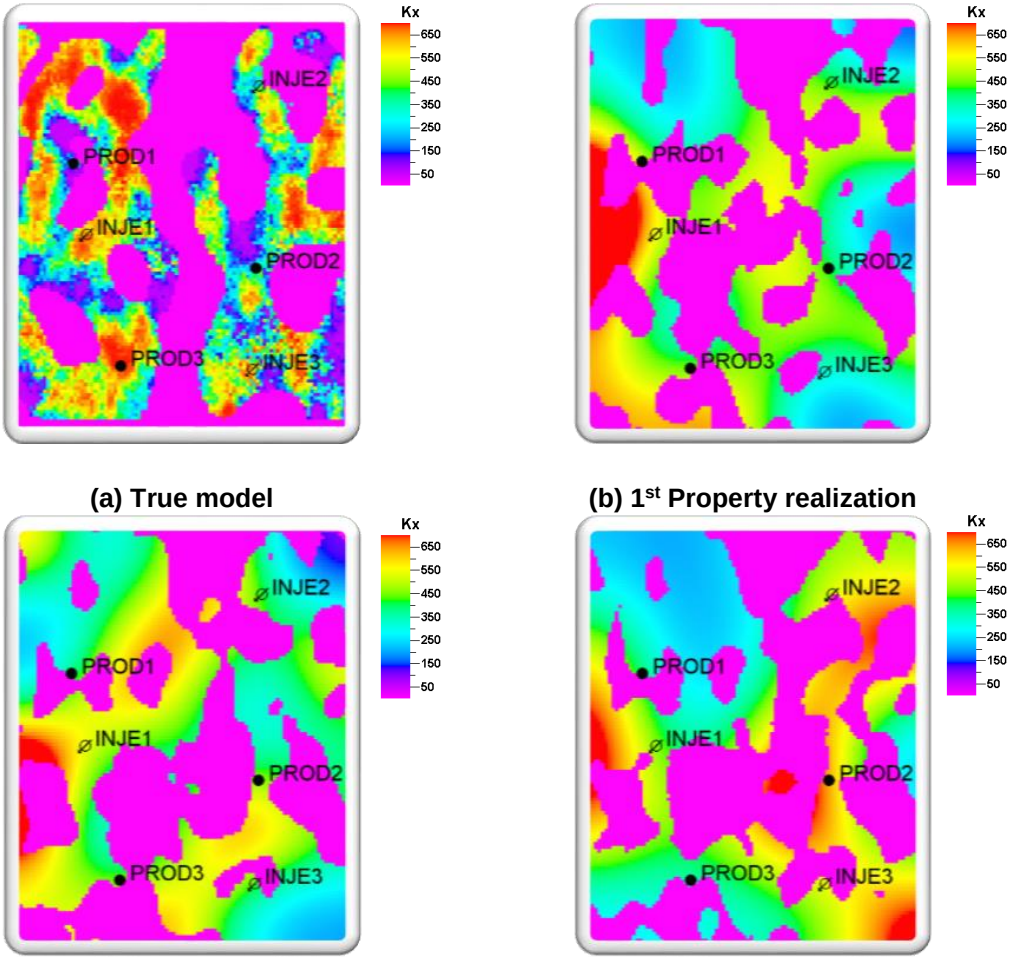

(a) True model

(b) 1st Property realization

(c) 2nd Property realization

(d) 3rd Property realization

Figure 4-26 Calibrated property models versus true model ($w = 0$).

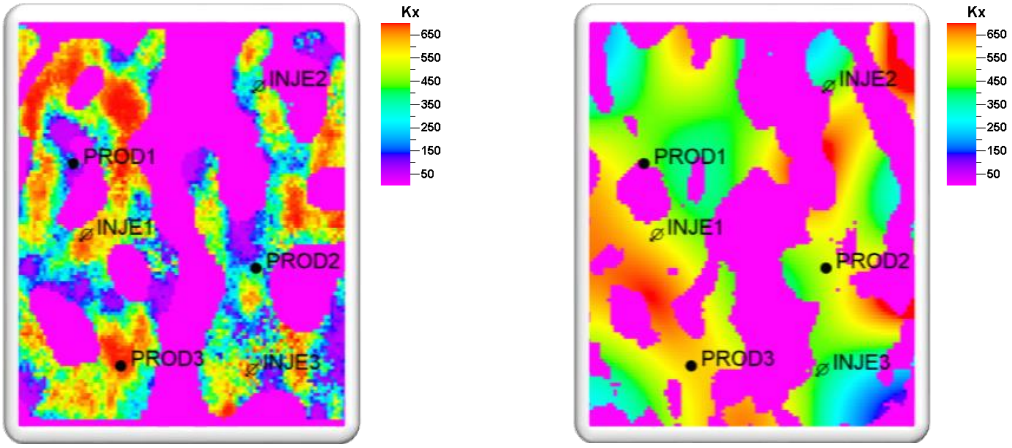

(a) True model

(b) 1st Property realization

(c) 2nd Property realization

(d) 3rd Property realization

Figure 4-27 Calibrated property models versus true model ($w = 0.5$).

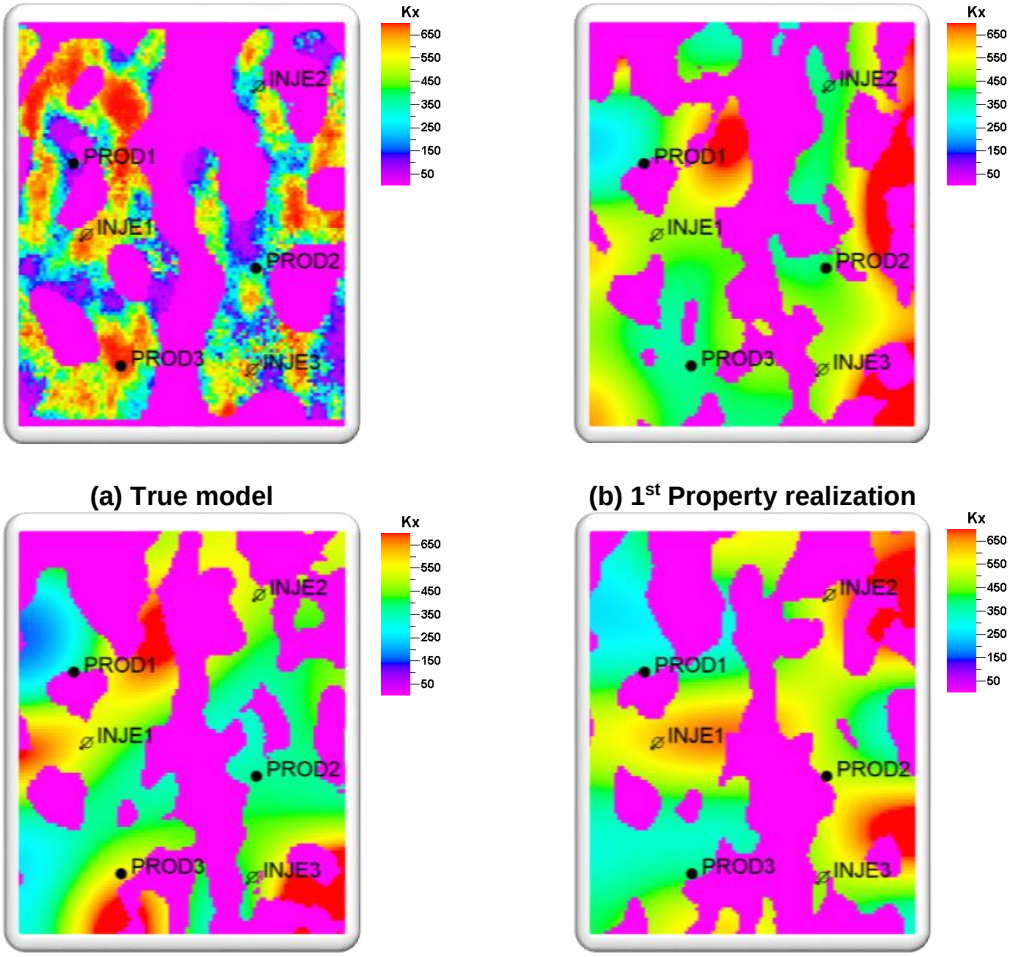

(a) True model

(b) 1st Property realization

(c) 2nd Property realization

(d) 3rd Property realization

Figure 4-28 Calibrated property models versus true model ($w = 0.7$).

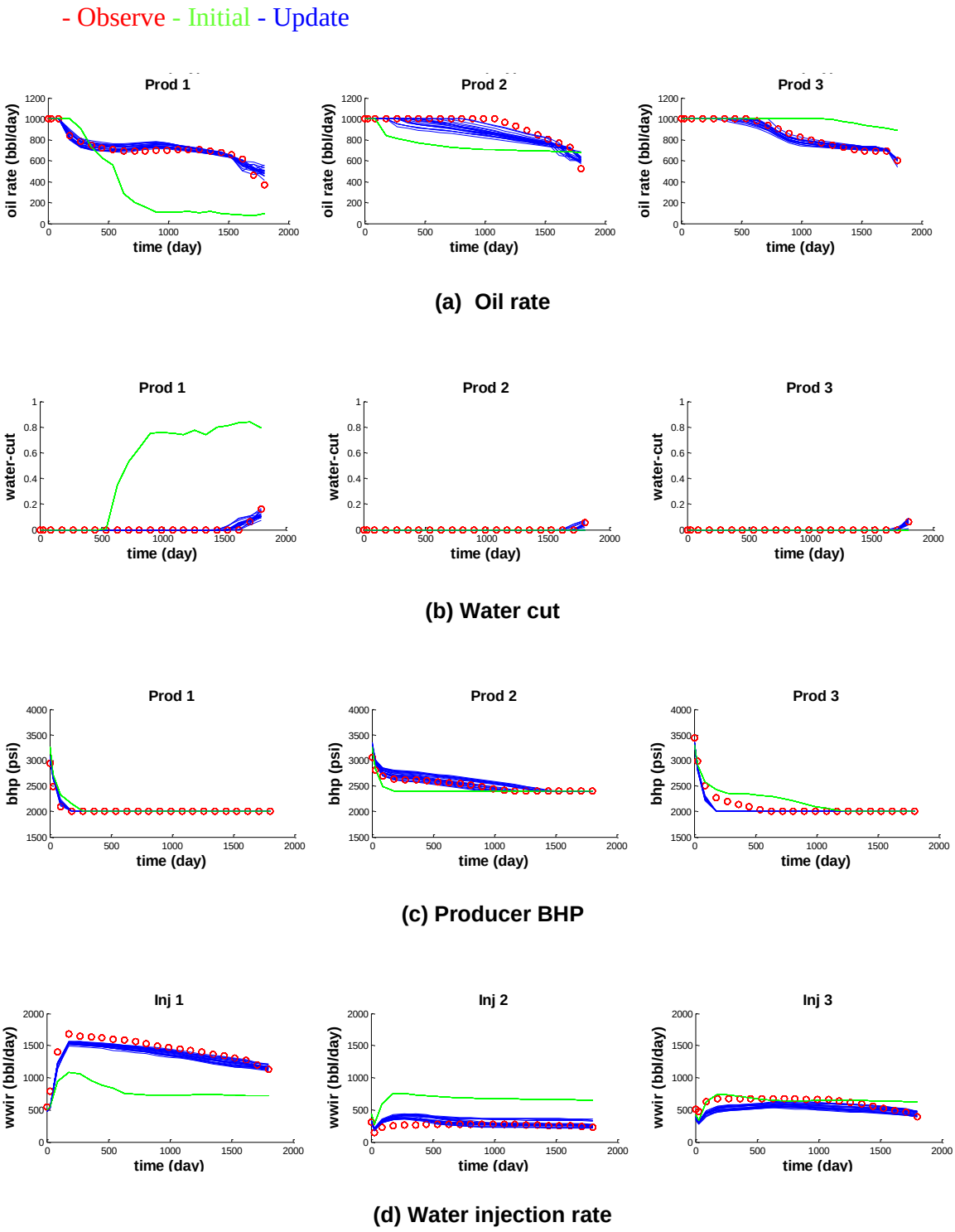

Figure 4-29 History matching results: (a) oil rate, (b) water cut, (c) producer BHP, (d) water injection rate.

4.5 Summary

In this chapter, we compared different parameterization methods and their performance in the image reconstruction and history matching, and then proposed a two-step history matching workflow for the channelized reservoir facies model calibration using the level set and property calibration within the channel using the GCT. The main findings are summarized as follows:

1. In the image reconstruction part, the DCT performs better with less coefficients, while the DWT surpass the other methods with more coefficients involved. The GCT behaves smoothly compared with the other two.
2. All the reparameterization methods studied here (the DCT, GCT, and DWT) do not seem to be able to reproduce the channel geometry during the history matching without the help of the level set.
3. The level set method provides an excellent framework for reparameterizing facies boundaries during history matching by changing channel geometry and connectivity. The main channel feature can be captured, and final history matching results perform better in comparison with directly applying parametrization methods on the reservoir.
4. For complicated channelized reservoirs, if seismic information is available, it can be effectively incorporated into the level set method to improve facies model calibration further. That's because generally seismic can provide accurate channel distribution pattern, which is the direction where the facies model can evolve toward.

CHAPTER V

CONCLUSIONS AND RECOMMENDATIONS

5.1 Conclusions

In this dissertation, we presented two applications of the Pareto-based method and the level set method in reservoir characterization: multiobjective optimization framework in the model ranking, history matching, and optimization as well as facies and property calibration for the channelized reservoir.

First, we have presented the Pareto-based model ranking (PBMR) approach for multiple geologic models with multiscale data, such as seismic and production data.

Second, we have applied a hierarchical history matching workflow, followed by a two-step polymer flood optimization for the Norne Field. The history matching workflow includes the global and local updates, and production optimization consists of the streamline-based rate optimization for waterflood and the Pareto-based polymer flood optimization. The Pareto-based framework is utilized not only in the history matching, but also in the production optimization process.

Third, a two-step history matching workflow is proposed where the channel geometry is modeled using the level set with/without seismic constraint, and internal scale heterogeneity is modeled using the GCT.

The main findings in this work are summarized below:

1. The Pareto-based framework is easily integrated into the model ranking, history matching, and production optimization processes. It has been proved to be

powerful method to integrate different scales of data and characterize the complementary as well as conflicting features of multiobjective, especially for the seismic and production data. The optimal Pareto front consisting of highly ranked models provides optimal choices in mathematics, which gives petroleum engineers a strong flexibility to make decision considering the model uncertainties.

2. The proposed Pareto-based model ranking approach can effectively incorporate accurate and comprehensive model set solution: the conflicting characteristic of multiple objectives can be preserved, selected models are competitive, and uncertainty range can be effectively addressed for each objective. In contrast, the weighted-sum method may lose some plausible solutions, and include more uncompetitive solutions simultaneously.
3. The Norne Field history matching application showed substantial improvement in matching acoustic impedance changes and also well by well water cut data matching after the global and fine scale updates. Seismic and production data are simultaneously integrated in the global updates. Moreover, the pressure and saturation effects on acoustic impedance changes are integrated sequentially in the local updates.
4. The Norne Field production application demonstrated the feasibility of the two-step polymer flood optimization for improving sweep efficiency by coupling the streamline-based rate optimization and the Pareto-based polymer optimization. The Rate optimization provides favorable production/injection rates for the polymer optimization, and the optimal solution, compromising production

improvement and utility factor, is successfully found from the average Pareto front. The cumulative production and NPV are improved substantially after production optimization.

5. Our observation shows that the traditional parameterization methods (the DCT, GCT, and DWT) cannot calibrate the channelized reservoirs directly. However, the two-step history matching workflow can effectively update the channel boundaries, and characterize the high/low permeability region within the channel. What's more important is that the integration of seismic data into the level set provides the potential extension from synthetic model to more complicated field channelized reservoirs.

5.2 Recommendations

Although the methods and workflow proposed here work well, there are still many places that need to be improved further. The recommendations are summarized as follows:

1. In the Pareto-based model ranking, although lower rank level models are competitive than the higher ones, sometimes the difference is very small between different rank levels. It is more reasonable to classify the rank level models with small differences together. Thus, the tolerance needs to be considered when we assign rank levels. If the difference is within the tolerance, the models, which belong to different levels mathematically, should be assigned to the same rank level from engineering point of view. In other words, the distance measurement between multiple rank levels may help improve the PBMR performance.

2. In the Norne Field production optimization, we implemented the rate optimization and polymer optimization sequentially. However, after injecting the polymer, the pressure and velocity field will change, and the production and injection rates needs to be re-optimized through streamline-based approach for the current reservoir conditions. It means that the better results can be obtained if we optimize production and injection rates after the optimization of each polymer simulation time step. The more accurate results are at the cost of simulation speed, because we need apply multiple rate optimization in the polymer optimization. Thus, it is a challenge to balance the speed and accuracy.
3. For the channelized reservoir, the seismic is incorporated into the level set in the very first step to modify the initial model before entering optimization iterations. If the MCMC includes the seismic derived information in each iteration, the level set method can be applied into more complicated and larger field models.
4. Currently, the seismic weight is a subjective variable, which needs to be decided by reservoir engineer, geologist, and geophysicist together. The establishment of relationship (equation or interpolation table) between seismic weight and some given reservoir parameters should benefit for the quick determination of seismic weight. Also, the seismic weight can be expressed as a function of location or facies type, which helps to build more accurate relationship between initial SDF and AI SDF.

NOMENCLATURE

AI	=	Acoustic Impedance
BHP	=	Bottom-hole Pressure
DCT	=	Discrete Cosine Transform
DWT	=	Discrete Wavelet Transform
GRF	=	Gaussian Random Field
FBHP	=	Field Bottom-hole Pressure
FGPT	=	Field Cumulative Gas Production
FMM	=	Fast Marching Method
FWCT	=	Field Water Cut
FWPT	=	Field Cumulative Water Production
GCT	=	Grid Connectivity Transform
GTTI	=	Generalized Travel Time Inversion
HCPV	=	Hydrocarbon Pore Volume
HM	=	History Matching
LHS	=	Latin Hypercube Sampling
MCMC	=	Markov Chain Monte Carlo
MOEA	=	Multi-objective Optimization Evolutionary Algorithm
MOPSO	=	Multi-objective Particle Swarm Optimization
MSE	=	Mean Square Error
NPV	=	Net Present Value
PBMR	=	Pareto-based Model Ranking
PEM	=	Petro-elastic Model
RI	=	Resistivity Index
RMSE	=	Root Mean Square Error
RRF	=	Residual Resistance Factor

SDF	=	Signed Distance Function
SGSIM	=	Sequential Gaussian Simulation
SQP	=	Sequential Quadratic Programming
SIS	=	Sequential Indicator Simulation
SW DIFF	=	Seismic Saturation Difference
TVD	=	True Vertical Depth
UF	=	Utility Factor
WWCT	=	Well Water Cut

E_v	=	Volumetric sweep efficiency
w	=	Data misfit weights
f	=	Objective function
τ	=	Time of flight
ψ	=	Streamline trajectory
s	=	Slowness
S	=	Saturation
$\vec{v}$	=	Interstitial velocity
λ	=	Mobility
k	=	Permeability
ϕ	=	Porosity
t	=	Time
S_w	=	Water saturation
F_w	=	Fractional flow of water
P	=	Hydrostatic pressure
P_{eff}	=	Effective pressure
P_{ext}	=	Lithostatic pressure
ΔP	=	Pressure drop along streamlines

δm	=	Model parameter change
K_{HM}	=	Bulk modulus of the Hertz-Mindlin formula
K_{ma}	=	Bulk modulus of the matrix
K_{fr}	=	Bulk modulus of the porous rock frame
K_f	=	Bulk modulus of the pore-filling fluids
K_{sat}	=	Bulk modulus of the fluid saturated rock
ρ_{sat}	=	Density of the fluid saturated rock
ρ_{ma}	=	Density of rock matrix
G_{fr}	=	Shear modulus of the porous rock frame
V_p	=	P-wave velocity
V_s	=	S-wave velocity
Z_p	=	Acoustic (p-wave) impedance
u	=	Property vector
Φ	=	Basis matrix
v	=	Coefficient vector
A	=	Cross sectional area
q	=	Flow rate
$t_{i,m}$	=	Arrival time of well i in group m
$t_{d,m}$	=	Average arrival time for group m
η	=	Weight trade-off between equalizing arrival time and production acceleration
$N_{fsl,i}$	=	Number of fast streamlines connected to the producer i
$N_{prod,m}$	=	Number of producers in group m
$\tau_{l,i}$	=	Time of flight of streamline l connected to the producer i
ΔN_p	=	Cumulative oil gain
R_k	=	Permeability reduction factor
C_p	=	Polymer concentration

C_p^{amax}	=	Maximum absorbed polymer concentration
C_p^a	=	Absorbed polymer concentration
μ_w	=	Water viscosity
$\mu_{w,e}$	=	Partially mixed water viscosity
ω	=	Todd-Longstaff mixing parameter
α	=	Scaling coefficient
β	=	Wavelet coefficient
ϕ_j	=	Scaling function at scale level *j*
ψ_j	=	Wavelet function at scale level j
Γ	=	Closed curve
φ	=	Implicit surface function
φ_d	=	Signed distance function
$\varphi_d^{t_0'}$	=	Initial signed distance function
$\varphi_d^{t_0}$	=	Deformed signed distance function
φ_{AI}	=	AI signed distance function
v_n	=	Normal velocity

REFERENCES

Agbalaka, C.C. and Oliver, D. 2011. Joint Updating of Petrophysical Properties and Discrete Facies Variables from Assimilating Production Data Using the Enkf. *SPE Journal* **16** (02): 318 - 330. DOI: 10.2118/118916-PA.

Aki, K. and Richards, P.G. 1980. *Quantitative Seismology*: Freeman San Francisco. Original edition. ISBN 0716710587.

Al-Sofi, A.M. and Blunt, M.J. 2011. The Design and Optimization of Polymer Flooding under Uncertainty. Paper presented at the SPE Enhanced Oil Recovery Conference, Kuala Lumpur, Malaysia. Society of Petroleum Engineers SPE-145110-MS. DOI: 10.2118/145110-MS.

Alabert, F.G. and Modot, V. 1992. Stochastic Models of Reservoir Heterogeneity: Impact on Connectivity and Average Permeabilities. Paper presented at the SPE Annual Technical Conference and Exhibition, Washington, D.C. 1992 Copyright 1992, Society of Petroleum Engineers Inc. 00024893. DOI: 10.2118/24893-MS.

Alhuthali, A., Oyerinde, A., and Datta-Gupta, A. 2007. Optimal Waterflood Management Using Rate Control. *SPE Journal* **10** (05): 539 - 551. DOI: 10.2118/102478-PA.

Awotunde, A.A. and Horne, R.N. 2010. Multidimensional Reservoir Description and Data Integration Using Time-Space Wavelet Analysis. Paper presented at the SPE Annual Technical Conference and Exhibition, Florence, Italy. Society of Petroleum Engineers SPE-133869-MS. DOI: 10.2118/133869-MS.

Batzle, M. and Wang, Z. 1992. Seismic Properties of Pore Fluids *GEOPHYSICS* **57** (11): 1396-1408. DOI: 10.1190/1.1443207.

Bhark, E., Jafarpour, B., and Datta-Gupta, A. 2011a. An Adaptively Scaled Frequency-Domain Parameterization for History Matching. *Journal of Petroleum Science and Engineering* **75** (3–4): 289-303.

Bhark, E., Jafarpour, B., and Datta-Gupta, A. 2011b. A Generalized Grid Connectivity–Based Parameterization for Subsurface Flow Model Calibration. *Water Resources Research* **47** (6): W06517. DOI: 10.1029/2010WR009982.

Bhark, E., Rey, A., Datta-Gupta, A. et al. 2012. A Multiscale Workflow for History Matching in Structured and Unstructured Grid Geometries. *SPE Journal* **17** (3): 828 - 848. DOI: 10.2118/141764-PA.

Bhark, E., Datta-Gupta, A., and Jafarpour, B. 2011. History Matching with a Multiscale Parameterization Based on Grid Connectivity and Adaptive to Prior Information. Paper presented at the SPE Annual Technical Conference and Exhibition, Denver, Colorado, USA. Society of Petroleum Engineers SPE-147372-MS. DOI: 10.2118/147372-MS.

Cheng, H., Dehghani, K., and Billiter, T.C. 2008. A Structured Approach for Probabilistic-Assisted History Matching Using Evolutionary Algorithms: Tengiz Field Applications. Paper presented at the SPE Annual Technical Conference and Exhibition, Denver, Colorado, USA. Society of Petroleum Engineers SPE-116212-MS. DOI: 10.2118/116212-MS.

Cheng, H., Kharghoria, A., He, Z. et al. 2005. Fast History Matching of Finite-Difference Models Using Streamline-Based Sensitivities. *SPE Reservoir Evaluation & Engineering* **8** (05): 426 - 436. DOI: 10.2118/89447-PA.

Christensen, N.I. and Wang, H.F. 1985. The Influence of Pore Pressure and Confining Pressure on Dynamic Elastic Properties of Berea Sandstone. *Geophysics* **50** (2): 207-213. DOI: 10.1190/1.1441910.

Clemens, T., Abdev, J., and Thiele, M. 2011. Improved Polymer-Flood Management Using Streamlines. *SPE Reservoir Evaluation & Engineering* **14** (02): 171 - 181. DOI: 10.2118/132774-PA.

Dadashpour, M., Echeverr´ıa-Ciaurri, D., Kleppe, J. et al. 2009. Porosity and Permeability Estimation by Integration of Production and Time-Lapse near and Far Offset Seismic Data. *Journal of Geophysics and Engineering* **6** (4): 325-344. DOI: 10.1088/1742-2132/6/4/001.

Datta-Gupta, A. and King, M.J. 2007. *Streamline Simulation: Theory and Practice*: Society of Petroleum Engineers. Original edition. ISBN 978-1-55563-111-6.

Deb, K., Pratap, A., Agarwal, S. et al. 2002. A Fast and Elitist Multiobjective Genetic Algorithm: Nsga-Ii. *Evolutionary Computation, IEEE Transactions on* **6** (2): 182-197.

Denney, D. 2012. Stochastic Data Integration: History Matching Production and Time-Lapse-Seismic Data. *Journal of Petroleum Technology* **64** (04): 137 - 139. DOI: 10.2118/0412-0137-JPT.

Deutsch, C.V. and Wang, L. 1996. Hierarchical Object-Based Stochastic Modeling of Fluvial Reservoirs. *Mathematical Geology* **28** (7): 857-880. DOI: 10.1007/bf02066005.

Elphick, R.Y. and Moore, W.R. 1999. Permeability Calculations from Clustered Electrofacies, a Case Study in Lake Maracaibo, Venezuela. Society of Petrophysicists & Well Log Analysts SPWLA-1999-AA.

Gao, G. and Reynolds, A.C. 2006. An Improved Implementation of the Lbfgs Algorithm for Automatic History Matching. *SPE Journal* **11** (01). DOI: 10.2118/90058-PA.

Gassmann, F. 1951. Elastic Waves through a Packing of Spheres. *GEOPHYSICS* **16** (4): 673-685. DOI: 10.1190/1.1437718.

Gonzalez, R.C. and Woods, R.E. 2002. *Digital Image Processing* Prentice Hall. 2nd edition. ISBN 0201180758.

Hastings, W.K. 1970. Monte Carlo Sampling Methods Using Markov Chains and Their Applications. *Biometrika* **57** (1): 97-109. DOI: 10.2307/2334940.

He, Z., Yoon, S., and Datta-Gupta, A. 2002. Streamline-Based Production Data Integration with Gravity and Changing Field Conditions. *SPE Journal* **7** (04): 423 - 436. DOI: 10.2118/81208-PA.

Hird, K. and Dubrule, O. 1998. Quantification of Reservoir Connectivity for Reservoir Description Applications. *SPE Reservoir Evaluation & Engineering* **1** (1): 12-17.

Hirsch, L. and Schuette, J. 1999. Graph Theory Applications to Continuity and Ranking in Geologic Models. *Computers & Geosciences* **25** (2): 127-139.

Holland, J.H. 1992. Genetic Algorithms. *Scientific American* **267** (1): 44-50.

Hu, L.Y., Ravalec, M.L., Blanc, G. et al. 1999. Reducing Uncertainties in Production Forecasts by Constraining Geological Modeling to Dynamic Data. Paper presented at the SPE Annual Technical Conference and Exhibition, Houston, Texas. Copyright 1999, Society of Petroleum Engineers Inc. 00056703. DOI: 10.2118/56703-MS.

Idrobo, E.A., Choudhary, M.K., and Datta-Gupta, A. 2000. Swept Volume Calculations and Ranking of Geostatistical Reservoir Models Using Streamline Simulation. Paper presented at the SPE/AAPG Western Regional Meeting, Long Beach, California. Copyright 2000, Society of Petroleum Engineers Inc. 00062557. DOI: 10.2118/62557-MS.

Jafarpour, B. 2011. Wavelet Reconstruction of Geologic Facies from Nonlinear Dynamic Flow Measurements. *IEEE Transactions on Geoscience and Remote Sensing Society* **49** (5): 1520 - 1535. DOI: 10.1109/TGRS.2010.2089464.

Jafarpour, B., Goyal, V.K., McLaughlin, D.B. et al. 2009a. Compressed History Matching: Exploiting Transform-Domain Sparsity for Regularization Of nonlinear Dynamic Data Integration Problems. *Mathematical Geosciences* **42** (1): 1-27. DOI: 10.1007/s11004-009-9247-z

Jafarpour, B., Goyal, V.K., McLaughlin, D.B. et al. 2009b. Transform-Domain Sparsity Regularization for Inverse Problems in Geosciences. *GEOPHYSICS* **74** (5): R69-R83. DOI: 10.1190/1.3157250.

Jafarpour, B. and McLaughlin, D.B. 2009. Reservoir Characterization with the Discrete Cosine Transform. *SPE Journal* **14** (01): 182 - 201. DOI: 10.2118/106453-PA.

Johnson Jr, C. 1956. Prediction of Oil Recovery by Waterflood-a Simplified Graphical Treatment of the Dykstra-Parsons Method. *Journal of Petroleum Technology* **8** (11): 55-56.

Journel, A.G. 1990. Geostatistics for Reservoir Characterization. Paper presented at the SPE Annual Technical Conference and Exhibition, New Orleans, Louisiana. 1990 Copyright 1990, Society of Petroleum Engineers Inc. 00020750. DOI: 10.2118/20750-MS.

Kam, D. and Datta-Gupta, A. 2014. Streamline-Based Transport Tomography Using Novel Tracer Technologies. Paper presented at the SPE Improved Oil Recovery Symposium, Tulsa, Oklahoma, USA. Society of Petroleum Engineers SPE-169105-MS. DOI: 10.2118/169105-MS.

Kang, S., Bhark, E., Datta-Gupta, A. et al. 2014. A Hierarchical Model Calibration Approach with Multiscale Spectral-Domain Parameterization: Application to a Structurally Complex Fractured Reservoir. Paper presented at the SPE Improved Oil Recovery Symposium, Tulsa, Oklahoma, USA. Society of Petroleum Engineers SPE-169061-MS. DOI: 10.2118/169061-MS.

Kennet, B. 1983. *Seismic Wave Propagation in Stratified Media*: Cambridge University Press Original edition. ISBN 0521239338.

Kim, C.S. and Dobin, M.W. 2008. A Rapid Method for Reservoir Connectivity Analysis Using a Fast Marching Method. In: EP Patent 1,883,840.

Kind, M.V. and Quinteros, J. 2007. History-Matched Reservoir Model Validation Based on Wavelets Methods. Paper presented at the Latin American & Caribbean

Petroleum Engineering Conference, Buenos Aires, Argentina. Society of Petroleum Engineers SPE-108124-MS. DOI: 10.2118/108124-MS.

Koltermann, C.E. and Gorelick, S.M. 1996. Heterogeneity in Sedimentary Deposits: A Review of Structure-Imitating, Process-Imitating, and Descriptive Approaches. *Water Resources Research* **32** (9): 2617-2658. DOI: 10.1029/96WR00025.

L.N.Y.Wong and G.Liu. 2010. An Improved K-Means Clustering Method for the Automatic Grouping of Discontinuity Sets. American Rock Mechanics Association ARMA-10-265.

Li, H. and Zhang, Q. 2009. Multiobjective Optimization Problems with Complicated Pareto Sets, Moea/D and Nsga-Ii. *Evolutionary Computation, IEEE Transactions on* **13** (2): 284-302.

Lorentzen, R.J., Nævdal, G., and Shafieirad, A. 2012. Estimating Facies Fields by Use of the Ensemble Kalman Filter and Distance Functions--Applied to Shallow-Marine Environments. *SPE Journal* **3** (01): 146 - 158. DOI: 10.2118/143031-PA.

Mao, S. and Journel, A.G. 1999. *Generation of a Reference Petrophysical/Seismic Data Set: The Stanford V Reservoir.*: Stanford Center for Reservoir Forecasting (SCRF) Report No. 12.

Mavko, G., Mukerji, T., and Dvorkin, J. 1998. *The Rock Physics Handbook: Tools for Seismic Analysis in Porous Media*: Cambridge University Press. Original edition. ISBN 0521620686.

McCormick, G.P. and Tapia, R.A. 1972. The Gradient Projection Method under Mild Differentiability Conditions. *SIAM Journal on Control* **10** (1): 93-98. DOI: 10.1137/0310009.

Mindlin, R.D. 1949. Compliance of Elastic Bodies in Contact. *Journal of Applied Mechanics* **16**: 259-268.

Mishra, S., Choudhary, M.K., and Datta-Gupta, A. 2000. A Novel Approach for Reservoir Forecasting under Uncertainty. Paper presented at the SPE Annual Technical Conference and Exhibition, Dallas, Texas. Copyright 2000, Society of Petroleum Engineers Inc. 00062926. DOI: 10.2118/62926-MS.

Mistry, D. and Banerjee, A. 2013. Discrete Wavelet Transform Using Matlab. *International journal of Computer Engineering & Technology* **4** (2): 252-259.

Mohamed, L., Christie, M.A., and Demyanov, V. 2011. History Matching and Uncertainty Quantification: Multiobjective Particle Swarm Optimisation Approach. Paper presented at the SPE EUROPEC/EAGE Annual Conference and Exhibition, Vienna, Austria. Society of Petroleum Engineers SPE-143067-MS. DOI: 10.2118/143067-MS.

Mohsen, D., David, E.-C., Jon, K. et al. 2009. Porosity and Permeability Estimation by Integration of Production and Time-Lapse near and Far Offset Seismic Data. *Journal of Geophysics and Engineering* **6** (4): 325-344. DOI: 10.1088/1742-2132/6/4/001.

Mohsen, D., David Echeverria, C., Tapan, M. et al. 2010. A Derivative-Free Approach for the Estimation of Porosity and Permeability Using Time-Lapse Seismic and

Production Data. *Journal of Geophysics and Engineering* **7** (4): 351-368. DOI: 10.1088/1742-2132/7/4/002.

Odai, L. and Ogbe, D.O. 2011. An Approach for Ranking Realizations to Characterize Reservoirs for Fluid Flow Simulation. Paper presented at the Nigeria Annual International Conference and Exhibition, Abuja, Nigeria. Society of Petroleum Engineers SPE-150738-MS. DOI: 10.2118/150738-MS.

Olalotiti-Lawal, F. and Datta-Gupta, A. 2015. A Multi-Objective Markov Chain Monte Carlo Approach for History Matching and Uncertainty Quantification. Paper presented at the SPE Annual Technical Conference and Exhibition, Houston, Texas, USA. Society of Petroleum Engineers SPE-175144-MS. DOI: 10.2118/175144-MS.

Osdal, B., Husby, O., Aronsen, H.A. et al. 2006. Mapping the Fluid Front and Pressure Buildup Using 4d Data on Norne Field. *The Leading Edge* **25** (9): 1134-1141.

Osher, S. and Fedkiw, R. 2002. *Level Set Methods and Dynamic Implicit Surfaces: Spinger* Original edition. ISBN 978-0-387-22746-7.

Osher, S. and Sethian, J.A. 1988. Front Propagating with Curvature Dependent Speed: Algorithms Based on Hamilton-Jacobi Formulations. *Journal of Computational Physics* **79** (1): 12 - 49.

Osher, S.J. and Santosa, F. 2001. Level Set Methods for Optimization Problems Involving Geometry and Constraints I. Frequencies of a Two-Density Inhomogeneous Drum. *Journal of Computational Physics* **171** (1): 272 - 288.

Park, H.-Y., Datta-Gupta, A., and King, M. 2013. Handling Conflicting Multiple Objectives Using Pareto-Based Evolutionary Algorithm for History Matching of Reservoir Performance. Paper presented at the 2013 SPE Reservoir Simulation Symposium, The Woodlands, TX, USA. Society of Petroleum Engineers SPE-163623-MS. DOI: 10.2118/163623-MS.

Peters, L., Arts, R., Brouwer, G. et al. 2009. Results of the Brugge Benchmark Study for Flooding Optimisation and History Matching. Paper presented at the SPE Reservoir Simulation Symposium, The Woodlands, Texas. Society of Petroleum Engineers SPE-119094-MS. DOI: 10.2118/119094-MS.

Ping, J. and Zhang, D. 2014. History Matching of Channelized Reservoirs with Vector-Based Level-Set Parameterization. *SPE Journal* **19** (03): 514 - 529. DOI: 10.2118/169898-PA

Remy, N., Boucher, A., and Wu, J. 2009. *Applied Geostatistics with Sgems: A User's Guide: Cambridge University* Original edition. ISBN 9780521514149.

Reuss, A.Z. 1929. Berechnung Der Fließgrenze Von Mischkristallen Auf Grund Der Plastizitätsbedingung Für Einkristalle. *ZAMM ‐ Journal of Applied Mathematics and Mechanics/Zeitschrift für Angewandte Mathematik und Mechanik* **9** (1): 49-58. DOI: 10.1002/zamm.19290090104.

Rey, A., Bhark, E., Gao, K. et al. 2012. Streamline-Based Integration of Time-Lapse Seismic and Production Data into Petroleum Reservoir Models. *GEOPHYSICS* **77** (6): M73-M87. DOI: 10.1190/geo2011-0346.1.

Rwechungura, R.W., Bhark, E.W., Miljeteig, O.T. et al. 2012. Results of the First Norne Field Case on History Matching and Recovery Optimization Using Production and

4d Seismic Data. Paper presented at the SPE Annual Technical Conference and Exhibition, San Antonio, Texas, USA. Society of Petroleum Engineers SPE-157112-MS. DOI: 10.2118/157112-MS.

Saad, N., Maroongroge, V., and Kalkomey, C.T. 1996. Ranking Geostatistical Models Using Tracer Production Data. Paper presented at the European 3-D Reservoir Modelling Conference, Stavanger, Norway. 1996 Copyright 1996, Society of Petroleum Engineers, Inc. 00035494. DOI: 10.2118/35494-MS.

Sahni, I. and Horne, R.N. 2005. Multiresolution Wavelet Analysis for Improved Reservoir Description. *SPE Reservoir Evaluation & Engineering* **8** (01): 53 - 69. DOI: 10.2118/87820-PA.

Sahni, I. and Horne, R.N. 2006a. Generating Multiple History-Matched Reservoir-Model Realizations Using Wavelets. *SPE Reservoir Evaluation & Engineering* **9** (03): 217 - 226. DOI: 10.2118/89950-PA.

Sahni, I. and Horne, R.N. 2006b. Stochastic History Matching and Data Integration for Complex Reservoirs Using a Wavelet-Based Algorithm. Paper presented at the SPE Annual Technical Conference and Exhibition, San Antonio, Texas, USA. Society of Petroleum Engineers SPE-103107-MS. DOI: 10.2118/103107-MS.

Schlumberger. 2012. Eclipse Reservoir Simulation Software Reference Manual, 2012.2, United States.

Shook, G.M. and Mitchell, K.M. 2009. A Robust Measure of Heterogeneity for Ranking Earth Models: The F-Phi Curve and Dynamic Lorenz Coefficient. Paper presented at the SPE Annual Technical Conference and Exhibition, New Orleans, Louisiana. Society of Petroleum Engineers SPE-124625-MS. DOI: 10.2118/124625-MS.

Srinivas, N. and Deb, K. 1994. Muiltiobjective Optimization Using Nondominated Sorting in Genetic Algorithms. *Evolutionary computation* **2** (3): 221-248.

Steffensen, I. and Karstadt, P.I. 1996. Norne Field Development - Fast Track from Discovery to Production. *Journal of Petroleum Technology* **48** (04): 296 - 339. DOI: 10.2118/30148-JPT.

Strebelle, S.B. and Journel, A.G. 2001. Reservoir Modeling Using Multiple-Point Statistics. Paper presented at the SPE Annual Technical Conference and Exhibition, New Orleans, Louisiana. Society of Petroleum Engineers SPE-71324-MS. DOI: 10.2118/71324-MS.

Talbert, M., Ma, X., and Datta-Gupta, A. 2008. Upgridding 3-D Reservoir Models in a Channel Environment. Paper presented at the SPE Indian Oil and Gas Technical Conference and Exhibition, Mumbai, India. Society of Petroleum Engineers SPE-113245-MS. DOI: 10.2118/113245-MS.

Tanaka, S., Kam, D., Datta-Gupta, A. et al. 2015. Streamline-Based History Matching of Arrival Times and Bottomhole Pressure Data for Multicomponent Compositional Systems. Paper presented at the SPE Annual Technical Conference and Exhibition, Houston, Texas, USA. Society of Petroleum Engineers SPE-174750-MS. DOI: 10.2118/174750-MS.

Taware, S.V., Sharma, M., Alhuthali, A. et al. 2010. Waterflood Management Using Optimal Rate Control with Accelerated Production Strategy. Paper presented at the SPE Annual Technical Conference and Exhibition, Florence, Italy. Society of Petroleum Engineers SPE-133882-MS. DOI: 10.2118/133882-MS.

Tokhmechi, B., Memarian, H., Noubari, H.A. et al. 2008. Joint Study Based on K-Means Clustering, Asmari Formation, South West Iranian Oil Fields. International Society for Rock Mechanics (ISRM) and Iranian Society for Rock Mechanics (IRSRM) ISRM-ARMS5-2008-159.

Van Doren, J., Douma, S.G., Wassing, L.B.M. et al. 2011. Adjoint-Based Optimization of Polymer Flooding. Paper presented at the SPE Enhanced Oil Recovery Conference, Kuala Lumpur, Malaysia. Society of Petroleum Engineers SPE-144024-MS. DOI: 10.2118/144024-MS.

Vasco, D.W., Datta-Gupta, A., He, Z. et al. 2003. Reconciling Time-Lapse Seismic and Production Data Using Streamline Models: The Bay Marchand Field, Gulf of Mexico. Paper presented at the SPE Annual Technical Conference and Exhibition, Denver, Colorado. Society of Petroleum Engineers SPE-84568-MS. DOI: 10.2118/84568-MS.

Veeken, P.C., Priezzhev, I.I., Shmaryan, L.E. et al. 2009. Nonlinear Multitrace Genetic Inversion Applied on Seismic Data across the Shtokman Field, Offshore Northern Russia. *Geophysics* **74** (6): WCD49-WCD59. DOI: 10.1190/1.3223314.

Watanabe, S., Han, J., Datta-Gupta, A., and King, M.J. 2013. Streamline-Based Time Lapse Seismic Data Integration Incorporating Pressure and Saturation Effects. Paper presented at the SPE Annual Technical Conference and Exhibition, New Orleans, Louisiana. Society of Petroleum Engineers SPE-166395-MS. DOI: 10.2118/166395-MS.

Wu, Z. and Datta-Gupta, A. 2002. Rapid History Matching Using a Generalized Travel-Time Inversion Method. *SPE Journal* **7** (02): 113 - 122. DOI: 10.2118/78359-PA.

Xie, J., Efendiev, Y., and Datta-Gupta, A. 2011. Uncertainty Quantification in History Matching of Channelized Reservoirs Using Markov Chain Level Set Approaches. Paper presented at the SPE Reservoir Simulation Symposium, The Woodlands, Texas, USA. Society of Petroleum Engineers SPE-141811-MS. DOI: 10.2118/141811-MS.

Yin, J., Park, H., Datta-Gupta, A. et al. 2010. A Hierarchical Streamline-Assisted History Matching Approach with Global and Local Parameter Updates. Paper presented at the SPE Western Regional Meeting, Anaheim, California, USA. Society of Petroleum Engineers SPE-132642-MS. DOI: 10.2118/132642-MS.